

THE OPTICAL AND MICROWAVE
PROPERTIES OF MELT PONDS OVER FIRST
YEAR ARCTIC SEA ICE

By

Robert B. Kirk

A thesis submitted in partial fulfillment of the requirements for the degree of

Master of Environment

Department of Environment and Geography

University of Manitoba

Winnipeg, Manitoba

© Robert B. Kirk, June, 2004

**THE UNIVERSITY OF MANITOBA
FACULTY OF GRADUATE STUDIES

COPYRIGHT PERMISSION PAGE**

**The Optical and Microwave Properties of Melt Ponds
Over First Year Arctic Sea Ice**

BY

Robert B. Kirk

**A Thesis/Practicum submitted to the Faculty of Graduate Studies of The University
of Manitoba in partial fulfillment of the requirements of the degree
of**

MASTER OF ENVIRONMENT

ROBERT B. KIRK ©2004

Permission has been granted to the Library of The University of Manitoba to lend or sell copies of this thesis/practicum, to the National Library of Canada to microfilm this thesis and to lend or sell copies of the film, and to University Microfilm Inc. to publish an abstract of this thesis/practicum.

The author reserves other publication rights, and neither this thesis/practicum nor extensive extracts from it may be printed or otherwise reproduced without the author's written permission.

ABSTRACT

The interaction of optical and microwave energy with an actively ablating first year sea ice (FYI) surface is a function of the geophysical properties present over the icescape. In this thesis I evaluate the spatial and temporal variability of the melt pond stage of the FYI lifecycle in terms of its affect on the albedo of optical energy and the backscatter (σ^0) of synthetic aperture radar (SAR). I conduct a field experiment over melting smooth, landfast FYI in the Canadian Arctic Archipelago from YD 167 – YD 191. The purpose of the field experiment is to explore the icescape in terms of the physical and optical characteristics of the surface from point measurements within a defined study region. These point measures are then used to up-scale the physical and optical characteristics to the regional level using aerial photography. The regional statistics derived from 14 flights of aerial photography are then used to compare the temporal relationship between the physical, optical and active microwave characteristics of the seasonally evolving FYI surface.

Results from the field study indicate that the physical and optical characteristics of the surface are represented by 16 discrete surfaces which are summarized by 3 surface categories; ponded, unponded and transitional. The ponded category fluctuated from shallow melt ponds over frazil ice to deep melt ponds with a smooth pond – ice interface. Broadband albedo for melt ponds ranged from 0.34 – 0.19. The transitional surface category forms a ubiquitous ring

surrounding melt ponds having an albedo range between 0.22 and 0.40 while the unponded category was composed of melting snow and a bare ice scattering layer with albedo ranging from 0.54 to 0.76. At the regional level, the temporal evolution of the surface, optical albedo and microwave backscatter is shown to evolve through 4 stages; pond onset, pond development, mature ponds and pond drainage. The relationship between pond fraction and albedo was shown to evolve within each of these stages as pond albedo decreased and unponded albedo increased over time.

The use of SAR was shown to contain information regarding the geophysical and optical state of the surface. However error due to the effect of wind and sensor resolution on point estimates of pond fraction was considerable. Using regionally averaged statistics for the study area and an Incidence Angle Correction Model (IACM) I developed a relationship between the physical state of the surface, optical albedo and microwave backscatter which explained 0.886 of the variance when corrected for the effect SAR viewing geometry.

ACKNOWLEDGMENTS

Sincere appreciation is extended to Dr. David Barber. Dave's support and insight has been of great assistance in this work. Many thanks to the members of the Collaborative – Interdisciplinary Cryospheric Experiment (C-ICE 2001/2002) research teams. In particular, the collaborations and assistance of Randall Scharien, CJ Mundy, Dan Reimer, David Mosscrop, Dr. Tim Papakyriakou, John Iacozza, Kim Morris and Dr. John Yackel are greatly appreciated. Special thanks to Byong Jun Hwang for his aid and patience in the development of the code used in this work as well for his intellectual stimulation. Thanks are also extended to Eric Peake and Julie Kirk for donating their time and energy towards the completion of this work. Finally, I would like to thank Dr. John Hanesiak and Dr. Paul Bullock for their support as committee members.

DEDICATION

This thesis is dedicated to the love and support from my parents Colleen and Eric Peake, and John Kirk as well as my partners in life, Christina and Kayla Maggiora. In many ways, this work is a reflection of your belief in my success. Thank you.

TABLE OF CONTENTS

Abstract	iii
Acknowledgments.....	v
Dedication	vi
Table of Contents	vii
List of Tables.....	xi
List of Figures	xiii
List of Abbreviations	xx
List of Symbols.....	xxi
Chapter 1. Introduction	1
1.1. Motivation.....	1
1.2. Thesis Objectives.....	6
1.3. Thesis Structure	10
Chapter 2. Nature of the Problem.....	12
2.1. Introduction	12
2.2. The Geophysical and Thermodynamic Properties of First Year Sea Ice	14
2.2.1. First Year Sea Ice.....	16
2.2.2. Snow	20
2.2.3. Melt Ponds	27
2.3. The Optical Properties of Melting First Year Sea Ice	31
2.3.1. First Year Sea Ice.....	35
2.3.2. Snow	36
	vii

2.3.3. Melt Ponds	39
2.4. The Microwave Properties of Melting First Year Sea Ice	44
2.4.1. The Role of Dielectrics in Snow and Ice	49
2.4.2. Surface and Volume Scattering Over FYI during Spring Ablation	51
2.4.3. The Effect of Incident Angle on SAR Backscatter	53
2.4.4. The Effect of Wind on SAR Backscatter	55
2.4.5. The Use of SAR for Determination of the Geophysical Properties of Landfast Smooth FYI.	57
2.4.5.1. First Year Sea Ice	59
2.4.5.2. Snow	61
2.4.5.3. Melt Ponds	63
2.5. Conclusions.....	65
Chapter 3. In situ Physical and Radiative Properties of Melt Ponds	68
3.1. Introduction	68
3.2. Data and Methods.....	69
3.2.1. Physical Sampling	73
3.2.2. Albedo Sampling	76
3.3. Results and Discussion.....	82
3.3. Results and Discussion.....	82
3.3.1. Observed Physical and Optical Evolution of an Ablating FYI Surface	82
3.3.1.1. The Unponded Surface Category	88
3.3.1.2. The Transitional Surface Category	92
3.3.1.3. The Poneded Surface Category.....	95

3.4. Conclusions.....	103
Chapter 4. The Spatial Distribution of the Physical and Radiative Properties of Melt Ponds.....	105
4.1. Introduction	105
4.2. Data and Methods.....	107
4.2.1. Aerial Photography.....	107
4.2.2. Extrapolation of Point Measurements to Regional Scales using Aerial Photography	112
4.3. Results and Discussion.....	117
4.3.1. Regional Physical and Albedo Characteristics from Digital Aerial Photography	117
4.3.1.1. The Effect of Surface Morphology on Derived Albedo	118
4.3.2. The Relationship between Albedo and Pond Fraction.....	125
4.3.3. Time Series Evolution of Aerially Derived Albedo	128
4.3.3.1. Pond Onset.....	130
4.3.3.2. Pond Development	132
4.3.3.3. Mature Ponds.....	134
4.3.3.4. Pond Drainage	137
4.3.3.5. The Effect of Snow on Surface Albedo	140
4.4. Conclusions.....	143
Chapter 5. Extracting Melt Pond Characteristics from Microwave Backscatter	145
5.1. Introduction	145
5.2. Data and Methods.....	147
5.2.1. RADARSAT-1 Calibration and Geocoding	148
5.2.2. Development of the Sigma Naught Temporal Trend	149

5.2.3. Associating SAR Backscatter to Point Surface Properties	153
5.3. Results and Discussion.....	154
5.3.1. The Temporal Evolution of Sigma Naught.....	154
5.3.1.1. Winter	158
5.3.1.2. Transition	159
5.3.1.3. Melt Onset	161
5.3.1.4. Melt Ponds.....	162
5.3.2. The Effect of Wind on SAR Signatures over Melt Ponds.....	162
5.3.3. The Relationship between Microwave Backscatter and FYI Pond Fraction during the Melt Pond Season.....	166
5.3.3.1. A Comparison of SAR Backscatter to Point Estimate Surface Characteristics	167
5.3.3.2. A Comparison of Bulk SAR Backscatter to Bulk Surface Characteristics	172
5.4. Conclusions.....	179
Chapter 6. Conclusions and Recommendations.....	182
6.1. Conclusions.....	182
6.2. Summary.....	188
6.3. Recommendations.....	190
References	192
Appendix A. Year Day Conversion.....	201
Appendix B. Melt Pond Study Schedule.....	202
Appendix C. Programs used with Aerial Photography	204
Appendix D. RADARSAT-1 Data Set.....	218
Appendix E. Programs used with SAR Data	220

LIST OF TABLES

Table 3.1. Melt Pond Study Area coordinates for C-ICE 2002. All measures are recorded in decimal degrees.	71
Table 3.2. Description of physical measurements collected during the Melt Pond Study.....	74
Table 3.3. Limits of integration (a & b) for spectral albedo over designated wavelengths.	80
Table 3.4. Representative melt surfaces documented during the 2002 Melt Pond Study. Each surface type is associated with a time interval corresponding to the evolving physical and optical surface.....	87
Table 3.5. Three representative surface categories (unponded, transitional and ponded surfaces) with corresponding surface types for an ablating FYI volume. Each surface type is associated with a depth and various integrated albedo segments averaged from samples collected throughout the field season. Standard deviation is given for broadband albedo measures (Std. Dev.).....	88
Table 3.6. Evolution of pond bubble fraction and albedo during the early stages of pond formation. Bubble fraction estimates were made from the separation of bubbles from the photograph background using image histograms.	98
Table 4.1. Paraglider flight information for C-ICE 2002.....	110
Figure 4.8. Changes in derived surface albedo along flight paths captured between YD 177 and 189. The albedo for each flight line is segmented into spectrally integrated intervals for blue (BLU), photosynthetically active radiation (PAR), integrated broadband (INT) and near infrared (NIR). Image ID represents the number of photographs captured having time and position attributes.	121
Table 4.2. The distribution of surface types for individual flights derived from aerial photography through the melt season. Table a) shows seven flights from YD 170 through YD 177 while table b) completes the time series to YD 191. (seal hole – SH; deep	

melt pond – DP, w/ low bubble density – DP_LB; moderate depth melt pond – MP, w/ moderate bubble density – MP_MB; shallow melt pond – SP, w/ high bubble density – SP_HB; transitional surface – TR; transitional blue surface – TR_B; bare blue ice – BI; new deteriorated ice – NI; new snow – NS; old (mature) deteriorated ice – OI; shallow saturated snow – SS; deep saturated snow – DS; slush – SL).....	123
Table 4.3. Individual flight slope of regression lines (β) for pond fraction versus broadband albedo. Flights having a statistically similar β suggest four stages of melt pond ablation. Comments outline major contributors to albedo: snowpack (S), pond bubbles (B), mature ponds (P), bare ice (I), maximum pond extent (M), surface drainage (D) and new snow (NS).	127
Table 5.1. The RADARSAT-1 dataset used for calculation of winter incidence models.	152
Table 5.2. List of RADARSAT-1 data used for the direct comparison of derived surface characteristics through the melt season. The explained variance (R^2) between pond fraction and σ^0 is provided.....	167
Table A.1. Year day conversion table.....	201
Table B.1. List of location and times for the Melt Pond Study Site.	202
Table D.1. RADARSAT-1 data set collected and processed at the Alaska SAR Facility. Images are stored in the 8-bit CEOS format.....	218

LIST OF FIGURES

Figure 1.1. Diagram of the scientific objectives. Objective 1 examines the geophysical processes which drives optical and microwave scattering. Objective 2 examines the relationship between microwave and optical scattering and the physical surface.	8
Figure 2.1. The evolution of first year sea ice, from initial ice formation through summer ablation. External forcing for each stage is in brackets. (adapted from Grenfell et al., 1992).	15
Figure 2.2. The structure and timing of thick first year sea ice. (Adapted from Eicken, 2003).	17
Figure 2.3. The vertical concentration of salinity for first year sea ice as it evolves from initial growth to drainage. (Adapted from Malmgren, 1927).	18
Figure 2.4. Categorical structures of the general thermodynamic regimes representing the seasonal transition from Freeze-up to Advanced Melt for snow-covered, landfast, FYI in the Canadian Arctic. The shortwave flux is recorded in Wm^{-2} . Temperature profiles are summarized from 10 years of in situ data. The available shortwave energy is denoted in summary above the thermodynamic profiles. Adapted from Barber et al. (1999).	23
Figure 2.5. Schematic depiction of sea-ice radiative transfer processes across the OSA interface where F is equal to total solar radiation (adapted from Perovich, 1996).	34
Figure 2.6. The viewing geometry of synthetic aperture radar (SAR). The look angle for RADARSAT-1 ranges from 20° to 49° from nadir. Adapted from Henderson and Lewis (1999).	46
Figure 2.7. Sea ice dielectric parameters and interfaces (adapted from Carlström, 1995).	48
Figure 2.8. Differences in backscatter versus incidence angle for surface (σ°_s) and volume scatters (σ°_v). The proportion of ice and melt ponds within a given pixel will dictate whether the	

backscatter is dominated by surface or volume scattering (adapted from Barber, 1993).	54
Figure 2.9 Evolution of first-year sea ice from winter to advanced melt as seen by time series SAR backscatter. Adapted from Barber et al., 2001.	58
Figure 3.1. The location of the Melt Pond Study Area. The site was located west of Truro Island, Nunavut, Canada on smooth landfast first year sea ice.	72
Figure 3.2. The 3km ² Melt Pond Study Area was broken into 100m ² sampling sites. Two access roads running N-S and E-W intersect through the centre.	73
Figure 3.3. An aerial view of the sampling site for YD 175. Snow machines (in the upper portion of the photograph) are 50m from researchers (left of centre on the photograph). Notice that the remaining snow patches are aligned in a linear fashion orthogonal to the predominant wind direction.	76
Figure 3.4. A broadband integrated albedo measurement taken over ablating FYI. Notice the high degree of surface flooding and evidence of drainage along the pond edge. (photo by D. Barber)	77
Figure 3.5. Snow depth and integrated broadband albedo (305nm – 2800nm) of FYI surface prior to the start of the Melt Pond Study. Data observations were recorded at the C-ICE Meteorological Station.	83
Figure 3.6. Density, salinity and temperature of the snowpack prior to the start of the Melt Pond Study. Values represent the average from observations made using a 2cm interval through the snowpack. Observations were recorded in close proximity to the meteorological station.	83
Figure 3.7. Pond fraction estimates observed for individual sampling sites over the course of the melt season. Year day fractions correspond to the time of day pond estimates were taken (.25 = morning, .5 = afternoon, .75 = night).	85
Figure 3.8. Time series aerial photographs taken by the powered paraglider. The images show the change in surface	

characteristics over the melt season. Note the seal hole (upper left) which provided the area with drainage and resulted in lower levels of ponding once drainage began. The dark rectangle is one of three tarpaulins (4m x 5m) deployed within the study area. 86

Figure 3.9. Averaged integrated albedo for snow and bare ice types observed through the melt season. New Snow (NS), Deep Saturated snow (DS), Saturated Snow (SS), New deteriorated Ice (NI) and Old deteriorated Ice (OI)..... 89

Figure 3.10. Averaged integrated albedo for the transitional surface category. Blue Ice (BI), Transitional pond/snow interface (TR) and Slush (SL). 93

Figure 3.11. Averaged spectral albedo for melt ponds at different stages and depth. Deep Pond (DP), Moderate Pond (MP), Shallow Pond (SP), Deep Pond Low Bubble Density (DP_LB), Moderate Pond Moderate Bubble Density (MP_MB) and Shallow Pond High Bubble Density (SP_HB)..... 96

Figure 3.12. The evolution of melt ponds through the melt season. Bubble densities quickly reduced after initial ponding however a ring of high bubble density is found along pond fringes during times of advance. Picture ID correspond to table 3.6. Each image is roughly 30cm x 23cm. 98

Figure 3.13. Processes leading to melt pond maturity over FYI. The melt pond – albedo feedback is initiated by an increase in the atmospheric heat flux (L), stimulating snow ablation and the development of melt ponds. During initial pond formation the albedo of young ponds is dictated by pond depth and the scattering properties of the frazil ice layer. Ablation of the frazil layer is a function of the wind induced mechanical weathering, and solar insolation (Wm^{-2}). As the melt ponds matured, the albedo is dictated by pond depth and the optical properties of the columnar ice volume. 100

Figure 3.14. Liquid precipitation captured using a rain gauge and recorded during the melt pond field season. Shaded areas represent liquid precipitation and white areas represent solid precipitation. Precipitation for YD189 was a combination of both rain and snow. Most snow occurred in the latter portion of the melt season leading to an increase in overall surface

	albedo due to the formation of slush in melt ponds and increased optical scattering on ablating ice surfaces.	102
Figure 4.1.	Locations of the Melt Pond Study Area, Meteorological Site, Truro Island Base Camp and three oranges tarpaulins.	108
Figure 4.2.	Motorized paraglider used during C-ICE 2002. Pilots: Dr. D. Barber (left) and Mr. D. Reimer (right).....	108
Figure 4.3.	Paraglider image captured YD 186. Drainage caused by a seal hole in the upper left corner is evident in the photo along with the 5m x 4m tarpaulin deployed in the Melt Pond Study Area.	111
Figure 4.4.	The use of isodata clustering on digital photographs of various surfaces observed over the course of the melt season. Images b) and c) show the linear arrangement of melt ponds following snow distribution patterns while both c) and d) illustrate the influence of drainage on pond fraction and corresponding albedo.	114
Figure 4.5.	Cartographic model for the application of optical and physical surface attributes to aerial images based on representative clusters. Base programs used to apply field statistics to individual aerial photographs can be found in Appendix C.	116
Figure 4.6.	Comparison of the temporal evolution of both field observed (Obs_PD) and aerially interpolated (Int_PD) pond fraction. Box plot quartiles are plotted for each aerial photography flights.....	118
Figure 4.7.	Changes in derived surface albedo following flight paths captured between YD 170 and YD 175. The albedo for each flight line is segmented into spectrally integrated intervals for blue (BLU), photosynthetically active radiation (PAR), integrated broadband (INT) and near infrared (NIR). Image ID represents the number of photographs captured having time and position attributes.	120
Figure 4.9.	The relationship between aerially derived pond fraction and broadband albedo through the melt season. Albedo and pond fraction estimates are based on the weight sum of surface type field statistics applied to each aerial photograph.....	126

Figure 4.10. Comparison of the temporal evolution of broadband (BRD) study area albedo (SC), pond (PD) and snow/bare ice (SN) albedo estimates for the study area and meteorological station. The graph also illustrates the four stages of melt pond development: a) pond onset, b) pond development, c) mature ponds and d) pond drainage.	129
Figure 4.11. This graph illustrates the evolution of integrated spectral albedo over the 2002 season. The four stages of melt pond development; a) pond onset, b) pond development, c) mature ponds and d) pond drainage are also shown.....	130
Figure 4.12. Images captured during “pond onset” (YD 168 – YD 171) over first year sea ice. Corresponding derived albedo and surface fraction highlight the physical and optical characteristics typical of this period of surface melt.	132
Figure 4.13. During the “pond development” stage (YD 172 – YD 177) of spring melt the effect of surface drainage is limited to a localized area in close proximity to drainage point while the bulk of the surface remains highly flooded.	134
Figure 4.14. The “mature pond” stage of surface ablation (YD 178 – YD 184). As the surface stabilizes after maximum pond extent resulting from drainage channel expansion, previously ponded areas deteriorate into the surface scattering layer.	136
Figure 4.15. The “pond drainage” stage of spring ablation (YD 185 – YD 190). Elaborate surface channels, pond drainage and finally “dry ice” are typical of the pond drainage stage of the melt season.	139
Figure 4.16. The effect of snowfall (snow) on broadband (BRD) albedo during the 2002 melt season. The difference in albedo (Δ BRD) and pond fraction (PD_FR) are also plotted and show the relationship between increased albedo due to the availability of unponded surfaces. The four stages of melt pond development; a) pond onset, b) pond development, c) mature ponds and d) pond drainage are also shown.....	141
Figure 5.1. RADARSAT-1 image outlining the two spatial areas used in the development of the SAR dataset. The inner square (40) represents the dataset used for calculating the bulk SAR backscatter statistics while the outer square (200) was	

imported into a GIS format for comparison to aerial flight point data.	149
Figure 5.2. RADARSAT-1 standard beam geometry. Radiometric calibration for each beam must be standardized from σ° to δ° before comparison of backscatter can be made. (Adapted from the Canadian Centre for Remote Sensing website, 2004).....	150
Figure 5.3. RADARSAT-1 standard beam 3 image captured on YD 93. Notice the consistent texture of the FYI surface suggesting a smooth, homogeneous volume. This image has undergone radiometric calibration and was standardized for incidence angle effects with the Melt Pond (MP) Study Area outlined in white.....	155
Figure 5.4. The RADARSAT-1 backscatter coefficient (σ°) as a function of standard beam incidence angle observed during the winter season. a) Second order polynomial model of backscatter (δ) values averaged over 9 sites within the study region. b) Shift coefficient (ω) for standardizing RADARSAT-1 standard beam backscatter to the near range. The shift interval ranges from 1 – 6 corresponding to the standard beam interval n, n+1 where n > 1 (ie. beams 2, 3).....	157
Figure 5.5. Temporal trend of σ° for the 2002 Melt Pond Study. Dashed boxes envelop observed backscatter for winter, transitional, melt onset and melt pond surface states as described in the text.	158
Figure 5.6. The effect of wind on SAR backscatter. Pond fraction (PF), wind speed (W), wind direction in degrees (D) and weather are all indicated for each image. The images have been corrected for viewing geometry and areas of low backscatter appear dark. All images are courtesy of the Canadian Space Agency (© CSA, 2002).....	165
Figure 5.7. Comparison of bulk sigma naught values to pond fraction during the melt pond season. Data points 1, 2, and 3 represent values obtained under moderate wind speeds ($1.6\text{ms}^{-1} - 2.1\text{ms}^{-1}$).....	174

Figure 5.8. A comparison of sigma naught to albedo bulk characteristics during the melt pond season. Increases in backscatter exhibit a positive relationship to surface albedo. Data points 1, 2, and 3 represent values obtained under moderate wind speeds ($1.6\text{ms}^{-1} - 2.1\text{ms}^{-1}$)..... 175

Figure 5.9. The relationship between averaged albedo and pond fraction, derived from surface observation and aerial photography during the melt pond season. 176

Figure 5.10. A comparison of average backscatter (σ^0), albedo and pond fraction found within the Melt Pond Study Area. Notice the inverse relationship between pond fraction and σ^0 . The graph has been partitioned into pond onset (a), pond development (b), mature pond (c), pond drainage (d) stages of the melt pond season and drained ice (e). 177

LIST OF ABBREVIATIONS

ASF	Alaska SAR Facility.
C-ICE	Collaborative Interdisciplinary Cryospheric Experiment.
CSA	Canadian Space Agency.
DN	Digital number.
EM	Electromagnetic energy.
FOV	Field of View.
FYI	First Year sea Ice.
GCM	General Circulation Model.
GPS	Global Positioning System.
MYI	Multiyear Sea Ice.
Nadir	The point on the earth orthogonal to the sensor.
NIR	Near-infrared portion of the electromagnetic spectrum.
OSA	The ocean – sea ice – atmosphere interface.
RADAR	RAdio Detection And Ranging.
SAR	Synthetic Aperture Radar.
SEB	Surface Energy Balance.
TOA	Top Of Atmosphere.
YD	Year Day.

LIST OF SYMBOLS

α	Albedo.
σ°	Microwave backscattering coefficient.
δ°	Microwave backscattering coefficient standardized by incidence angle.
λ	Wavelength.
θ	Incidence angle as measured from NADIR.
ϵ^*	Complex dielectric constant.
ϵ'	Dielectric permittivity.
ϵ''	Dielectric loss.
C	Degrees Celsius.
K	Degrees Kelvin.
kg	Kilogram.
m	Metre.
ppt	Parts per thousand.
s	Second.
W	Watts.

CHAPTER 1. INTRODUCTION

1.1. Motivation

Over the last several years concern regarding the state of the global climate has increasingly focused on polar regions and in particular on the role of the marine cryosphere. In terms of climate research, the marine cryosphere is one of three discrete volumes; the polar oceans (hydrosphere), the overlying sea ice (cryosphere) and the air (atmosphere). The marine cryosphere consists of various ice types overlying the hydrosphere such as shore fast ice, snow and the various stages of sea ice. Despite the obvious physical differences of each of these mediums, they create a highly coupled system known as the ocean – sea ice – atmosphere (OSA) interface. Of particular interest to the work presented here is how changes in the extent and thickness of sea ice, brought on by a changing climate, would affect mass and energy fluxes across this medium and how these variables drive biological production, seasonal fresh water inputs to the oceanic thermohaline circulation, and its overall effect on regional, hemispheric and ultimately global, climates.

The marine cryosphere undergoes a seasonal cycle of advance and retreat regulated in part by the quantity of solar insolation available to polar regions as well as the influence of regional temperature and atmospheric circulation. The cycle of ice growth and decay is well defined and the reader is directed to the works of

Barber et al. (1999) for a complete definition. For the purpose of this work three key types of ice will be defined. First year sea ice (FYI) forms as ocean temperatures drop below the freezing point during autumn (approximately -1.8°C). This type of ice is characterized by high salinity (liquid salts, known as brine) which are trapped within the crystal lattice of the ice during freezing. FYI ranges in thickness between 30cm – 200cm.

After the summer melt season, surviving pieces of FYI enter autumn freeze-up and become second year sea ice (SYI). SYI is considerably stronger than FYI due to the flushing of brine from the ice structure during spring melt. Ice that survives at least two melt cycles is termed multiyear ice (MYI). MYI is characterized as having almost no brine within the upper layer of the ice structure, a thickness averaging three to five metres, and a hummocky surface created by numerous pond/drainage cycles. Due to the low salinity and generally larger volume, this type of ice is considerably stronger and more resistant to melt than FYI.

Recent reports suggest that the amount of MYI in the Canadian Arctic is diminishing due to an increase in regional temperatures (Folland et al. 2001; Parkinson et al. 1999; and Rothrock et al. 1999). Projections for Arctic climate change suggest that the aerial extent of sea ice will continue to decrease towards a point where the Arctic will be seasonally ice free. The Canadian GCM suggests this point will be reached as early as 2050 (Flato and Boer, 2001). The recent

trend observed in the rate of reduction to the aerial extent of sea ice agree, at least to a first order, between modeled projections and observations from passive microwave satellite data between the periods 1978 and 2000 (Folland et al. 2001). This trend, if it continues, will mean first year sea ice (FYI) will become more ubiquitous in the Arctic and thus more important as an element within the OSA interface.

Current estimates from satellite data show the minimum area covered by sea ice is about $8 \times 10^6 \text{ km}^2$ (1.5% of the Earth's surface), while the maximum extent of sea ice in winter months is about $15 \times 10^6 \text{ km}^2$ (3% of the Earth's surface) (LeDrew et al., 1992). The extent of Arctic sea ice, as observed by satellite, decreased at a rate of about 3% per decade since the 1970's (Parkinson et al., 1999). Also of great concern are estimates based on submarine measurements indicating that summertime Arctic ice thickness has diminished by 40% over the past 30 years (Rothrock et al., 1999), an estimate supported by measurements made by the Canadian Ice Service (Falkingham, 2000).

A key forcing factor in the rate of FYI formation and decay is the temporal evolution of the sea ice – albedo feedback. Albedo is the proportion of the total incident solar radiation reflected from a surface relative to that which is incident. As a fundamental variable used in regional and global climate models, albedo is coupled to the amount of energy available to a surface. In terms of this work, albedo strongly affects the overall energy balance of the marine cryosphere. This

is especially true during spring melt when surface albedo undergoes considerable change at local and regional scales. Over the course of a single melt season, the regional energy balance over smooth first year sea ice is composed, to varying degrees and extent, of melting snow, ablating ice, melt ponds and open water (Papakyriakou, 1999). This creates a complex web of albedo variation ranging from 0.90 for newly fallen snow to 0.07 for open water with considerable change at sub-metre resolutions (DeAbreu et al. 1994; Hanesiak et al. 2001a; Perovich, 1996).

During spring melt, the marine cryosphere undergoes dramatic changes in its radiative budget as snow gives way to melt ponds and open water. An important measure for monitoring the evolution of FYI's radiative budget is the snow/sea ice – albedo feedback. This feedback is initiated by a positive temperature perturbation as winter subsides to spring. The increase in ambient air temperature initiates snowmelt resulting in a decrease in surface albedo. The decrease in snow albedo increases solar loading providing higher temperatures within the snow volume which in turn increases snowmelt and further reduces albedo. As melt water begins to pool on the surface of the ice, ponds form revealing the darker ice surface below, further decreasing albedo. With lower albedo, more solar insolation is available to the system accelerating melt, and the expansion and deepening of melt ponds. A more detailed representation of this feedback process will be explored in chapter 2.

The remoteness of polar regions results in sparse measurements of the surface at both the local and regional level. Satellites have gained acceptance as a tool for monitoring these areas due to their consistent temporal coverage and high spatial resolution (Barber et al. 2001). Traditional sensors for monitoring the Earth's radiation budget include optical spectrometers which measure the peak portion of the electromagnetic (EM) spectrum emitted by the sun. Unfortunately these sensors are only useful for monitoring areas under solar illumination and clear skies. These requirements limit the usefulness of optical sensors for polar monitoring due to the long periods of darkness during winter and ubiquitous cloud cover in the non-winter period. Thus scientists interested in monitoring the polar regions have increasingly relied on satellite based microwave scatterometers and radiometers. Microwave sensors have the unique ability to monitor the Earth's surface during times of darkness and cloudiness, and are sensitive to the presence of both solid and liquid water within the OSA interface.

Although the use of active microwave sensors such as RADARSAT-1 have proven effective for monitoring the annual sea ice cycle (Livingston, et al. 1987, Drinkwater and Crocker 1988, Barber 1993, Kwok et al. 1998), a strong relationship between the microwave and optical portions of the electromagnetic spectrum has yet to be established. Instead, an increase in microwave backscatter (σ^0) due to the presence of water within the snowpack has been an indicator for the start of the sea ice – albedo feedback and linear models have been used to predict the evolution of albedo during the melt season (Sedlacek, 2001).

1.2. Thesis Objectives

The OSA interface operates as a complex and highly coupled system whereby the physical and thermodynamic properties of the system are affected by atmospheric and hydrospheric forcing throughout a complete range of spatial and temporal scales. The evolution of spring melt over smooth FYI is of interest to climatology due to its feedback with regional climate and its control on ecosystem processes operating across the OSA interface. Few studies have examined the spring period evolution of first year sea ice in any detail and even fewer have examined the spatial and temporal variability over FYI which is 'fast' (attached to shore) during spring ablation. In my thesis I intend to examine the evolution of spring melt over landfast FYI structured according to the following scientific objective:

Science Objective 1: "To understand the geophysical processes which drive optical and microwave scattering during the melt season."

In order to ensure a tractable progression of this work, further constraints to the geophysical, radiative and temporal extent of the study are defined. The geophysical constraints are confined to snow covered, smooth landfast FYI representative of seasonal ice found in the Canadian Arctic Archipelago. The study is limited to integrated spectral albedo (338nm – 950nm), broadband albedo (300nm – 3000nm) and the microwave (5.6cm) portions of the electromagnetic spectrum. Finally, the study commenced at the start of early snowmelt, and

continued through pond development and drainage of the ice surface. The nomenclature of melt onset, early melt, advanced melt and drainage is used here following Livingston et al. (1987) and will be discussed in Chapter 2.

Within the constraints of the study, a detailed examination of the physical and electromagnetic evolution of snow covered FYI as it progresses through the melt season is presented. Optical and microwave portions of the electromagnetic spectrum all interact independently with the sea ice surface based on the physical, thermodynamic and dielectric nature of the evolving system. The physical basis for the scattering characteristics at different wavelengths leads to the second scientific objective, namely to:

Scientific Objective 2: "Construct a link between microwave and optical scattering based on the physical characteristics of the melt surface."

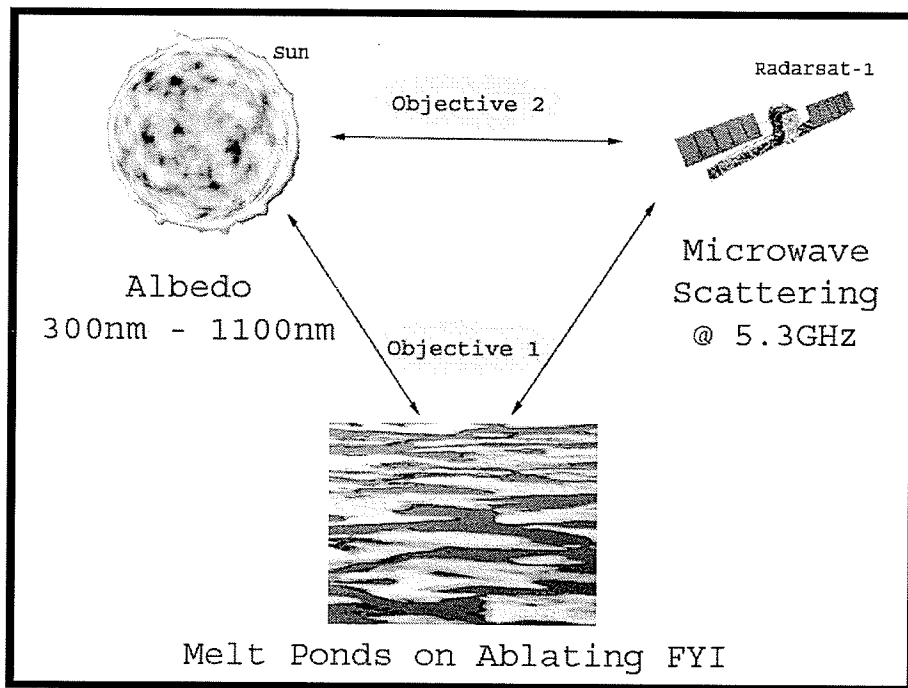


Figure 1.1. Diagram of the scientific objectives. Objective 1 examines the geophysical processes which drives optical and microwave scattering. Objective 2 examines the relationship between microwave and optical scattering and the physical surface.

A successful link will allow for the extraction of both optical albedo and physical properties of the ice surface during spring melt from time series active microwave data. This in turn will allow for a greater understanding of the energy balance over the ice surface for use in regional and global climate models (GCM). The relationships under investigation within the context of this work are shown in figure 1.1. Tools used to assess the scientific objectives are divided into three sections:

- 1) *In situ Observations*: The primary field experiment examines the physical and optical evolution of melt ponds on first year sea ice. This work provides

detailed descriptions of the transition from an ice surface covered by snow to one dominated by melt ponds and bare ice. The field study dataset includes a suite of physical and optical measures conducted within a dedicated melt pond study site. The physical data will be used as a foundation from which to relate the optical albedo of the surface to its corresponding microwave response.

- 2) *Aerial Observations:* Coupled with in situ observations are aerial observations recorded by a low altitude/high resolution digital camera. The camera was mounted on a powered paraglider piloted over the study area during the melt season. The use of the paraglider allowed in situ measurements from the surface to be scaled to the regional level needed for comparison of microwave backscatter.
- 3) *Microwave Data:* An active microwave temporal dataset was collected over the study area beginning in late winter and continuing through spring ablation. Microwave frequencies are sensitive to physical changes on the ice surface, mainly the presence of water and brine, and these relationships will be explored with special attention paid to changes in backscatter due to the evolving icescape.

1.3. Thesis Structure

This thesis is organized into six chapters. In the first chapter I introduce the reader to the marine cryosphere and outline the rationale and goals for my study. Chapter 2 provides an overview of the processes and theories following the metamorphosis of the FYI volume as it progresses from late winter through the melt season. In this chapter, I focus on the linkages between the thermodynamic, geophysical and electromagnetic characteristics of the FYI surface/volume during spring ablation as addressed through current literature.

Chapter 3 outlines the in situ measurements I obtained during the 2002 melt pond sampling program. Collection of morphological and albedo variables were recorded as the surface evolved from dry snow to one dominated by melt ponds. Dominant surfaces, both physically and radiatively, were catalogued on a daily basis and changes to these surfaces monitored throughout the field season. This led to a series of categories used to describe the physical and optical surface. These categories are defined as unponded, transitional and ponded and contain 16 individual surface types observed through the melt pond season.

In Chapter 4, I apply the unponded, transitional and ponded surfaces to aerial photography. The use of aerial photography is used to 'scale-up' the physical and radiative properties of the evolving icescape to the regional level and I develop the temporal trend with four discrete stages of the FYI melt pond season; pond onset, pond development, mature pond and pond drainage. Each melt pond stage is

used to quantify changes in the physical and albedo characteristics observed during the melt pond season.

Chapter five explores the relationship of the regional physical and surface albedo variables developed from the aerial surveys to the microwave backscatter data. Microwave backscatter has been used to estimate the evolution of melt ponds over FYI but limited information has been extracted on the physical variables present during this time period. This is mainly due to limited data available at a spatial resolution comparable to active microwave sensors. With the high temporal coverage captured by the powered paraglider at the regional level, I explore a process for extracting physical and optical properties from microwave backscatter.

In the final chapter, Chapter 6, I offer specific comments on the links between the results of individual chapters to the scientific objectives for this thesis. This is followed by a summary of the relevant work to the scientific community and recommendations for future research.

CHAPTER 2. NATURE OF THE PROBLEM

2.1. Introduction

Within the context of the marine cryosphere smooth, landfast first year sea ice undergoes a number of phases throughout the annual cycle. From the onset of ice formation in the fall, environmental variables such as the salinity of seawater, ambient temperature and snowfall, all combine to influence the composition and extent of FYI. The benefit of working on fast ice in the Arctic Archipelago is that seasonal ice forms between islands during consolidation events creating smooth, relatively homogeneous sheets of thick FYI. These sheets are anchored to the land allowing for easy access and a stationary volume from which to study.

The most influential environmental variable regulating sea ice growth is the timing and thickness of snow accumulation on the ice surface. The low thermal-conductivity of snow acts as an insulator that buffers the cold atmosphere from the ice volume and thus limits the atmospheric heat flux across the ocean – sea ice – atmosphere (OSA) interface, thereby regulating ice thickness. The amount of solar radiation available to the surface during non-winter periods is also strongly tied to the presence and state of snow. Cold snow has a high albedo, near 0.85, whereas melting snow has an average albedo of 0.6 (Curry et al., 2001; Hanesiak et al., 2001b; Barry, 1996; Perovich, 1996; Warren, 1982). Consequently, during the early stages of the melt season the warming of ice due to solar insolation is

intimately tied to the presence of snow (Hanesiak et al., 1999; Curry et al., 1995; Grenfell, 1991; Jordan, 1991; Shine and Henderson-Sellers, 1985; Wiscombe and Warren, 1980). The high albedo and low conductivity of snow further combine to insulate the ice surface from the warming atmosphere in spring. This allows for the presence of ice much longer into summer than would otherwise occur if no snow were present. However, as spring emerges, snowmelt causes ponding on the ice surface, triggering a host of physical and radiative changes across the OSA interface. The physical evolution of melt ponds on the optical and microwave energy interaction over smooth FYI is the primary focus of this work.

In this chapter I describe the evolution of snow covered first year sea ice as it progresses through the melt season. I begin with an overview of the physical and thermodynamic properties of FYI. An examination of the optical and microwave properties associated with an evolving ice sheet is then reviewed in the context of previous studies. This examination leads to a scientific investigation which was conducted over smooth, landfast FYI in the Canadian Arctic Archipelago during spring melt.

2.2. The Geophysical and Thermodynamic Properties of First Year Sea Ice

First year sea ice forms annually when temperatures within the mixed layer of the ocean drop below the freezing point. Seawater has an average salinity of 32 parts per thousand (ppt), which depresses the freezing point to -1.8°C . Once the temperature within the mixed layer drops below -1.8°C , mainly due to wind induced convective mixing, new ice platelets called frazil begin to form. This stage of ice development is termed fall freeze-up. A detailed description of fall freeze-up and its effect on optical and microwave energy interaction can be found elsewhere (e.g. Eicken, 2003; Barber, 1993; Grenfell, et al., 1998; LeDrew et al., 1992; Tucker et al., 1992; Weeks and Ackley 1986) and thus only a brief introduction to FYI formation will be provided.

Depending on the degree of atmospheric induced cooling, frazil ice grows into shuga, nilas and pancake ice (figure 2.1). Both nilas and pancake ice continue to consolidate into a single solid volume measured at the regional level, known as first year sea ice (FYI). Winds, currents, air and water temperatures, as well as timing and magnitude of snow accumulation contribute to the eventual roughness, texture, chemical composition, and temperature gradient through the sea ice (Jezek *et al.*, 1998). For a complete definition of terminology used for ice classification the reader is directed to the **Manual of Standard Procedures for Observing and Reporting Ice Conditions (MANICE)** available from the Canadian Ice Service.

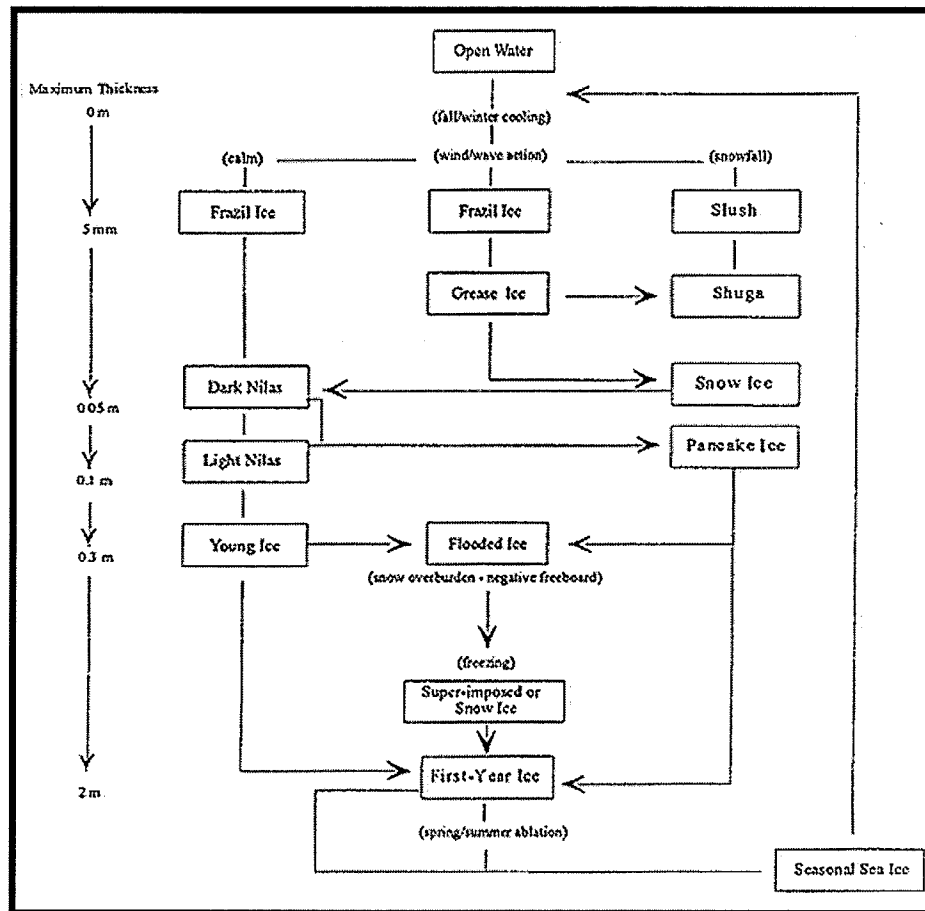


Figure 2.1. The evolution of first year sea ice, from initial ice formation through summer ablation. External forcing for each stage is in brackets. (adapted from Grenfell et al., 1992).

The following sections outline three physically and thermodynamically different media composing the FYI volume during spring melt. Ice, snow and melt ponds all contribute to the physical, optical and microwave characteristics of the OSA interface. Each of these variables also regulates the thermal and radiative heat fluxes through the OSA thus controlling the rate of melt and ultimately determining the timing of complete ice decay.

2.2.1. First Year Sea Ice

Although environmental conditions combine to create varying thickness of FYI, its overall structure is well understood. By late winter (approximately early May at latitudes greater than 70°N latitude), Arctic first year sea ice will have reached its greatest thickness averaging between 1.5m and 2.0m. Within the vertical structure of FYI, two distinctive types of ice are found. Beneath the snow layer, a thin layer of frazil generally 10cm to 30cm thick overlies a vertically oriented columnar ice structure. Frazil ice is a remnant of initial ice growth and consists of needle, spicule platelet and ice crystal aggregates (Vant et al., 1986; Weeks and Ackley, 1986). Below the frazil ice lays a thick layer of columnar ice formed at the ice – ocean interface. This process of ice growth, called congelation, forms vertically elongated prismatic crystals that can grow to several centimetres in diameter and tens of centimetres in length (Eicken, 2003). Interspersed amongst these columns, small pockets of brine and air (>1mm in diameter) are randomly distributed (figure 2.2). The concentration of each of these constituents is directly dependent on the rate of fall freeze-up with higher concentrations of air and brine occurring during times of rapid ice growth (Barber, 1993).

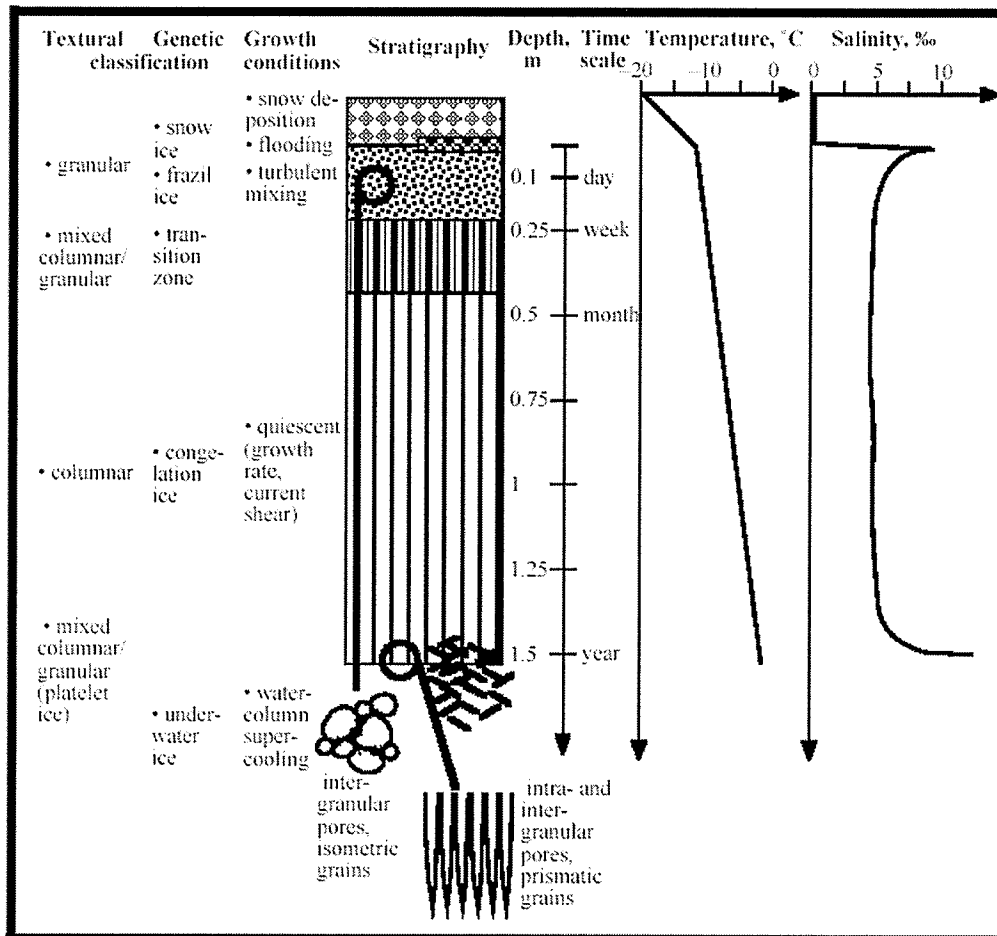


Figure 2.2. The structure and timing of thick first year sea ice. (Adapted from Eicken, 2003)

By late winter, the effects of prolonged cold and gravity both have an effect on ice structure. Brine loss within the ice volume occurs mostly due to gravity drainage. Beginning immediately after formation, brine is drawn down through the ice volume to warmer, less dense ice following a negative temperature gradient from the ice surface towards the ocean – ice interface. This creates a heterogeneous lattice of brine drainage channels running vertically through the ice volume (Eicken, 2003; Vant et al. 1986).

Winter brings long periods of cold temperatures which cause a reduction in the temperature of the upper portion of the ice volume. Cold temperatures cause ice platelets to squeeze together, pushing out air and salt from the interstices of the ice platelets, a process called brine expulsion (Weeks and Ackley, 1986). Brine that has been expelled to the surface becomes a concentrated saline solution at the snow – ice interface (Barber 1993; Livingston et al. 1987). The processes of brine expulsion and gravity drainage results in a “C” shaped salinity profile through the ice (figure 2.3).

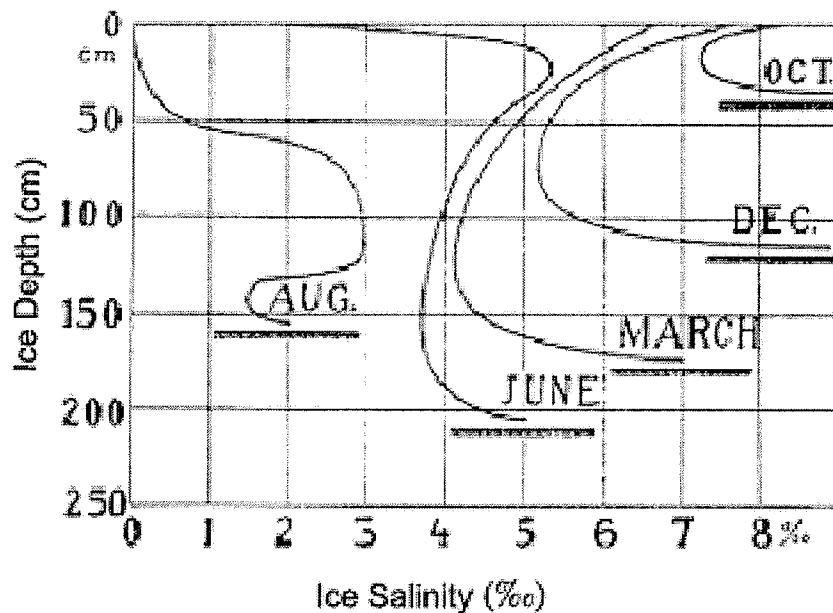


Figure 2.3. The vertical concentration of salinity for first year sea ice as it evolves from initial growth to drainage. (Adapted from Malmgren, 1927).

The thermodynamic properties of FYI are a function of the density of the ice and the impurities found within it, mainly air and brine (Papakyriakou, 1999). Cold

temperatures cause both brine and air expulsion in the upper portion of the ice volume creating typical FYI densities of 880 kg m^{-3} – 910 kg m^{-3} . These densities produce an average bulk thermal conductivity for FYI near $2.1 \text{ Wm}^{-1}\text{K}^{-1}$ (Hanesiak, 2001).

With the onset of melt, the structure of first year sea ice undergoes a dramatic transition in terms of temperature and structure. As temperatures within the ice approach -7°C there is a rapid increase in the brine volume within sea ice as a function of phase relationships (Barber et al., 2001). Brine pockets will align linearly and join together, re-establishing brine channels created due to gravity drainage. As water in liquid form collects at the surface of the snow – ice interface from melting snow (see section 2.2.2) it begins to seep through the ice following the brine channels. The drainage of fresh water results in a cleansing of brine from both the snow and the upper portion of the ice (Barber, 1993). In the absence of brine, a higher freezing point initiates a period of ice formation through the ice volume thus reducing further drainage of the surface and allowing for pond formation on the ice surface (Eicken et al. 2002). A period of ice growth at the ice – ocean interface also occurs as the influx of fresh water interacts with the mixing layer (-1.8°C). During this time congelation ice forms to the bottom of the FYI volume while the interaction of fresh water with the upper portion of the mix layer creates a false bottom ice layer up to 20cm thick, separating the mixed layer from melt water entering the system. Eicken et al. (2002) found that the formation of false bottoms leads to sub-ice fresh water ponding, which has a profound effect on

bottom ablation rates and radiative transfer previously unaccounted for in sea ice models.

Advanced melt is characterized by the complete ablation of snow due to increased ambient temperatures and corresponding solar absorption. The resulting increase in heat flux through the ice volume shifts the temperature gradient within the ice towards isothermal (Barber et al. 1999). Water is present throughout the ice volume and drainage through brine channels accelerates.

Towards the end of the melt season, the ice volume becomes isothermal and complete drainage of melt ponds from the surface occurs. With the removal of surface water the volume is termed dry ice. Dry ice is highly porous and shows an increase in salinity as seawater replaces melt water in the lower portion of the volume. At this point, depending on the length of the melt season, FYI will ablate into the ocean or it may last into freeze-up and become second year ice.

2.2.2. Snow

After initial ice formation, the timing and depth of snow accumulation sets the stage for the overall thickness of the ice, regulating temperature gradients and dominating mass and energy fluxes across the ocean – sea ice – atmosphere interface (Eicken, 2003; Papakyriakou, 1999). This is due to the low thermal conductivity of snow. The low thermal conductivity causes the snow to act as an insulating blanket for the sea ice, thereby modulating the conductive flux between

the ocean and the atmosphere (Iacozza and Barber, 1999). Snow also regulates the quantity and nature of energy available for biological production and provides significant amounts of fresh water to the marine environment during spring melt.

The deposition of snow over the marine cryosphere is bimodal in nature with the majority of snow accumulation occurring during fall freeze-up and spring ablation (Drobot, 1997). The lack of snowfall during the winter is largely due to the lack of significant weather systems as low atmospheric moisture results from the reduction of open water. The distribution of snow over the ice sheet is a combination of snowfall and aeolian transport resulting in an oscillation of depth orthogonal to the direction of prevailing winds (Yackel et al., 2000; Iacozza, 1997). Over FYI, these snow dunes, known as sastrugi, become wind swept leaving FYI with relatively thin snow cover following a consistent periodicity. This pattern is a result of the flat underlying ice and the lack of any large uplifted pieces that disrupt the surface wind field during depositional and erosional events (Iacozza and Barber, 1999).

By late winter, the snowpack overlying first year sea ice contains a series of layers representing various snowfall events and degree of metamorphism through the volume. After deposition, metamorphism of individual snow grains seeks a state of free energy equilibrium resulting in minimized surface area to volume ratios (Mätzler, 2002; Colbeck, 1982; Langham, 1981). Densities for snow in late winter average $350 - 400 \text{ kg m}^{-3}$ with levels of greater density near the middle of

the snowpack due to overburden and the temperature gradient through the volume.

The high ratio of air pockets to ice crystals within the snowpack results in snow having one of the lowest thermal conductivity of any surface on earth. Snow covering FYI has an average thermal conductivity of $0.4 \text{ Wm}^{-1}\text{K}^{-1}$ (Hanesiak, 2001; Colbeck, 1982). Thermal conductivity is further depressed in the lower region of the snowpack, known as the basal layer, due to the presence of brine (Papakyriakou, 1999). The unique thermodynamic properties of snow effectively insulate the lower ice from the cold atmosphere in winter by reducing conductive heat flux by as much as 50% (Eicken, 2003). The reduction in the conductive heat flux from the atmosphere limits ice growth to one to two meters in depth (Hanesiak, 2001; Lindsay, 2001; Jordan, 1991; Shine and Henderson-Sellers, 1985). This insulation effect also caps the upward flux of heat from the warm ocean into the lower atmosphere. This maintains an equilibrium thickness for sea ice which is a critical component in the hemispheric sea ice mass balance (Maykut, 1978).

Finally, the low thermal conductivity of the snowpack delays ice decay during spring melt, allowing for colder temperatures to persist within the ice volume after ambient temperatures reach the melting point. This reversal in the temperature gradient within the snow volume during early ablation results in snow melt at the snow – atmosphere interface while ice continues to grow via congelation at the ice – ocean interface, a process which can persist long into advanced melt (Eicken,

2003). Figure 2.4 shows the evolution of temperature across the OSA interface associated with different seasonal regimes.

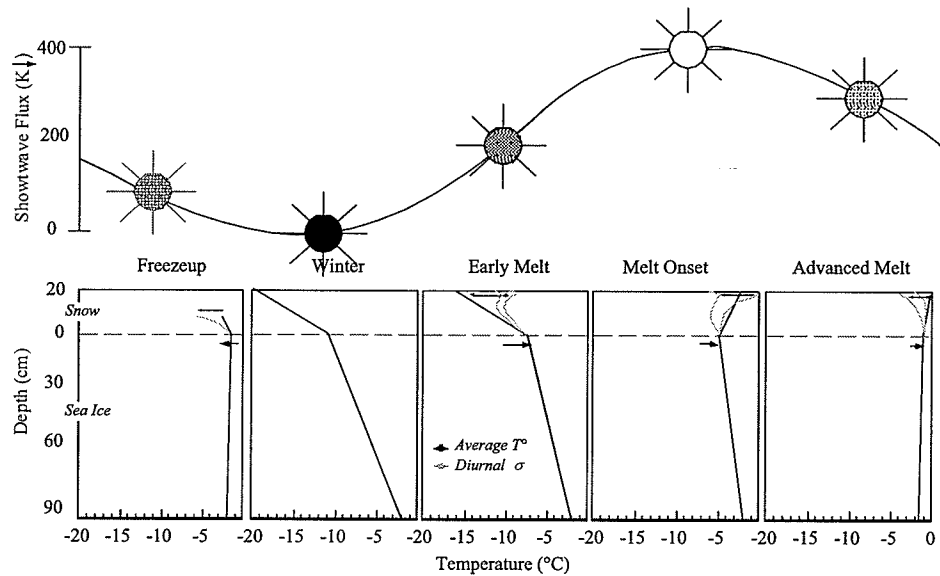


Figure 2.4. Categorical structures of the general thermodynamic regimes representing the seasonal transition from Freeze-up to Advanced Melt for snow-covered, landfast, FYI in the Canadian Arctic. The shortwave flux is recorded in Wm^{-2} . Temperature profiles are summarized from 10 years of in situ data. The available shortwave energy is denoted in summary above the thermodynamic profiles. Adapted from Barber et al. (1999).

The temperature gradient through the snowpack is further complicated due to the upward heat flux from the warm ocean below and the considerable amounts of brine at the snow – ice interface. Figure 2.4 shows the temperature of the ice near the ice – ocean interface remains constant through time at -1.8°C . The thermal properties of the ice volume maintain this temperature by regulating ice thickness to counter fluctuations in the atmospheric and/or oceanic heat fluxes through the annual cycle. Practically speaking, as temperatures decrease in

winter the sea ice – ocean interface temperature of -1.8°C is maintained with an increase of ice thickness and vice versa.

The kinetic grain growth in the basal layer creates unique thermodynamic properties due to low density and the wicking of brine (Papakyriakou 1999; Grenfell 1991, Wiscombe and Warren 1980,). The occurrence of warm air perturbations during winter reduces the atmospheric heat flux, warming the basal layer. The resulting increase in temperature across the snow – ice interface causes kinetic grain growth within the first 5cm – 10cm of the snowpack (Barber et al., 1995). A corresponding decrease in snow density and warmer temperatures creates a positive vapour gradient towards the snow surface which wicks brine into the basal layer. The wicking of brine creates a salinity concentration as high as 15ppt within the first few centimetres of the snowpack (Hanesiak, 2001; Drobot, 1997). The snow thermal conductivity is reduced in the brine-laden regions by at least 100% in most cases, (Papakyriakou, 1999) further reducing the amount of energy transferred between ocean and atmosphere.

As the atmosphere warms in spring, the temperature gradient across the OSA interface shifts, having warmer temperatures at the atmosphere – snow interface and cooler temperatures at the snow – ice interface (figure 2.4). This stage in the annual cycle is known as “early melt”. During early melt, the temperature gradient within the snowpack fluctuates following the diurnal nature of atmospheric heating and cooling and the volume goes through a series of

freeze/thaw cycles. The diurnal oscillations in the temperature profile represent a rapid growth period for snow grains throughout the snow layer (Barber et al., 2001).

Iacozza and Barber (2001) showed that the depletion of the snow cover over FYI is non-linear and during spring ablation, areas having a shallow snow depth exhibit an accelerated melt rate. The faster melt rate is due to the larger equilibrium metamorphic grains found to occur in the shallower snow cover (Barber and Nghiem, 1999). These larger snow grains create a lower surface albedo in the thinner snow cover due to the absorption of solar energy within the ice crystals, especially in the longer wavelengths. The increase in solar absorption contributes to the increase in the relative melt rate. During spring ablation melt ponds over FYI are initiated in the low points of snow drifts due to this increased melt rate for shallow snow (<16cm) (Iacozza and Barber, 2001). The initial development of melt ponds will be discussed in the following section.

When temperatures within the snow volume approach the freezing mark, water in liquid phase can be found throughout the snowpack and wet metamorphism of snow grains dominates the physical structure of the snow volume (Livingston et al. 1987). The presence of liquid water within the snow volume marks "melt onset". During this time, the snowpack goes through two types of snow regimes, pendular and funicular. Pendular and funicular snow regimes are very important to the physical and electromagnetic properties of the snow cover

due to increases of individual grain size, the formation of ice aggregates and the presence of liquid water within the snowpack (Barry, 1996; Mätzler, 1996; Perovich, 1996; Fukusako, 1990; Grenfell and Maykut, 1977).

As temperatures within the snowpack approach 0°C, liquid water becomes nestled in small fillets and veins between contact points of neighbouring ice grains creating crystal aggregates (Colbeck, 1982). Droplets of liquid water are held in suspension within the snowpack. This state of wet snow metamorphosis is known as the pendular regime. During the pendular regime air is continuous throughout the pore space and the liquid water occurs as isolated inclusions (Mätzler, 1987). The pendular regime will remain stable with water volumes less than 7%.

In the funicular regime, average daytime temperatures exceed 0°C, marking prolonged melting within the snowpack and water by volume in excess of 7% (Mätzler 1996; Colbeck 1982). Surface tension is no longer sufficient to hold water between crystals and water channels develop within the snowpack allowing water to freely drain toward the ice surface. With the breaking of bonds between ice crystals, individual grains grow to spherical shapes, further decreasing the strength of the snowpack. The snowpack is close to isothermal during the funicular regime and rapid ablation occurs.

The formation of water within the snowpack initiates two important physical changes across the OSA interface. First, the initial drainage of water to the ice surface causes flushing of salinity in the basal layer of the snowpack and

upper region of ice volume. Secondly, the rapid ablation of snow as the snowpack reaches an isothermal state causes a large influx of fresh water on the ice surface. This marks the formation of melt ponds on the ice surface and a transition to "advanced melt".

In the Arctic, the presence of melt ponds and open leads during the melt season is responsible for very high moisture content within the atmosphere creating a nearly continuous cloud layer (Grenfell and Perovich, 1984). The ubiquitous cloud cover during early spring enhances the longwave flux between the atmosphere and surface, accelerating snow and ice ablation (Barber and Thomas, 1998). As the melt season progresses, the reduction in surface albedo and an increase in shortwave energy will dominate the ablation of the FYI volume.

2.2.3. Melt Ponds

Melt ponds, or melt puddles, are a unique feature of the northern ice zone as they are rarely seen over southern hemisphere sea ice. Melt ponds have been at the centre of scientific inquiry for many years during spring melt as their presence initiates tremendous change across the OSA interface. In terms of the annual cycle of the marine cryosphere, the ponding on sea ice marks "advanced melt" which is characterized by the removal of the snowpack, a surge of fresh water to the upper portion of the ocean and a dramatic shift in the radiative properties across the OSA interface.

Melt ponds begin to form over smooth, landfast, first year sea ice when the amount of liquid water available at the surface exceeds the amount able to percolate through the ice volume (Eicken et al. 2002; Perovich et al. 2002). Iacozza and Barber (2001) found melt ponds developed in the troughs of sastrugi due to an increased melt rate in shallower snow. Initial melt water flushes brine from the lower snowpack and ice surface through brine drainage channels (Barber et al., 2001). However, as fresh water comes in contact with the super cooled ice volume, brine channels become plugged with the development of new ice. The reduction in the percolation rate through the ice volume results in melt water from the ablating snowpack to pool over the surface. This further erodes the remaining snow volume and exposes the ice surface to solar radiation. Over smooth ice, the rapid ablation of surface snow can result in pond fractions in excess of 80% before drainage channels form and stabilize the surface (Perovich et al. 2002; Yackel and Barber, 2000).

Several factors combine to control the size and extent of melt ponds. First, with the flooding of the ice surface, drainage channels are quickly established as seal holes, leads and cracks combine to provide melt water access to the underlying ocean (Grenfell and Perovich, 2004; Eicken et al. 2002). As the drainage of melt water progresses through drainage points, a web of drainage channels stretches out across the surface connecting ponds which eventually stabilizes the pond fraction of FYI near 50% (Perovich et al. 2002; Yackel et al. 2000). The effect of a single seal hole on the distribution of melt ponds can be

seen over hundreds of meters (Barber and Yackel, 1999). The ice surface progressively drains as it approaches these drainage points and a preferential drainage pattern develops having an increase in pond fraction radiating away from drainage points.

Secondly, the exposure of the dark ice surface at the bottom of melt ponds sets the stage for a dramatic shift in the radiative properties of FYI. Initially the frazil layer of the ice volume is flooded creating a pond bottom composed of white ice and air bubbles. Over a period of days, this initial surface ablates revealing the much darker columnar ice structure below. An increase in albedo allows for more solar radiation absorption which speeds ice ablation from the pond bottom, causing the ponds to deepen (DeAbreu et al. 1994). The deepening of ponds and subsequent thinning of the ice volume increases shortwave penetration and absorption over the ponded surface, further decreasing albedo and initiating sub-ice ablation below the pond. The melt pond albedo feedback mechanism accounts for the majority of pond deepening after initial surface flooding (Perovich et al., 2001).

Mechanical weathering also plays a role in pond development. This is especially true during initial pond onset when strong winds can cause substantial snow ablation from wave action along leeward pond edges. As wind crosses pond surfaces, the resulting friction causes water to be pushed to the leeward side of ponds creating an influx of water into snow or bare ice. This influx of water

accelerates the melting of ice crystals further increasing water on the ice surface and increasing pond extent. Wave action is also thought to aid in the release of bubbles held within the frazil layer of the ice volume. As the bottom of wind induced wave trains comes in contact with the submerged frazil ice, the impact breaks ice aggregates and trapped air bubbles are released.

Lastly, percolation of melt water along brine drainage channels ultimately dictates the degree of surface ponding and timing of complete pond drainage. During early melt, low permeability within the ice volume limits meltwater percolation thus allowing for melt ponds to form. However, once the ice warms to an isothermal state, the brine drainage networks become active and rapid drainage can occur, often within hours (Grenfell and Perovich, 2004). Eicken et al. (2002) used tracer studies to estimate percolation rates of melt water through FYI during summer. Their study found that due to freezing temperatures within the upper portion of ice volume during melt onset, melt water refroze upon infiltration of low-salinity, superimposed ice, plugging drainage channels creating a low-permeability ice layer. This effectively seals the upper ice volume due to reduced percolation rates, allowing for rapid pond formation over the first two or three weeks of the melt season. The study also found that the permeability of FYI varied more than two orders of magnitude as the melt season progressed. The increase in percolation rates toward the end of the melt season increases drainage rates beyond ablation rates, thereby leading to the removal of surface water.

2.3. The Optical Properties of Melting First Year Sea Ice

The optical properties of first year sea ice are intimately linked to the physical evolution of the FYI volume. The optical portion of the electromagnetic (EM) spectrum is defined as those wavelengths falling between 400nm and 700nm. Shortwave radiation is an alternate term commonly used to describe the peak wavelength range of EM energy from the sun (200nm and 4000nm) and is regarded as the climatically significant portion of the spectrum. The spectral range of shortwave energy represents the ultraviolet, visible and near-infrared segments of the EM spectrum or 250nm to 2500nm.

The absorption, reflection, and transmission of visible and infrared radiation by ice are fundamental processes governing ice thermodynamics and biological productivity beneath the ice (Perovich et al. 2002). During spring and summer, shortwave radiation dominates the surface energy balance (SEB) across the OSA interface (Shine and Henderson-Sellers, 1985). Over the melt season, the surface characteristics governing the SEB on landfast FYI is further complicated by an ablating ice surface composed, to varying degrees, of deep snow, bare ice, melt ponds and open water.

During spring melt, the albedo of sea ice is intimately related to the geophysical structure of both the snow and the ice volume (De Abreu et al. 1994). Recall from chapter 1 that albedo is the proportion of total incident solar radiation reflected from a surface relative to that which is incident, and that it represents a

scalar unit governing the amount of energy lost, either by transmission or absorption, to a surface. Spectrally integrated albedo is a function of solar zenith angle, atmospheric properties, cloudiness and surface characteristics (Warren, 1982). Ice and snow have similar bulk optical properties in the visible and near-infrared wavelengths so that reflectance in these wavelengths depends primarily on variations in the refractive index of ice and on snowpack characteristics (Barry, 1996; Perovich, 1996).

The presence of clouds also effects spectrally integrated albedo. As cloud thickness increases, incident radiation decreases across all wavelengths. The changes are strongest in the infrared because of the influence of the atmospheric water content, resulting in an increase in the ratio of visible-to-total irradiance (Barry, 1996; Grenfell and Perovich 1984; Warren, 1982). Total albedos under cloudy skies are typically 8-12% larger than clear sky values (Grenfell and Perovich 1984; Grenfell and Maykut, 1977). This results in clear sky albedo measures underestimating true all sky albedo values. This is an important consideration for modelers using optical remote sensing for albedo parameterization as these sensors record clear sky values.

Despite numerous studies by various research groups, (Grenfell and Perovich, 2004; Hanesiak et al. 2001; Yackel et al., 2000; Fetterer and Untersteiner, 1998; DeAbreu et al. 1994) little is know about the pattern of evolution regarding the optical properties of the icescape at the regional level.

Instead, bulk optical properties derived from surface studies are applied to aerial scenes and up-scaled to regional estimates. These estimates are then used to force model simulations of radiative transfer across the OSA interface used in local, regional and global climate models (GCMs).

Correct parameterization of sea ice albedo used in regional and global climate models is essential for proper treatment of the sea ice-albedo feedback operating over the marine cryosphere. The ice-albedo feedback is defined as follows: As temperatures increase, the extent of snow and ice is reduced, decreasing the surface albedo and increasing the amount of sunlight that is absorbed by the Earth-atmosphere system, and vice versa (Curry et al. 2001). In terms of the work presented here, the sea ice – albedo feedback is thought to be in part responsible for a reduction in sea ice extent. For example, reductions in ice extent due to perturbations in atmospheric heat transfer into polar regions exposes more of the ocean, which in turn increases the amount of solar heating, further amplifying ice retreat. (Eicken and Lemke, 2001).

The sea ice – albedo feedback has strong association with radiative transfer across the OSA interface. Lowering albedo increases the amount of solar radiation available to both the cryosphere and hydrosphere through the absorption and transmission of shortwave energy through the FYI volume. The internal absorption of solar radiation contributes directly to the thermal energy of the snow/ice volume affecting both heat diffusion and snow/ice metamorphism

(Eicken, 2003; Papakriakou, 1999; Colbeck, 1982). Radiative transfer theory associates numerous bulk FYI properties such as albedo, thermal gradients and physical morphology to determine the path and type of interaction spectral energy follows through the OSA interface (Curry et al. 2001). Figure 2.5 illustrates various aspects of radiative transfer through FYI.

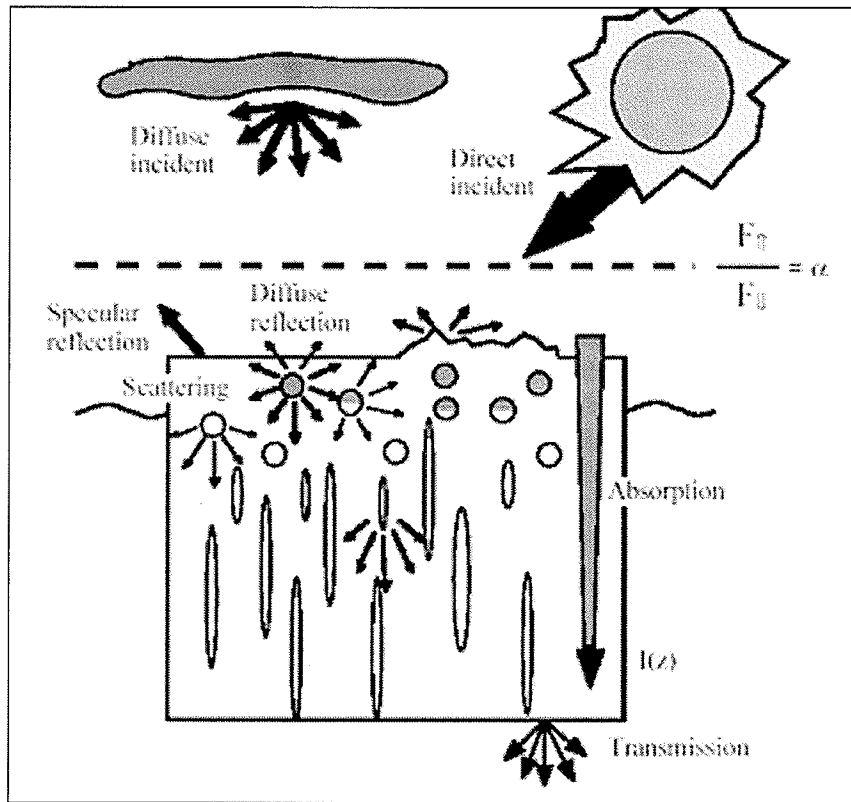


Figure 2.5. Schematic depiction of sea-ice radiative transfer processes across the OSA interface where F is equal to total solar radiation (adapted from Perovich, 1996).

In this chapter I examine the effect of physical changes within the OSA interface on the spectrally integrated albedo over landfast FYI. An examination of

the evolution of albedo as it changes from a winter snow covered medium to one made up of ablating ice and melt ponds during spring ablation will further focus my discussion.

2.3.1. First Year Sea Ice

The optical properties of first year sea ice are of little concern during winter, as the system receives no solar radiation. In spring, when the sun rises above the horizon, an optically thick snow layer scatters the majority of incident solar radiation back towards the atmosphere with only a small portion of energy, mainly in the blue region of the spectrum, penetrating the ice volume (Perovich, 1996; Warren, 1982). It is not until advanced melt, when the snowpack is rapidly ablating and the surface of the ice becomes exposed to direct solar irradiance that the optical characteristics of ice begin to gain significance. Sea ice optical properties depend on ice thickness, the relative proportion of brine and air inclusions within the ice volume, and surface conditions such as surface roughness (Perovich, 1996).

During the melt season most of the brine drains out of the upper layers of the ice producing a "surface scattering layer" composed of granular decomposing ice which persists throughout the melt season (Perovich et al. 2002). The scattering layer maintains the albedo of unponded ice at a stable level near 0.60, through the remainder of ice ablation (Perovich et al., 2002; Hanesiak et al., 2001; Barry, 1996). The thickness of this scattering layer is determined by a balance in the

rates of surface ablation due to surface heat fluxes and the rate of internal melting and brine drainage owing to the absorption of shortwave radiation (Grenfell and Perovich 2004).

At times of rapid pond drainage, columnar ice becomes exposed at the surface. Pore space between crystals is saturated with meltwater, which fill in near-surface irregularities so that backscattering is reduced which further increases the transmission of optical energy into the volume (Grenfell and Perovich, 1984). Maximum transmission of optical energy has been found to be at a wavelength of 470nm (Barry, 1996; Perovich, 1996; Warren, 1982). This results in the maximum scattering of blue wavelength and the characteristic blue colour of thick FYI. The longer optical wavelengths which penetrate the ice volume are scattered or absorbed within 50cm of the ice surface. Typical blue ice albedo ranges from 0.29 to 0.32 with a characteristic peak in the blue portion of the spectral albedo (Hanesiak et al. 2001a; Perovich, 1996).

2.3.2. Snow

Snow optical properties depend on grain size and shape, depth of the snow layer and the optical properties of the underlying surface (Mätzler, 2002; Barry, 1996; Warren, 1982; Grenfell and Maykut, 1977). Within the visible region of the EM spectrum, the albedo of snow due to scattering of wavelengths is high since absorption is very low. However, near-infrared albedo is lower because both water and ice exhibit high absorption across this bandwidth. Beyond 5cm, snow is

considered optically thick (Grenfell and Perovich, 1984). Warren (1982) found that 98% of snow albedo is achieved with only 3cm of snow and that only a few millimetres of snow can dramatically raise the albedo of thick sea ice.

New snow has the highest albedo. The small grain size of newly fallen snow crystals effectively scatters incident optical energy, creating typical albedo values between 0.8 and 0.9. As the snowpack ages, albedo decreases across all wavelengths. This is due to an increase in grain size and the rounding of edges from dry snow metamorphosis which reduces the effective volume scattering within the snowpack (Barry, 1996). A photon has a chance to be scattered only when it crosses an air – ice interface and it has a chance of being absorbed only while passing through the ice. An increase in grain size brings about an increase in the path length that must be traveled through the ice between scattering opportunities (Warren, 1982). The largest changes to albedo in an aging snowpack occur in the infrared, where absorption by ice and water is very large and the upward scattered radiation is very sensitive to the scattering properties of individual grains at the surface (Grenfell and Perovich, 1984). Typical aged snowpack albedos under cold conditions range between 0.8 and 0.85 (Hanesiak, 2001; Fetterer and Untersteiner, 1998; DeAbreu et al., 1994; Perovich, 1996).

With the onset of melt, liquid water begins to form within the snowpack. During both the pendular and funicular regimes, wet snow metamorphosis stimulates crystal grain growth and water collects within the snowpack. The

formation of ice aggregates along with the addition of water combine to further decrease the albedo of melting snow (Hanesiak, 2001; Yackel, 2001; Barry, 1996; Mätzler, 1987; Warren, 1982). The effect of liquid water on snow albedo is simply to increase the effective grain size, because the refractive index contrast between water and ice is very small (Warren 1982). Typical wet snow albedo has been reported between 0.6 – 0.66.

Finally, solar zenith angle also plays a role in total albedo over snow. Visible light achieves near complete transmission through snow, however, light is scattered as it passes through individual snow grains. The volume scattering component of the snow volume makes it the most isotropic reflector of all natural surfaces on Earth, yet it still exhibits substantial anisotropy. The anisotropy is greater in the near-infrared than in the visible, because as absorption increases due to increasing grain size, the bi-directional reflectance pattern becomes dominated by the single-scattering phase function (Warren, 1982). When the incident direct beam component is significant, both spectral and total albedos increase as the solar zenith angle increases due to enhanced specular reflection and to forward scattering, thus allowing the photons to escape the medium faster (Perovich, 1996). Due to the angular dependence of snow albedo Warren (1982), reported an increase in albedo of 4% when measurements were taken along sun facing slopes of sastrugi compared to flat measurements.

2.3.3. Melt Ponds

Melt pond albedos are a function of reflection, absorption and transmission of wavelengths through the overlying water volume and the underlying ice. Scattering by underlying ice has the greatest influence on albedo, ranging from 400nm – 600nm where the pond water is most transparent resulting in a blue colour due to ice volume scattering (Perovich et al. 2002; Perovich, 1996). A characteristic linear decrease in albedo from 600nm – 800nm is observed over melt ponds as absorption within water becomes an increasingly dominant factor for reducing albedo. Above 800nm, absorption in the water is so great that pond albedo is essentially determined by Fresnel reflection at the surface and is independent of wavelength (Perovich, 1996). This trend can be seen in the near identical spectral albedo of varying pond depths between 800nm and 1100nm (Hanesiak et al. 2001b; DeAbreu et al. 1994; Grenfell and Maykut, 1977).

The visible albedo of melt ponds continually decreases as the melt season progresses. When melt water floods the FYI surface during advanced melt, initial melt ponds form over the frazil layer of the ice volume. The frazil layer is highly porous creating an extremely efficient scattering surface similar to the scattering layer described for drained FYI. A mainly white pond bottom with high bubble density and correspondingly high albedo across all wavelengths is typical of this surface type when compared to mature ponds. Hanesiak et al. (2001b) refer to

this type of melt pond as a 'light pond'. Typical albedo values for young melt ponds are 0.21 – 0.33.

As bubbles are released from the ice structure due to ablation and mechanical weathering, the columnar structure of the lower ice volume is exposed. With the removal of the frazil layer, albedo continues to decrease across all wavelengths with increased pond depth (Fetterer and Understeiner, 1998; Grenfell and Maykut, 1977). This is a result of the ablation of the ice to a point where it is no longer optically thick (<50cm), exposing the optical properties of the ocean volume (Maykut and Grenfell, 2001; Hanesiak, 2001; DeAbreu et al. 1994). Observed albedos for well developed deep melt ponds are 0.15 – 0.21. The low albedo of mature melt ponds accelerates the melt rate of the underlying ice volume to 2 – 3 times the rate of bare ice (Fetterer and Understeiner, 1998).

Light levels beneath ponded first year sea ice are at least a factor of three greater than those beneath the scattering layer of decomposing ice of the same thickness (Grenfell and Maykut, 1977). Recent work on the radiative flux across the OSA interface has shown that this estimate may be quite conservative. Data collected during the Surface Heat Budget of the Arctic Ocean (SHEBA) showed a surprisingly large amount of heat in the summer mixed layer, leading to total mass ablation at the underside of the ice pack that were comparable to those at the upper surface (Eiken et al. 2002). The origin of this heat appears to have been largely solar radiation transmitted through the ice pack (Maykut and Grenfell,

2001). This led Grenfell and Perovich (2004) to dub melt ponds as “skylights to the ocean”.

So far I have discussed the optical characteristics of surfaces representative of melting FYI. However, I have not taken into account the spatial distribution of these surfaces nor their contribution to regional albedo. Due to the importance of melt ponds on the SEB over FYI, numerous researchers have attempted to combine local surface optical properties to aerial imagery in order to up-scale local measurements. Currently this mode of investigation is still in its infancy with each set of researchers developing their own approach for interpolating physical and optical characteristics to digital stills.

Derksen et al. (1997) used a tethered balloon held 300m above the ice as a platform to take photographs of a surface composed of MYI and FYI. Analysis of the imagery found good agreement between the intensity of digital values and surface albedo over a ten day period. This relationship led to the development of 5 discrete bulk surfaces with associated observed albedo and physical characteristics based on density slicing of the image histogram to corresponding intensity levels. Although simple in nature, this type of approach allowed for estimates of pond fraction and visible and near – infrared albedo for an evolving melt surface composed of both FYI and MYI. Over the 10 day period, Derksen et al. (1997) found pond fraction to increase in a linear fashion from 0.0 to 0.5.

More recently Yackel and Barber (2000) and Hanesiak et al. (2001b) used aerial photography from aircraft flights to estimate physical and optical properties over landfast FYI. Intensity levels were again associated with surface types but a more sophisticated method allowed for perimeter lengths and average pond size to be calculated over large segments of FYI. The bulk characteristics of four surface classes were used in this investigation (dry snow, wet snow, light pond and dark pond). Aerial surveys showed considerable variation in both pond fraction and albedo. This was explained by preferential drainage in areas with direct access to the ocean such as seal holes and leads. Average albedo was calculated to be 0.55, with a pond fraction of 0.5 around the midpoint of the melt season.

Tschudi et al. (2002) and Perovich et al. 2002 used a similar method for establishing surface variability. Five low altitude flights were conducted in 1998 over pack ice composed of MYI and FYI during the melt season. The researchers used an algorithm which determined surface types by examining differences between the blue, red and green channels of digitally captured imagery. Five bulk surface types were determined: open water, snow, bare ice, light melt pond and dark melt pond. Again considerable heterogeneity was seen across the surface. A relationship between pond fraction and albedo was observed with average albedo estimates below 0.5 by the end of the melt season.

The results of each of these methods have shown that there is considerable heterogeneity in both the spatial and temporal pattern over different ice surfaces.

Understanding these distributions at the regional level will allow for better representation of surface energy balance variability acting across the ocean – sea ice – atmosphere interface in both the spatial and temporal dimension. These studies also show a lack of high temporal resolution aerial observations during this highly dynamic season. Tshudi et al. (2002) have presented the most comprehensive regional time series with 5 datasets captured during the 1998 melt season. However, considerable variation in surface characteristics was also observed during this time, especially during initial melt pond development and drainage. A more detailed temporal examination of the surface is needed.

2.4. The Microwave Properties of Melting First Year Sea Ice

The use of passive and active microwave remote sensing has proven to be a powerful tool for the observation of snow and ice (e.g. Yackel, 2001; Parkinson et al., 1999, Barber 1993, Tucker, et al. 1992, Ulaby et al. 1986). This is due to several factors, namely the coherent transmission of microwaves through the atmosphere, independence from solar input, their sensitivity to water in liquid phase, and brine – temperature relationships. These properties allow for year-round, continuous monitoring of polar regions which are often shrouded in cloud and darkness.

Active microwave systems, and in particular synthetic aperture radar (SAR), have been used for monitoring the temporal evolution of sea ice as it changes from winter to summer (e.g. Breneman, 2003; Hanesiak et al., 2001b; Kirk, 2001; Yackel, 2001; Barber and Nghiem, 1999; Carlström, 1995; Barber, 1993; Livingston et al., 1987; Ulaby et al., 1986). The utility of SAR is largely due to changes in the physical nature of the snow – ice medium as it progresses from cold, dry winter conditions to warm, melting spring conditions. Although the transition is observable over various ice types, the transition to spring is most distinguishable over smooth, thick, first year sea ice (FYI) (Yackel et al., 2000). The response of SAR is seen because of the sensitive dielectric nature of water held within the snowpack, the formation of melt ponds on the surface, (Hallikainen, 1986; Tiuri et al., 1984; Stiles and Ulaby, 1980; Mätzler, 1987) and the quantity of

brine in suspension found in the basal layer of snow at the snow – ice interface (Yackel, 2001; Barber et al., 1995; Drinkwater and Crocker, 1988).

Wavelength and polarization of the incident energy, viewing geometry of the sensor, surface roughness and the dielectric nature of the media all contribute to dictate the overall signal return recorded by the sensor. Unlike radiometers, which have a field of view (FOV) centred at nadir, SAR scatterometers transmit and receive microwave energy from a look angle that is off axis from nadir. The viewing geometry for a SAR satellite platform is illustrated in figure 2.6.

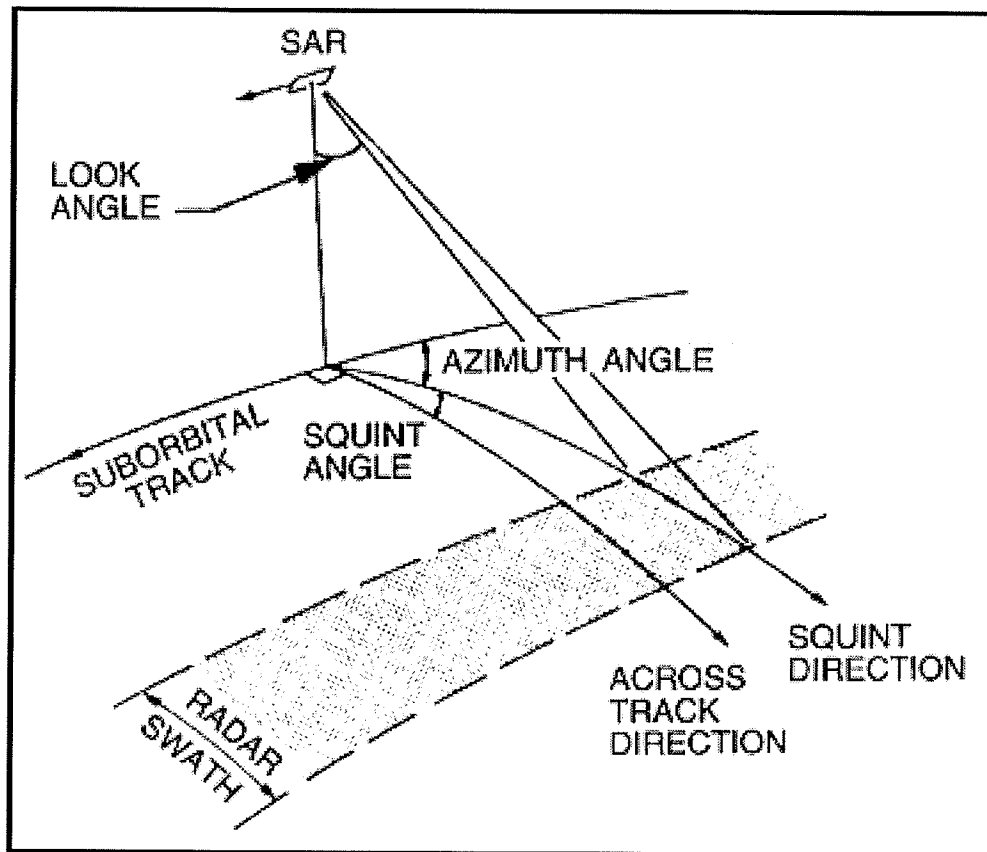


Figure 2.6. The viewing geometry of synthetic aperture radar (SAR). The look angle for RADARSAT-1 ranges from 20° to 49° from nadir. Adapted from Henderson and Lewis (1999).

The magnitude or intensity of power returned to the sensor is dependent on how the microwave energy interacts with the physical and dielectric characteristics of the surface and on the incidence angle of the pulse (Ulaby et al., 1986). The technical parameters controlling power returned to the sensor are shown in equation 2.1.

$$P_R = P_T (\sigma \cdot A) \frac{G^2 \cdot \lambda^2}{4\pi^3 \cdot R^4} \quad [2.1]$$

Where P_R is the power returned to the sensor, P_T is equivalent to the power transmitted, σ equals the radar cross section, A is the total area of the radar cross section, G represents the gain of the transmitting antenna, λ is the wavelength of the microwave sensor and R is the range/distance to the target. Notice that with the exception of the radar cross section, each variable is predetermined by the technical specifications of the sensor. In contrast, the radar cross section is determined by the surface and/or the volume characteristics that the microwave energy comes in contact with. Power is generally expressed as a total backscattering coefficient (σ^0) in decibels (dB) following equation 2.2.

$$\sigma^0 = 10 \bullet \log_{10} P_R \quad [2.2]$$

Within various layers of the OSA interface, mainly ice crystals, liquid water, air and brine, the amount of energy able to pass to lower levels is a function of the dielectric nature of individual elements. Within the dielectric term wetness, salinity, temperature and grain size all play a major role in determining the dielectric constant (ϵ^*) of the system (Nghiem et al., 1996; Barber, 1993; Tucker et al., 1992; Mätzler, 1987; Ulaby, 1986; Turi et al., 1984), (figure 2.7).

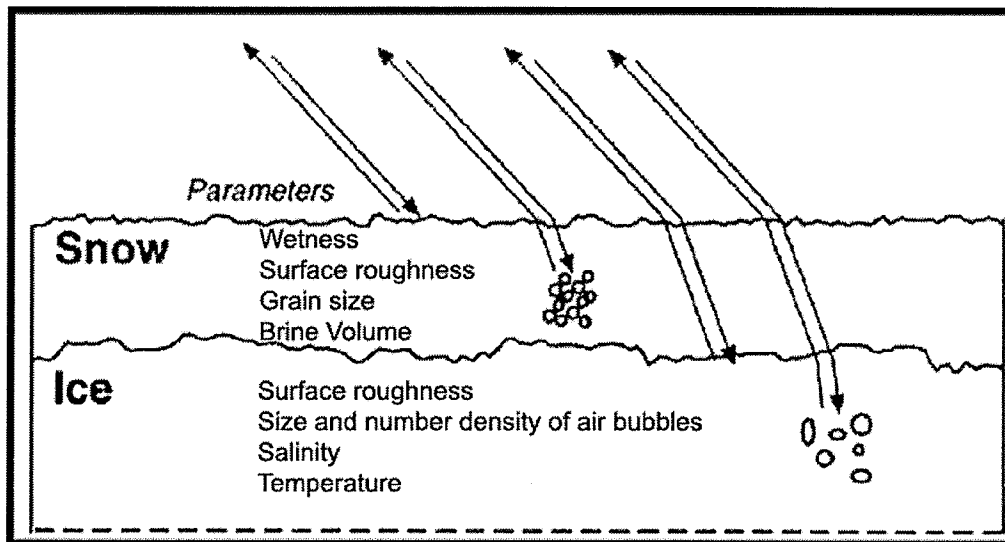


Figure 2.7. Sea ice dielectric parameters and interfaces (adapted from Carlström, 1995).

Here we define the OSA interface as three distinct dielectric mediums: air, snow and FYI. The relative scattering cross section (σ^0), or backscatter, recorded by the sensor becomes a combination of surface and volume scattering as the penetrating energy passes through the atmosphere – snow boundary, the snow volume, the snow – ice boundary and finally the ice volume following equation 2.4. Scattering at microwave frequencies is dependent on the snow density, correlation lengths of ice, brine, air and water held within the snow/ice volume, and the dielectric characteristics of the different scattering elements at a given depth within the OSA interface (Barber and Nghiem, 1999).

$$\sigma_{total}^{\circ}(\theta) = \sigma_{ss}^{\circ} + \psi_{as}^2(\theta) * \sigma_{sv}^{\circ}(\theta') + \psi_s^2(\theta) * \sigma_s^{\circ}(\theta') \quad [2.4]$$

Where σ_{total}° represents the total backscattering coefficient, θ is the incidence angle of the illumination beam, θ' is the Fresnel refraction angle, σ_{ss}° is equivalent to the backscattering at snow surface, ψ_{as}^2 is the transmission coefficient across air – snow interface, σ_{sv}° equals backscattering within the snow volume, ψ_s^2 is the transmission coefficient across the snow – ice interface and σ_s° represents backscattering from the ice volume. In the following sections, each element influencing backscatter during the spring ablation period will be explored.

2.4.1. The Role of Dielectrics in Snow and Ice

Dielectric properties are important in microwave remote sensing because they define the electrical conductivity of the material relative to the wavelength and polarization of the incident energy (Barber *et al.* 1999). The dielectric constant is made up of a complex number consisting of a real (ϵ') term and an imaginary ($j\epsilon''$) term as outlined in equation 2.5 (Henderson and Lewis, 1999).

$$\epsilon^* = \epsilon' + j\epsilon'' \quad [2.5]$$

Where ϵ^* equals the dielectric constant, ϵ' represents the dielectric permittivity, ϵ'' is the dielectric loss and j is an imaginary number ($\sqrt{-1}$). A pure dielectric does not conduct electricity. As such, for a given unit of energy of known frequency, the amount of energy able to interact with a medium will be reduced as the value of ϵ^*

increases. Dielectric permittivity is defined as the degree to which a medium resists the flow of electric charge while dielectric loss represents the amount of energy retained by the material. In the lower half-space occupied by sea ice, snow, and seawater, ϵ^* takes a wide range of values, often with a large imaginary part (ϵ'') in the various media that are encountered, such as pure ice, brine, air, fresh water, and sea water (Grenfell *et al.*, 1998).

Dielectric mixture models are used to estimate the complex dielectric constant for multiple media interfaces such as the OSA interface. The models provide insight into the nature of energy interaction as a penetrating pulse of energy passes through a medium by providing a physical basis from which changes in backscatter can be explained. Dielectric mixing formulae are based on the assumption that a heterogeneous medium reacts electromagnetically as a homogeneous medium with an effective dielectric constant, ϵ^* (Mätzler, 1987). The effective dielectric constant is calculated for a specified frequency by weighting individual constituent dielectrics, such as the density of brine, water (liquid, solid and vapour) and air, through the medium for specific frequencies. For a detailed look at dielectric mixture models the reader is directed to the work of Nghiem and Bertoia, 2001; Nghiem *et al.*, 1996; Nghiem *et al.*, 1995; Barber, 1993; Drinkwater and Crocker, 1988; and Vant *et al.*, 1986.

2.4.2. Surface and Volume Scattering Over FYI during Spring Ablation

Scattering of microwave energy is dependent on the dielectric nature of the medium with which the illumination beam comes in contact. Sea ice and snow are heterogeneous materials composed of ice, brine and air pockets. The distribution of these elements within the snowpack along with temperature and the presence of liquid water all combine to dictate ϵ^* for a medium (Carlström, 1995; Barber, 1993; Hallikainen et al., 1986). Air has a dielectric constant of ~ 1 ; dry snow ~ 2 ; saturated snow ranges from 2.5 to 6; thick FYI is about 3.5; and brine found within the basal layer of the snow at the snow – ice interface is in the order of 70. So long as the dielectric mismatch between two adjacent volumes is sufficiently high, scattering will occur along its interface (Barber, 1993). Thus, as the temperature rises during the transition from winter to spring, the proportion of brine, ice, air and liquid water found within each medium, mainly brine and water, determine the dielectric behaviour across the OSA interface.

During spring ablation the distribution of brine and liquid water within the snowpack and on the surface of the icescape greatly influences the backscatter recorded by the sensor (Yackel and Barber, 2000). In terms of the OSA interface over FYI there are two types of scattering which contribute to σ^0 ; surface and volume scattering. The concentration of liquid water and brine within the snowpack and bare ice scattering layer creates volume scattering, whereas the pooling of melt water over the icescape provides a surface scattering interface.

The spatial concentration of each of these scattering mediums will directly influence the scattering characteristics of the microwave illumination beam and thus dictate the amount of backscatter detected by the sensor.

The backscatter of a pixel can be considered to be the sum of the energy returned from all of the scatterers within the pixel (Jeffries et al., 1997). Low resolution SAR data used in this thesis has a nominal pixel resolution of 100m². Therefore the backscatter recorded by the SAR platform becomes a function of the relative fractions of surface scattering from ponded water, and volume scattering from snow/deteriorated ice present within each pixel following equation 2.6.

$$\sigma^{\circ} = 10 \log_{10} [f_m \cdot 10^{(\sigma_m/10)} + (1 - f_m) \cdot 10^{(\sigma_i/10)}] \quad [2.6]$$

Where σ_m and σ_i are the estimated backscatter coefficients for melt ponds and bare ice respectively and f_m is the surface fraction of melt ponds. Volume scattering contributes to the value of σ_i and will dominate σ° during the pendular snow regime and within the bare ice scattering layer once the snowpack has ablated. During these periods of spring ablation backscatter is the result of diffuse volume scattering within the snow/bare ice volume. In contrast, surface scattering will dominate σ° during the funicular snow regime and over melt ponds when the surface of ponds become wind roughened. In both of these cases liquid water on the surface of FYI creates the interface for surface scattering and σ° is due to surface roughness caused by uneven drainage within the snowpack (in the case of

the funicular regime) and wind (in the case of melt ponds). Each of these stages will be explored in greater detail in subsequent sections.

2.4.3. The Effect of Incident Angle on SAR Backscatter

The power returned to the sensor for any isotropic surface will diminish with increased incidence angle (Barber et al., 1999). The effect of incidence angle is also dependent on the type of scattering dominating σ^0 . As volume scattering results in a diffuse signal, the effect of a variable angle of incidence is relatively small. In contrast, due to the specular nature of surface scattering, the effect of incidence angle results in a considerable decrease in signal return with increasing incidence angle (figure 2.8). RADARSAT-1 data, used in this thesis, collected while operating in standard beam configuration offers imaging from a variety of incidence angles. As a result, the effect of diminishing backscatter with increasing incidence must be taken into consideration.

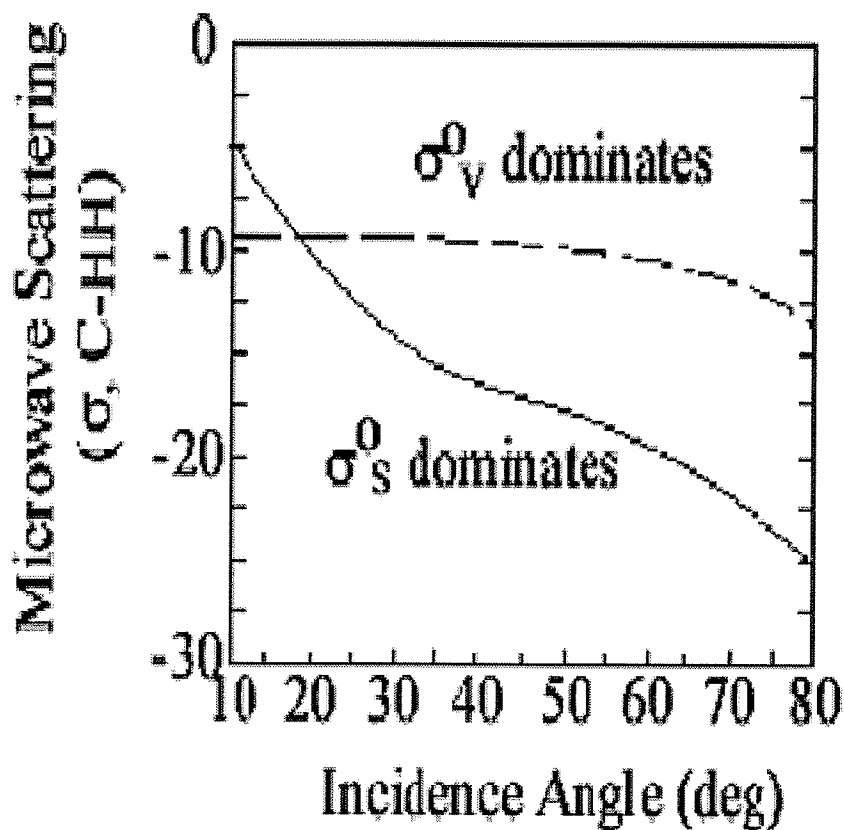


Figure 2.8. Differences in backscatter versus incidence angle for surface (σ_s^0) and volume scatters (σ_v^0). The proportion of ice and melt ponds within a given pixel will dictate whether the backscatter is dominated by surface or volume scattering (adapted from Barber, 1993).

A method for correcting for the effect of incidence angle has been developed by Yackel and Barber (2000). This method assumes that over an isotropic surface, the backscatter can be normalized to a fixed incidence angle. This method is only valid so long as changes in σ^0 can be attributed strictly to changes in incidence angle. During winter, the temperature at the snow/ice interface is cold ($<-11^\circ\text{C}$) and the dielectrics of the FYI volume can be assumed constant. Thus, any change to SAR backscatter during this time is a function of

surface roughness and incidence angle. Assuming that the region of interest is smooth FYI, the roughness term can be eliminated and changes in backscatter are solely a function of incidence angle. Plotting the change in backscatter with increasing incidence angle allows for development of a model which quantifies the changes in backscatter due to incidence angle. This incidence angle correction model is shown in equation 2.3.

$$\Delta\sigma^{\circ} = \sigma_{(\theta)w}^{\circ} - \sigma_{(\theta)}^{\circ} \quad [2.3]$$

Where $\Delta\sigma^{\circ}$ is the change in backscatter from winter conditions (incidence angle corrected value), $\sigma_{(\theta)w}^{\circ}$ is the backscatter at a given incidence angle from the winter model and $\sigma_{(\theta)}^{\circ}$ is the seasonally observed backscatter for the corresponding incidence angle.

2.4.4. The Effect of Wind on SAR Backscatter

Over the course of the melt pond ablation period, SAR signatures take on a wide range of values. The variability in σ° has been shown to be a function of pond fraction, incidence angle and wind speed (Yackel and Barber, 2000). As the effect of incidence angle can be quantified and corrected for, the fluctuations in σ° during the melt pond season is reduced to pond fraction and wind speed. In this section, a brief look at the effect of wind speed on SAR signatures during the melt pond season will be addressed.

Recall that during the melt pond season two backscattering terms contribute to the overall σ^0 observed by the sensor; backscatter due to volume scattering over bare ice (σ_i) and backscatter due to surface scattering over melt ponds (σ_m). Under calm conditions, σ^0 is dominated by volume scattering within the bare ice patches as the dielectric mismatch at the atmosphere – melt pond interface causes specular reflection of the incident energy away from the sensor. Due to specular reflection and depending on pond fraction, typical backscatter over an ablating FYI surface during calm conditions is low and ranges between -24dB for pond fraction approaching 100%, increasing to -12dB over areas with no ponding. However, as wind velocity increases, friction between air particles traveling across the surface of the melt ponds causes sinuous wave trains to develop. The effect of wave trains is to roughen the pond surface sufficiently enough for surface scattering to contribute to backscatter. The amplitude of these sinusoidal wave trains, and thereby their effect on σ^0 , is a function of wind speed and pond fetch length.

Yackel and Barber (2000), found that 90.3% of the variability in σ^0 can be explained by incidence angle and wind speed. They also found that backscatter is dominated by surface scattering when wind velocity increases beyond 3ms^{-1} , becoming increasingly distinguishable from volume scattering with increasing velocity. Further, they reported that between 1.5ms^{-1} and 2ms^{-1} , backscatter from volume and surface scattering is approximately equal, making the determination of pond fraction almost impossible. The researchers had no data for calm conditions.

2.4.5. The Use of SAR for Determination of the Geophysical Properties of Landfast Smooth FYI.

With the explanation of SAR backscatter quantified for the effect of surface and volume scattering, incidence angle and wind during spring ablation, an examination of the temporal trend of SAR backscatter can be made. Time series synthetic aperture radar has been used primarily to determine the onset of melt for both MYI and FYI surfaces. Due to the physical and dielectric evolution of snow, FYI and melt ponds time series SAR has a distinctive pattern beginning with the presence of water within the snowpack (figure 2.9). Although successful for determining the timing of pond onset, time series SAR has had limited success for the determination of the physical evolution of a ponded marine cryosphere once melt ponds have formed on the surface (e.g. Yackel and Barber, 2000; Fetterer and Untersteiner, 1998; Jeffries et al., 1997). This is mainly due to the difficulty in isolating the proportion of backscatter due to ponded surfaces (σ_m) and bare ice (σ_i).

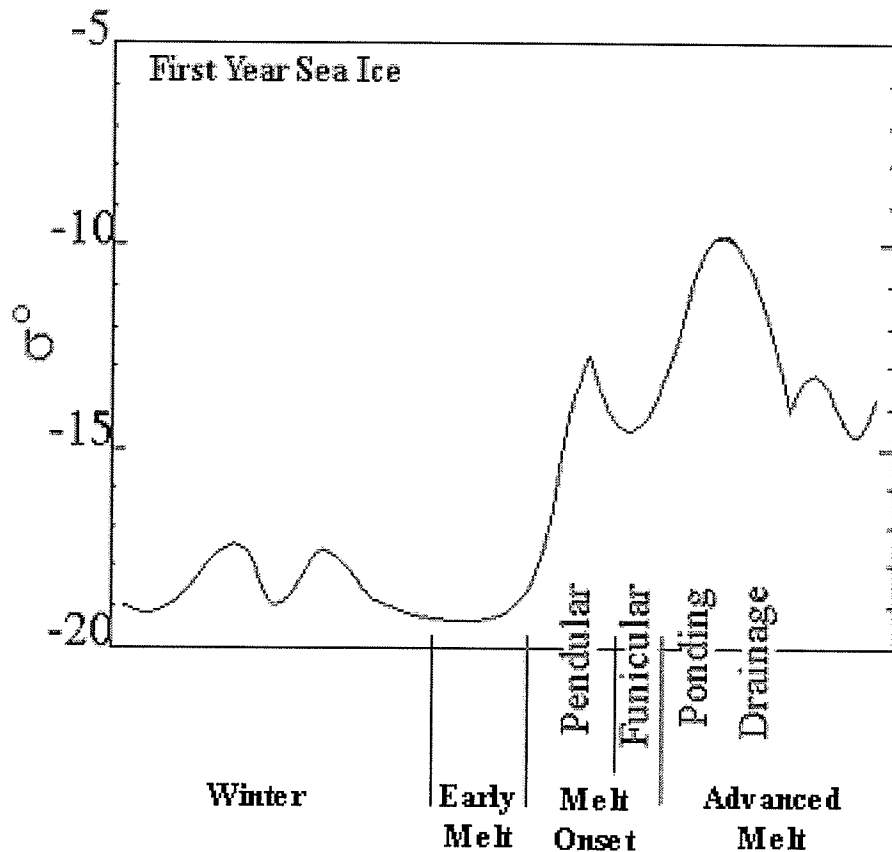


Figure 2.9 Evolution of first-year sea ice from winter to advanced melt as seen by time series SAR backscatter. Adapted from Barber et al., 2001.

Although limited in number, the majority of studies examining the relationship between σ° and pond fractions has been done over Arctic pack ice composed primarily of MYI (e.g. Fetterer and Understeiner, 1998; Jeffries et al., 1997; Onstott and Gogineni, 1985). Recently, Barber and Yackel (1999) and Yackel and Barber (2000) have shown a statistical relationship between σ° and pond fraction over landfast FYI using in situ pond fractions extrapolated from aerial photography. The following sections will outline the influences of snow, ice and melt ponds on σ° as the season progresses from winter through to the summer.

2.4.5.1. First Year Sea Ice

From a microwave scattering standpoint, during winter the dielectrics and small grain size of the overlying snowpack are such that scattering within the upper snowpack contributes only a fraction of the total backscatter and most of the microwave energy is free to interact with the basal snow layer and ice volume. First year sea ice has two distinct layers, the frazil layer and the underlying columnar layer.

The concentration of both air and brine found within the structure of FYI is determined by the rate of formation during fall freeze-up. During winter, periods of cold temperature cause brine expulsion in the upper portion of the ice volume as ice platelets squeeze together. The expulsion of brine and air from the upper portion of the ice results in a decrease in brine volume within the ice structure and a concentration of brine forms along the ice surface. The presence of brine along the smooth ice surface has a sufficiently high dielectric mismatch to ensure the majority of energy is scattered away from the sensor at the snow – ice interface during cold conditions (Kwok and Cunningham, 1994).

The limited amount of energy penetrating across the snow – ice interface is free to interact with the FYI volume. The relatively high density of air and brine pockets within the frazil layer, as compared to the columnar ice below, provide sufficient scattering radii for volume scattering to be a measurable component of the microwave signature. Scattering within the frazil layer greatly diminishes the

amount of energy available to the columnar layer at 5.3GHz, thus eliminating this layer from our discussion. Cold FYI is characterized by low levels of signal return leaving any σ^0 observed by the sensor ($<-18\text{dB}$) as a function of volume scattering within the frazil layer of the ice volume and brine migration into the basal layer of the snowpack, snow depth, and/or small scale variations in surface roughness (Barber and Nghiem, 1999).

Melt onset marks a transition from surface scattering at the snow – ice interface to volume scattering within the snow surface. Increases in water and brine volume within the snowpack due to an increase in the atmospheric flux create scattering radii, initiating volume scattering. During this time, the snowpack volume scattering component of the backscatter will dominate, leaving the ice virtually invisible to the sensor. The ice surface will remain undetectable until the snowpack completely ablates revealing the bare ice surface scattering layer (see discussion on snow scattering below).

With the removal of snow and brine and the formation of melt ponds during the advanced stages of spring melt, the ice surface becomes evident once more. The presence of the surface scattering layer formed through surface ablation (described in section 2.3) results in the ice surface contributing volume scattering to backscatter observed by the sensor. During advanced melt the surface of the ice is saline free with the majority of scattering due to large wetted ice agglomerates, with grain sizes of 0.5cm – 1.5cm and depths of 3cm – 10cm. A

moderate and stable backscatter value of -12dB is generally observed by the sensor and is representative of deteriorated bare ice during this time (Jeffries et al., 1997).

2.4.5.2. Snow

During winter σ^0 is low and stable with only small variability in σ^0 observed. The low density of ice crystals within the snow volume creates a sufficiently low dielectric constant for near complete transmission of microwave energy at 5.3GHz, leaving the surface of the ice the dominant scattering interface. Settled snow having a density of 350 kg m^{-3} has a ϵ^* of around 2 ($\epsilon' = \sim 2$, $\epsilon'' = \sim 0.038$). However, the snow volume itself is a heterogeneous medium which is in a constant state of flux due to environmental forcing such as changes in temperature and snowfall. As brine is mobile in the lower reaches of the snowpack, it is normally expressed as a percent volume along with ice and air and can be modeled using temperature relationships (Barber, 1993).

Kinetic grain growth within the basal layer, initiated by warming within the basal layer, cause an increase in crystal size and brine volume through brine wicking into the lower snow volume. The brine-wetted kinetic growth grains within the basal layer of the snowpack create sufficiently large volume scattering to increase the total backscatter above that created by the sea ice surface (Barber et al., 2001). The thermodynamically driven changes within the snowpack are seen in the oscillatory behaviour of the time series trend during winter over FYI (Barber

and Thomas, 1998). Barber and Nghiem (1999) found that the magnitude of the oscillations could be used as a proxy indicator of snow depth and thermodynamic processes acting across the OSA interface.

With the onset of melt, the dielectric properties change considerably. Liquid water at 0°C has a dielectric constant of 80. For wet snow in the pendular regime (water volume < ~7%) both the real part and the imaginary part of the complex dielectric constant seem to be almost independent of the structure of snow (Tiuri *et al.* 1984). During the pendular regime, water held within the interspatial pore space provides ample scattering radii and snow volume scattering rises exponentially. The rapid increase in σ° is largely attributable to marked increases in water in liquid phase, basal layer grain size growth and brine volume as a function of increasing temperature (Barber and Nghiem, 1999). The overall magnitude of σ° is dependent on the ice surface microscale roughness and its surface brine volume (Barber *et al.*, 2001). From melt onset through advanced melt, the surface of the ice is no longer detectable by the sensor as volume scattering within the snowpack dominates σ° (Kirk, 2001).

During the pendular regime the rapid increase in backscatter continues until water by volume within the snowpack approaches 7%. This is a result of both volume scattering due to increased water and brine volume, and surface scattering from the snow surface as water collects in the upper portion of the snowpack. A dip in volume scattering as the snow volume drains in transition from pendular to

funicular snow regimes is also observable from SAR. The resulting dip in σ^0 is characteristic of water draining from the upper portions of the snowpack and brine volume reducing to near zero resulting in a reduction in volume scattering (Yackel and Barber, 2000).

Within the funicular snow regime water becomes continuous throughout the remaining snowpack creating an uneven dielectric interface. This rough interface has a sufficiently large mismatch to produce high backscatter due to surface scattering (Jeffries et al., 1997). During the funicular regime, backscatter will rise to its highest point. The peak in backscatter along the microwave temporal trend signifies the near complete removal of the snowpack and marks the transition to advanced melt with ponding on the surface due to excess water flooding the icescape from the rapid ablation of the snowpack (Drinkwater and Crocker, 1988; Yackel, 2001).

2.4.5.3. Melt Ponds

Melt ponds begin to form during the advanced melting stage of FYI ablation as fresh water from snowmelt begins to pool on the surface. The dielectric permittivity of water at 0.5°C and 5.3GHz is about 65.81. The high dielectric mismatch between the atmosphere and melt ponds creates a specular reflector of incident microwave energy. Under calm conditions melt ponds are characterized by low backscatter as incident energy is reflected away from the sensor (Yackel and Barber, 2000). However, during windy conditions, wave trains oriented

orthogonal to the incident pulse direction cause a dramatic increase in backscatter due to specular reflection back to the sensor (Barber and Yackel, 1999; Jeffries et al., 1997; Comiso and Kwok, 1996). Oscillations and magnitude variations in σ^0 once melt ponds have formed are a function of wind induced surface roughening and/or changes in their fractional coverage (Yackel and Barber, 2000).

Yackel and Barber (2000) found backscatter to pond fraction relationships were poor under light wind conditions ($r^2 = 0.1$) but improved when surfaces became wind roughened (wind speed 3.2 m s^{-1} , $r^2 = 0.47$; 5.3 m s^{-1} , $r^2 = 0.8$). The authors suggest that scattering from ponded surfaces and snow patches would be approximately equal when the surface wind velocity falls within the range of 1.7 m s^{-1} and 2.0 m s^{-1} , explaining the low correlation. As wind speeds increase the backscatter becomes progressively more dominated by ponded surfaces, thereby increasing the difference in σ^0 between pond and snow and allowing for a better estimate of surface ponding. No data was available under calm conditions.

2.5. Conclusions

In this chapter I outlined the major optical and microwave characteristics of melting first year sea ice by describing the thermodynamic processes acting across the OSA interface. My discussion began with an introduction to the formation of FYI and the events, such as atmospheric forcing and timing of snowfall, which dictate its overall structure and depth. However, the focus to my discussion revolved around the physical changes occurring during spring melt which were broken into early melt, melt onset and advanced melt following the nomenclature of Livingston et al. (1987).

During early melt, radiant and atmospheric warming initiates kinetic grain growth through the snowpack resulting in large crystals and an increase in brine volume within the lower reaches of the snowpack. Water begins to form in the interstices of snow grains as the snowpack begins wet snow metamorphism. Both the increase in grain size and addition of water decreases the albedo of the surface due to increased absorption, especially in the near infrared portion of the EM spectrum. Increases in grain size and brine volume cause an increase in microwave backscatter as volume scattering dominates resulting in an exponential increase in σ^0 , as seen in the temporal trend.

The presence of continuous liquid water within the snow volume marks melt onset. During this time, the snowpack goes through two types of snow regimes, pendular and funicular. Pendular and funicular snow regimes are very important to

the physical and electromagnetic properties of the snow cover due to increases of individual grain size, the formation of ice aggregates and the presence of liquid water within the snowpack. The effect of liquid water on snow albedo is simply to increase the effective grain size thus lowering albedo across all wavelengths. There is a distinctive dip in the microwave backscatter temporal trend as the snowpack transitions from the pendular to funicular snow regimes. This transition marks the reduction of brine within the basal layer to near zero, an increase in the water in liquid phase at the snow – ice interface and a reduction of water in the upper portion of the snow layer. During the funicular regime, the snowpack is near isothermal and rapid ablation of the remaining snowpack ensues. This marks the formation of melt ponds and is termed advanced melt.

The removal of the snowpack exposes the bare ice surface as the melt season progresses. The draining of brine from the upper layers of the ice volume produces a surface scattering layer composed of granular decomposing ice. This scattering layer maintains the albedo of unponded ice at a stable level near 0.61, through the remainder of ice ablation. The large grain size of the wet granular ice is an effective volume scatterer of microwave energy and contributes to backscatter based on its fraction extent.

Melt ponds begin to form between sastrugi when the amount of water from ablating snow and ice exceeds the amount able to percolate through the ice volume. Initially the frazil layer of the ice volume is flooded creating a pond bottom

composed of white ice and air bubbles. The white bottom and shallow pond depths is indicative of high pond albedos. The initial frazil pond bottom quickly ablates due to solar loading and mechanical weathering to reveal the darker columnar ice structure below. An increase in albedo allows for more solar radiation absorption which speeds ice ablation from the pond bottom, causing the ponds to deepen. This process is known as the melt pond – albedo feedback mechanism which accounts for the majority of pond deepening after initial surface flooding.

During advanced melt, the fractional coverage of melt ponds and the effect of wind induced wave trains were shown have the greatest effect on microwave backscatter. Oscillations in microwave temporal trends are explained by the contribution of volume scattering by bare ice and spectral reflection from pond surfaces. Wind roughened pond surfaces ($\sim 5\text{m s}^{-1}$) have been shown to dominate backscatter and pond fraction can be determined under these conditions.

Chapter 3 examines surface data collected for exploring the relationship between the physical evolution of the melt surface over FYI and its optical characteristics. A field program was constructed to collect physical and optical measurements as the ice surface progressed from one dominated by wet snow through melt pond drainage.

CHAPTER 3. IN SITU PHYSICAL AND RADIATIVE PROPERTIES OF MELT PONDS

3.1. Introduction

Melt ponds dominate the surface radiation balance of first year sea ice (FYI) during spring and summer ablation, making them a climatologically significant feature of the ocean – sea ice – atmosphere (OSA) interface. Wavelength – integrated and spectral albedo are used to parameterize the radiation balance of the sea icescape and numerous studies have been conducted defining albedo for a wide range of ice types and conditions (e.g. Grenfell and Maykut, 1977; De Abreu et al., 1994; Grenfell et al., 1998; Perovich, 1996; Hanesiak et al. 2001a). These studies have demonstrated that albedo has a strong dependence on the physical condition of the sea ice surface however they lack a time series approach for the evaluation of albedo during the physical evolution of the melt surface. One of the motivations for my thesis research is to provide a detailed examination of the physical characteristics of the first year sea ice surface as the surface albedo evolves from winter to summer. Observations of surface morphology (dimensions and type of melt ponds and snow patches) and albedo were examined to provide a foundation for exploring the link between the physical surface, optical albedo and microwave scattering as outlined in the scientific objectives in chapter 1, namely to:

- “Understand the geophysical processes which drive optical and microwave scattering during the melt season.”

To achieve this objective, a field experiment was conducted over melting snow covered first year sea ice focused on two interconnected spatial scales: point sampling and spatial sampling. Point sampling focused on the connection between the thermodynamic evolution of the system, changes in the physical properties of the surface due to this evolution, and the resulting temporal change in surface albedo. This will form a foundation from which to explore the spatial sampling component of the field program which I will address in Chapter 4.

3.2. Data and Methods

A detailed examination of the evolution of snow-covered smooth landfast FYI to a surface composed of ablating ice and melt ponds was conducted during the Melt Pond Study. This study was part of the Collaborative – Interdisciplinary Cryospheric Experiment (C-ICE) field program located at Truro Island, Nunavut, Canada and it was implemented from June 17, 2002 through July 10, 2002 (figure 3.1). C-ICE is a multi-disciplinary, multi-year field experiment designed to investigate and monitor the effect and variability of physical, climatological and biological forces operating across the OSA interface. As such, the Melt Pond Study was one of several experiments conducted in 2002. The collaborative environment of this field program allowed for a dedicated melt pond program for the observation of the physical and optical evolution of FYI, with the benefit of

complementary data from other coincident field projects such as meteorological and snow physical properties. A detailed description of C-ICE 2002 is available through the Centre for Earth Observation Science at the University of Manitoba (Mundy and Barber, 2002).

The Melt Pond Study Area was established on a portion of homogeneous smooth 'fast' FYI which had not been accessed during previous stages of the field season. A 3km by 3km sampling grid was plotted 4.3km west of the Truro Island Base Camp on Year Day (YD) 165 (see Appendix A for a YD to calendar conversion table) when early melt snow conditions existed (figure 3.2). The sampling grid was divided into 100m by 100m cells. This allowed a sampling grid of 30x30 cells having a surface area comparable to RADARSAT-1 low resolution data products (see chapter 5). Surface sampling sites were selected randomly and stratified by cell, without replacement. A five hour melt pond sampling schedule began with the formation of melt ponds on YD 168. Each five hour period included the time to travel to the study location and complete surface sampling for morphology, optical and wind characteristics. Each sample period was randomly selected based on an interval of no less than two hours and no more than nineteen hours. This schedule ensured that at least one visit to the sampling area was conducted each day (with a maximum of three visits per day). This random temporal schedule enabled the diurnal effect of temperature on melt pond surface properties to be examined. Sampling began at 8am (CST) on YD 168 and continued through YD 189, two days prior to the removal of base camp. Casual

surface observation where recorded on YD 190 and YD 191 while the camp was dismantled.

Two access paths running orthogonal to one another were mapped 1.5km from the south and east borders of the study region, crossing through the centre of the sampling area. The pathways plotted around and through the study region provided snow machine access within a maximum of 750m from the centre of individual sampling sites. Equipment was then pulled from the path by foot. This was done to ensure minimal disruption of the natural surface within the study area (see figure 3.2). Table 3.1 outlines the coordinates of the Base Camp, Meteorological Site and Melt Pond Study Area. Appendix B describes the sampling locations and schedule for individual sampling sites.

Table 3.1. Melt Pond Study Area coordinates for C-ICE 2002. All measures are recorded in decimal degrees.

Position ID	Latitude	Longitude
Base Camp	75.244800	-97.312540
Meteorological Site	75.247241	-97.236516
MP_NW Corner	75.256000	-97.312540
MP_NE Corner	75.256000	-97.416580
MP_SW Corner	75.230000	-97.312540
MP_SE Corner	75.230000	-97.416580
MP_Centre	75.243000	-97.364560

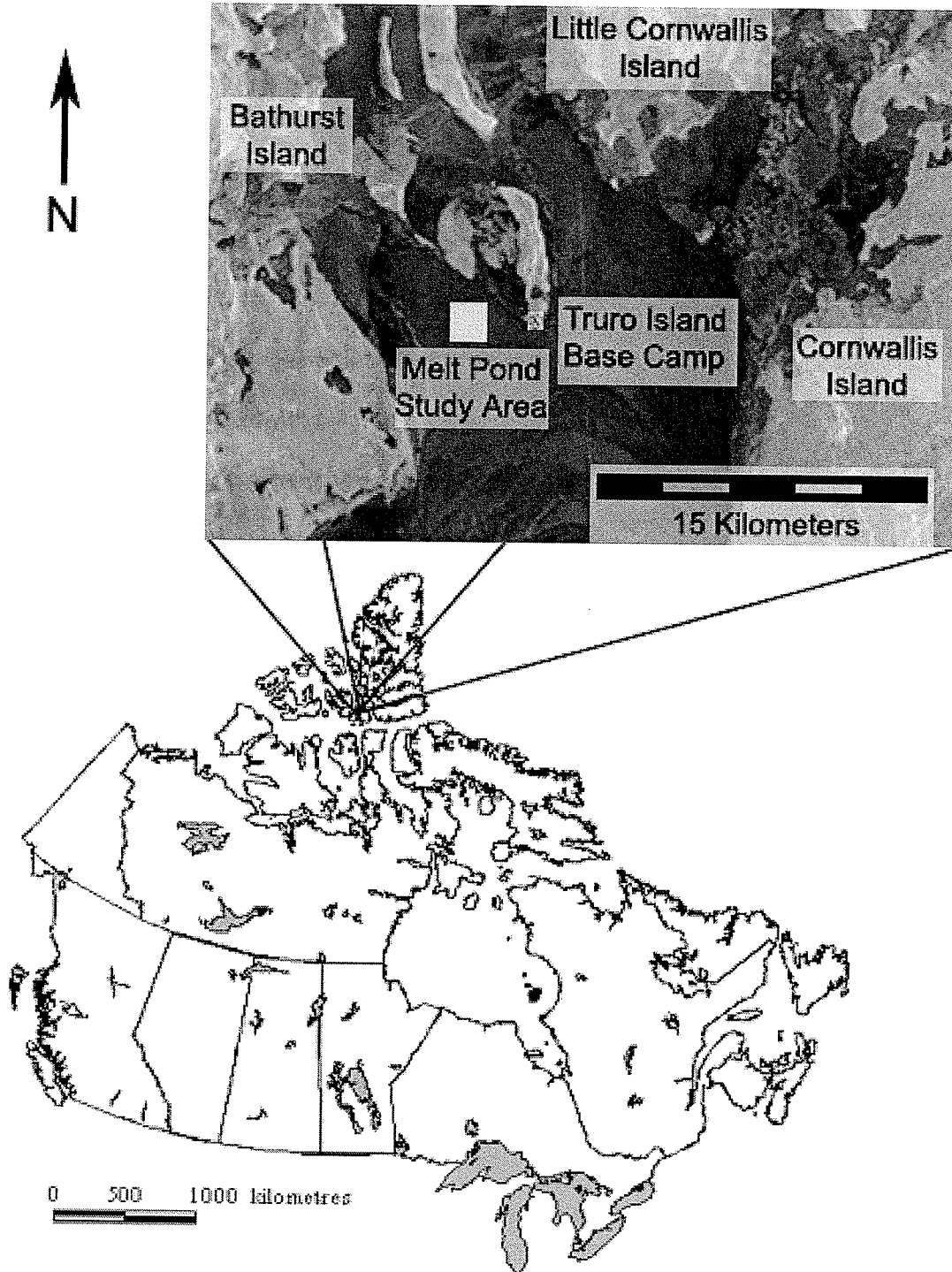


Figure 3.1. The location of the Melt Pond Study Area. The site was located west of Truro Island, Nunavut, Canada on smooth landfast first year sea ice.

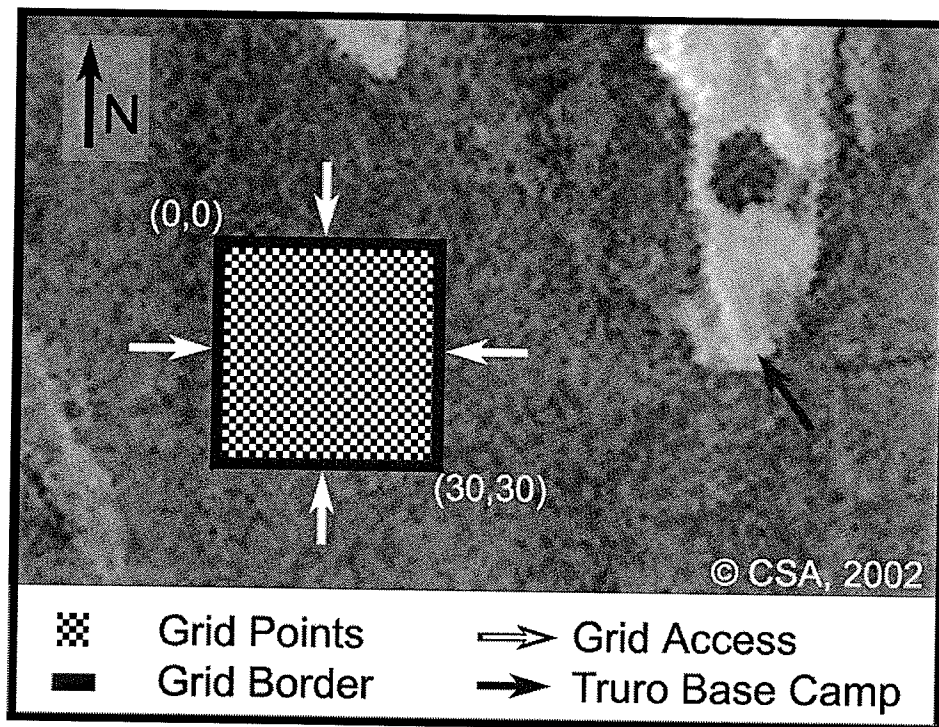


Figure 3.2. The 3km² Melt Pond Study Area was broken into 100m² sampling sites. Two access roads running N-S and E-W intersect through the centre.

3.2.1. Physical Sampling

Snow physical properties were measured and meteorological data collected at a microclimate station (Papakyriakou, 2003) in advance of the start of the Melt Pond Study. This provided a history of the physical and optical state of the surface prior to the start of the melt season. Snow pits were randomly selected within 100m of the microclimate station and snow density, salinity, depth and temperature were collected three times daily from YD 131 through YD 169. Snow density was sampled using a 66.36cm³ density cutter at a 2cm interval. Samples were then weighed to the nearest hundredth of a gram and divided by volume to obtain a density measure. Salinity and temperature were also measured at 2cm

intervals, and at the ice surface, using a conductivity metre and a multi-meter temperature probe. Depth was measured to the nearest 0.5cm using a graduated ruler. These measures were then averaged over the entire snowpack for each day. Albedo measures were obtained from the microclimate station located in close proximity to our study site (Papakyriakou, 2002). Shortwave albedo (400nm – 1100nm) was calculated using the ratio of upwelling and downwelling irradiance recorded by two LiCor pyranometers (model LI200) positioned 1m from the snow surface.

The surface sampling program included an estimation of pond fraction, snow and pond depth profiles, and surface type classification of representative pond and snow patches within the designated sampling site. Each of these variables was used in concert with albedo measurements and aerial photography (Chapter 4) to explore SAR backscatter (Chapter 5). Table 3.2 outlines the measurements recorded.

Table 3.2. Description of physical measurements collected during the Melt Pond Study.

Measurement	Equipment	Accuracy
Pond/Snow Depth	Graduated Ruler	0.5cm
Morphology Profile	Measuring Tape	1.0cm
Surface Classification	Digital Camera	$r^2 = 0.998$
Pond Fraction	Visual estimate	10%
Perimeter Length	Digiroller	0.1m

During the collection of variables at each sample site, observation of the pond to snow ratio was recorded (figure 3.3). Oblique photographs were taken of the site and dominant surface types were recorded and catalogued using digital photography. Also during these sessions wind conditions were monitored in order to estimate the effect of wind roughening on the surface. Wind leads to mechanical weathering of pond boundaries and wind-induced wave trains can amplify backscatter recorded by SAR. My colleague, Randy Scharien, at the University of Calgary will address this aspect of the field season in his Masters Thesis.

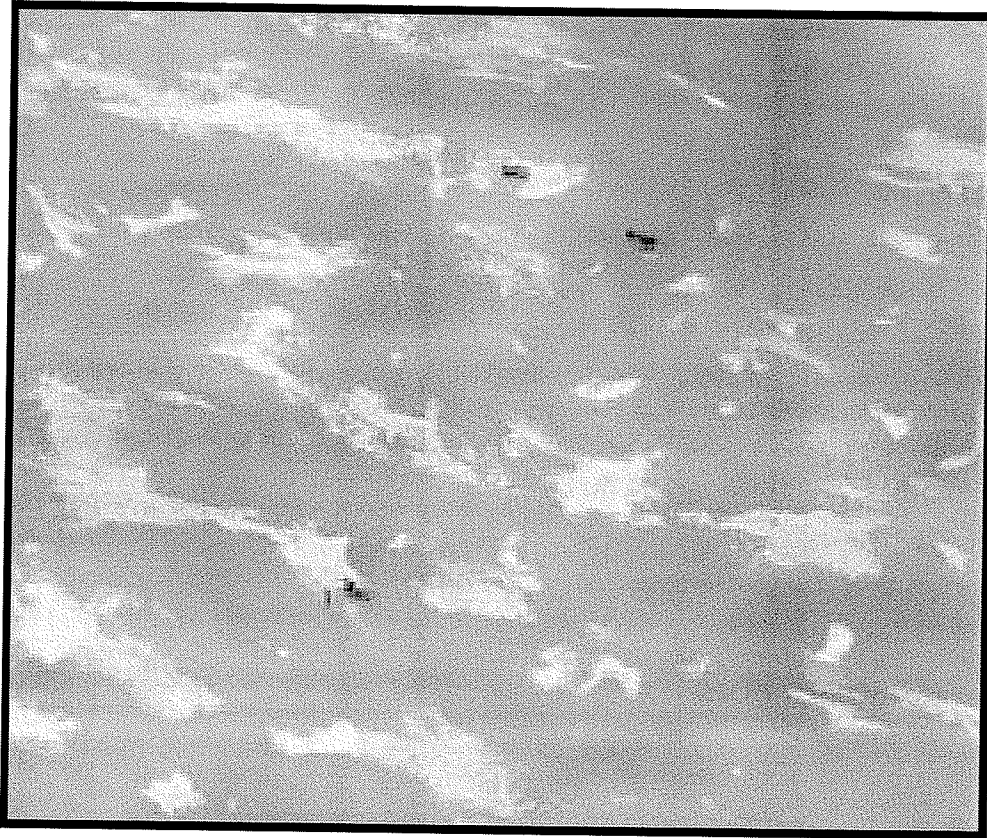


Figure 3.3. An aerial view of the sampling site for YD 175. Snow machines (in the upper portion of the photograph) are 50m from researchers (left of centre on the photograph). Notice that the remaining snow patches are aligned in a linear fashion orthogonal to the predominant wind direction.

3.2.2. Albedo Sampling

Albedo samples were collected at each sampling site. Limiting the grid cells to 100m allowed for the investigation of small-scale variability of surface albedo and associated physical morphology. After identifying the dominant surfaces composing the sampling site, measurements of broadband and spectral albedo were made (figure 3.4). The albedo (α) of a surface at a particular wavelength (λ) is defined (3.1) as:

$$\alpha(\lambda) = \frac{F \uparrow (\lambda)}{F \downarrow (\lambda)} \quad [3.1]$$

Where $F \downarrow (\lambda)$ is the incident spectral irradiance, including direct solar and diffuse contributions, and $F \uparrow (\lambda)$ is the upwelling irradiance scattered by the surface back towards the atmosphere.

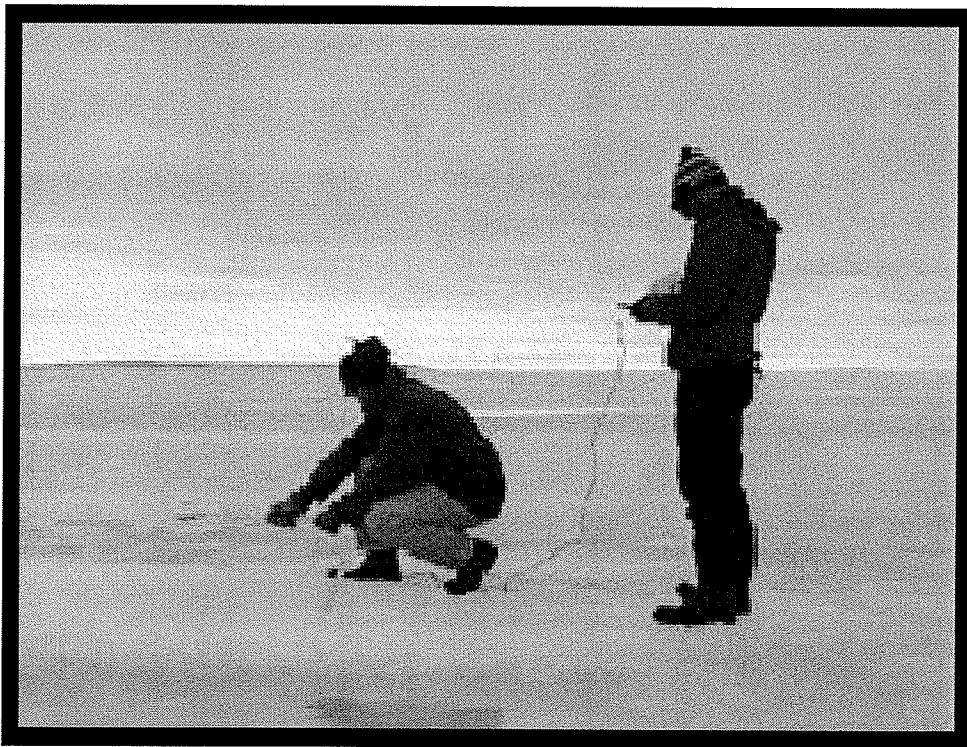


Figure 3.4. A broadband integrated albedo measurement taken over ablating FYI. Notice the high degree of surface flooding and evidence of drainage along the pond edge. (photo by D. Barber)

Broadband albedo was measured using a Middleton pyrano-albedometer, 305nm – 2800nm. The albedometer was factory calibrated and has a 10 second response time. The instrument was held level over dominant surfaces until

measurements stabilized (10 – 30 seconds). Upwelling and downwelling radiance (Wm^{-2}) measurements were then recorded. The dual head of the albedometer gives the instrument increased flexibility for use in the Arctic environment, as only a brief window of stable irradiance is required to take a measurement. During variable cloud conditions, albedometer measurements were taken between breaks in cloud cover or during periods when the solar disc was obscured by a homogeneous cloud layer when upwelling and downwelling irradiance was observed to be stable. This method allowed for observations to be recorded at times of variable cloud, a condition predominant during spring melt. A total of 205 broadband albedo measurements were made over the course of the study period. Broadband (or wavelength-integrated) albedo (α) follows equation 3.2.

$$\alpha = \frac{\int_a^b \alpha(\lambda) F \uparrow (\lambda) d\lambda}{\int_a^b F \downarrow (\lambda) d\lambda} \quad [3.2]$$

Where the limits of integration span the solar spectrum of the instrument ($a = 305nm$, $b = 2800nm$).

Spectral albedo measures were captured throughout the season when appropriate light conditions prevailed. An ASD Fieldspec Pro visible/near-infrared spectroradiometer, 338nm-1100nm with 1.4nm resolution, was used to collect spectral albedo over various melt surface types. A remote cosine receptor having an 180° FOV was used to record both upwelling and downwelling radiance (Wm^{-2}).

Due to the time required to flip the head of the instrument, five samples were taken under uniform sky conditions (either clear skies or uniform cloud cover) to ensure accurate albedo measures. The instrument has a response time of less than a second, allowing a set of 5 measures of incident and reflected scans to be recorded in approximately 15 seconds. In order to ensure consistent measurements of surface albedo recorded by the albedometer and spectroradiometer, markers were placed on characteristic surfaces ensuring that the same surface could be revisited.

ASD data tends to be noisy between 1000nm and 1100nm due to the small portion of energy available to the surface at these wavelengths which results in a high signal to noise ratio. The behaviour of the irradiance between these wavelengths results in high signal to noise ratios and statistically different measures can occur at timescales of less than 1 second. Due to this limitation, the dataset used in this work was limited to wavelengths between 338nm and 950nm.

Verification of uniform irradiance was required of spectral sample sets before measures were converted to albedo. This was done to ensure constant solar irradiance during the sample period (<5 seconds for 5 measures). The Kolmogorov-Smirnov nonparametric goodness-of-fit test (KS test) was applied to sample sets for upwelling and downwelling data before albedo measures were evaluated. The KS test examines if multiple sample groups come from the same distribution. This test is sensitive to differences in the shape of the distribution and

is based on the largest difference between cumulative distributions. Limiting the acceptable albedo samples to those with a 0.05 level of significance for homogeneity reduced the ASD data to 61 of 83 spectral albedo measures for the melt pond season. Integrated spectral albedo segments were then calculated from the ASD data. Values for the integrated wavelength (INT), photosynthetically active radiation (PAR), visible radiation (VIS), blue (BLU) and near-infrared (NIR) segments were computed following equation 3.2. Limits of integration for these segments of the EM spectrum are outlined in table 3.3. The different limits of integration for the spectral data were performed in order to allow for the behaviour of different portions of the EM spectrum to be explored. The albedo dataset includes a physical description of the surface, depth of snow/pond, a digital photograph of the sample and associated integrated broadband and spectral albedo measures.

Table 3.3. Limits of integration (a & b) for spectral albedo over designated wavelengths.

Albedo ID	Start Wavelength (a)	End Wavelength (b)
INT	338nm	950nm
PAR	400nm	700nm
VIS	380nm	740nm
NIR	700nm	950nm
BLU	400nm	500nm

Analysis of photographs capturing varying degrees of bubble density along the bottom of melt ponds was conducted to estimate their influence on albedo. GIS software was employed to estimate bubble density using image histograms. Density slicing of individual image histograms allowed the separation of bubbles

from the ice structure. Bubble density was then calculated based on the ratio of bubble pixels to the resolution of the photo.

3.3. Results and Discussion

3.3.1. Observed Physical and Optical Evolution of an Ablating FYI Surface

The Melt Pond Study began with the formation of surface puddles on YD 168. Bulk snow physical properties collected adjacent to the meteorological station showed the state of the snowpack prior to melt pond formation (figure 3.5 and figure 3.6). Snowpack data confirmed that pond formation began shortly after rapid ablation of the snow volume. It also illustrated that as the snow volume reached zero degrees, salinity was flushed from the ice surface. This process was associated with the transition from the pendular to funicular snow regimes (Barber et al., 2001). As the pond season began, the surface was composed of rapidly ablating snow with small puddles overlying white frazil ice and a surface albedo approaching 0.6.

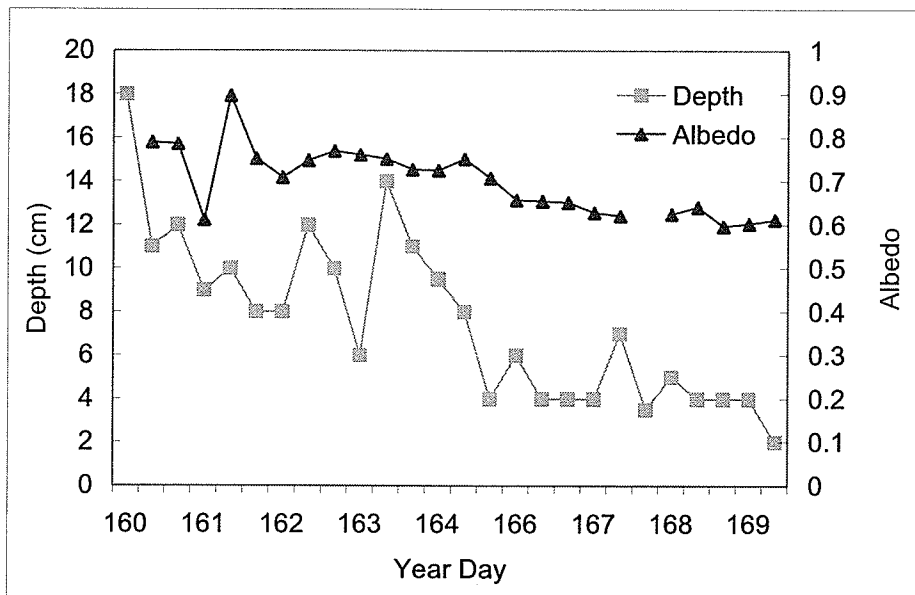


Figure 3.5. Snow depth and integrated broadband albedo (305nm – 2800nm) of FYI surface prior to the start of the Melt Pond Study. Data observations were recorded at the C-ICE Meteorological Station.

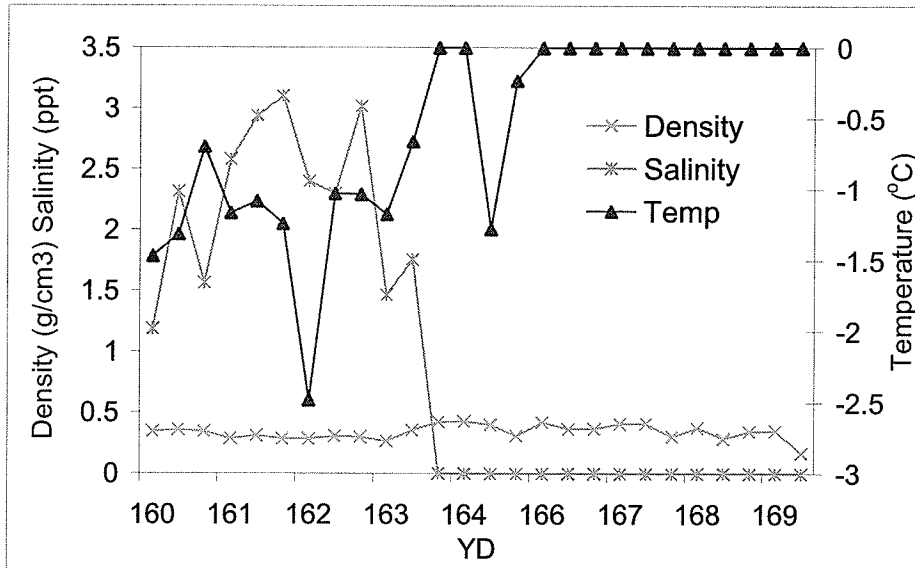


Figure 3.6. Density, salinity and temperature of the snowpack prior to the start of the Melt Pond Study. Values represent the average from observations made using a 2cm interval through the snowpack. Observations were recorded in close proximity to the meteorological station.

Pond formation and expansion continued rapidly over the first three days of pond formation. Visual observations of pond fraction for YD 168 estimated <1% coverage. This estimate grew to 5% on 169, 25% on the morning of 170 and 65% by the evening of that day. Cold temperatures on YD 171 reduced pond estimates to 60% followed by a surge towards maximum coverage between YD 174 and 177 with the pond fraction approaching 85%. Between YD 174 and 184 fractions remained high, ranging between 50% and 80% though pond fractions as low as 10% were noted in study sites containing drainage points. Differences in pond fraction for point estimates were attributed to the proximity of drainage points. A comparison of aerial photographs captured in situ to surface observations showed visual pond fractions estimates to fall within $\pm 10\%$.

YD 184 and 185 saw rapid drainage of the surface. The rapid drainage indicated that the ice volume had become isothermal. As the ice volume became isothermal the brine channels were activated which increased the percolation rate through the volume which facilitated surface water drainage (Eicken et al., 2002). Surface drainage continued until a dry surface (devoid of surface ponds) was observed on YD 190, corresponding to a near complete removal of ponded surfaces. Figure 3.7 shows the estimated pond fraction through the melt season while figure 3.8 illustrates how the surface changed over the course of the melt season.

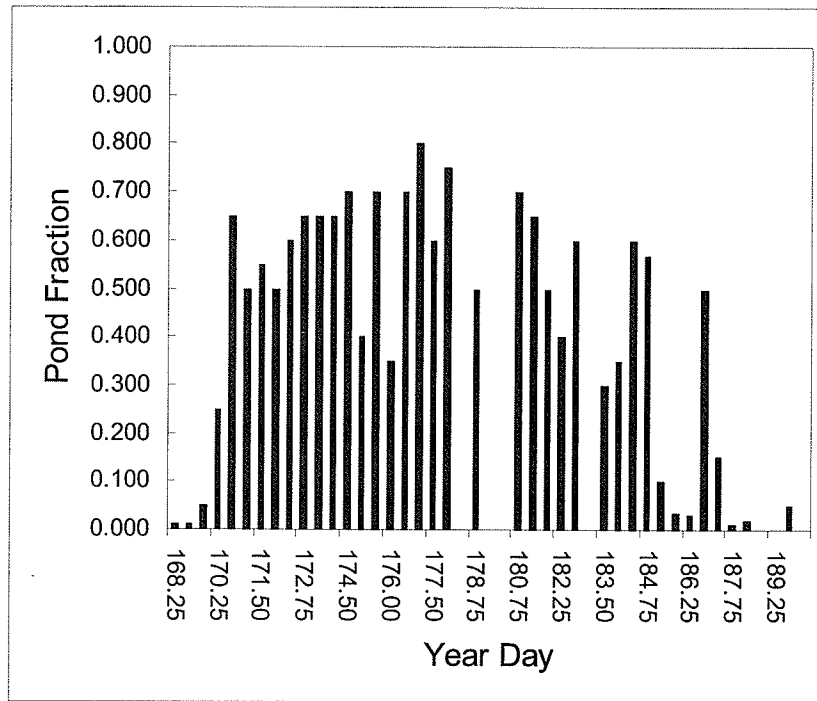


Figure 3.7. Pond fraction estimates observed for individual sampling sites over the course of the melt season. Year day fractions correspond to the time of day pond estimates were taken (.25 = morning, .5 = afternoon, .75 = night).

As the FYI surface transitioned between snow, bare ice and melt ponds, several different distinct physical and optical surfaces were observed and recorded. These surfaces were used to answer the first research question proposed for this chapter.

- 1) What is the relationship between the geophysical properties of melting snow covered smooth FYI and surface albedo?

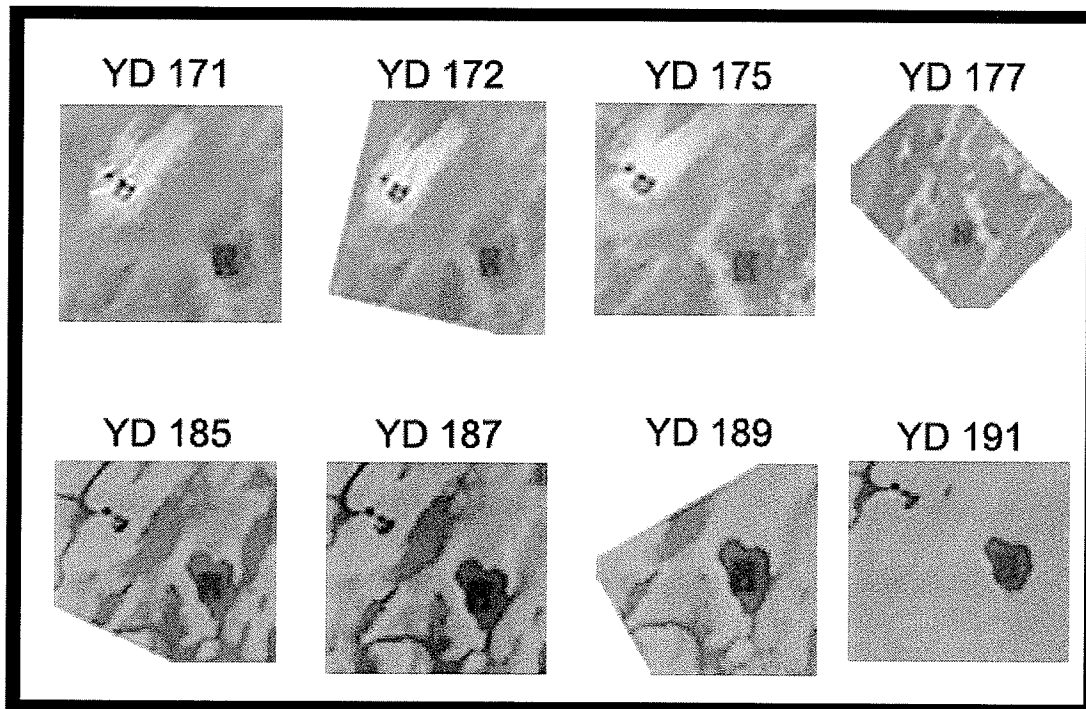


Figure 3.8. Time series aerial photographs taken by the powered paraglider. The images show the change in surface characteristics over the melt season. Note the seal hole (upper left) which provided the area with drainage and resulted in lower levels of ponding once drainage began. The dark rectangle is one of three tarpaulins (4m x 5m) deployed within the study area.

Table 3.4 outlines the physically and optically different surfaces encountered during the melt season. Table 3.5 describes the average surface depth and spectral albedo for six intervals within the solar spectrum. Each of these surfaces was then placed into one of three surface categories; unponded, transitional and ponded. First, unponded surface types included areas of the icescape which were free of the influence of ponded water. In contrast, areas flooded by melt water were categorized as ponded surfaces. Finally, transitional surfaces were found between ponded and unponded surfaces and their influence on the surface structure was controlled by fluctuations in the extent of the ponded surfaces. The

remainder of this section will consider the surfaces observed within each of these categories, focusing on the evolution of both the physical and optical state of the ablating FYI icescape.

Table 3.4. Representative melt surfaces documented during the 2002 Melt Pond Study. Each surface type is associated with a time interval corresponding to the evolving physical and optical surface.

Surface ID	Code ID	Year Day Observed
Shallow saturated snow	SS	168 – 171
Deep saturated snow	DS	168 – 171
New deteriorated ice (shallow)	NI	171 – 191
Old/mature deteriorated ice (deep)	OI	172 – 191
New snow over deteriorated ice	NS	173, 183, 186, 190
Transitional pond edge surface	TR	168 – 191
Transitional surface w/ blue background	TR_B	180 – 191
Blue ice (recently drained)	BI	183 – 186
Slush	SL	182, 185, 189, 190
Seal hole	SH	168 – 191
Deep Pond	DP	172 – 191
Medium Pond	MP	174 – 191
Shallow Pond	SP	174 – 191
Deep pond with low bubble density	DP_LB	169 – 172, 187
Moderate depth pond with medium bubble density	MP_MB	169 – 173, 187
Shallow pond with high bubble density	SP_HB	168 – 177, 187 – 189

Table 3.5. Three representative surface categories (unponded, transitional and ponded surfaces) with corresponding surface types for an ablating FYI volume. Each surface type is associated with a depth and various integrated albedo segments averaged from samples collected throughout the field season. Standard deviation is given for broadband albedo measures (Std. Dev.).

Surface ID	Depth (cm)	305 – 2800nm (BRD)	BRD Std. Dev.	338 – 950nm (INT)	400 – 700nm (VIS)	380 – 740nm (PAR)	700 – 950nm (NIR)	400 – 500nm (BLU)
Unponded Surfaces								
SS	3.8	0.6179	0.036	0.6187	0.6497	0.6554	0.5390	0.6739
DS	7.83	0.7068	0.012	0.7353	0.7612	0.7646	0.6728	0.7710
NI	1.5	0.5378	0.042	0.5263	0.5743	0.5668	0.4514	0.6043
OI	3.29	0.6789	0.021	0.6424	0.6882	0.6737	0.5895	0.6909
NS	2.42	0.7584	0.050	0.7691	0.8075	0.8036	0.7151	0.8150
Transitional Surfaces								
TR	1.37	0.4017	0.062	0.4697	0.5062	0.5148	0.3664	0.5502
TR_B	2.75	0.3113	0.029	0.4007	0.4380	0.4474	0.2924	0.4859
BI	0.25	0.2445	0.043	0.2466	0.3197	0.3049	0.1303	0.3788
SL	1.91	0.2212	0.039	0.1984	0.2465	0.2604	0.0521	0.3208
Ponded Surfaces								
SH	1000	0.07	n/a	0.0729	0.0743	0.0743	0.0608	0.0891
DP	10	0.1961	0.019	0.1872	0.2318	0.2448	0.0524	0.3033
MP	4.92	0.2265	0.016	0.1950	0.2446	0.2593	0.0481	0.3265
SP	1.58	0.2234	0.012	0.2007	0.2449	0.2576	0.0653	0.3159
DP_LB	8.09	0.2662	0.032	0.3191	0.3848	0.4013	0.1250	0.4788
MP_MB	4.36	0.3276	0.027	0.3192	0.3841	0.4001	0.1283	0.4729
SP_HB	1.71	0.3385	0.030	0.3728	0.4299	0.4440	0.2111	0.4998

3.3.1.1. The Unponded Surface Category

The field season began with a FYI icescape dominated by a rapidly melting snowpack. As the snowpack ablated, due to a strong positive longwave flux from atmospheric warming and increased insolation, it was replaced by melt ponds and

a deteriorating FYI volume. The unponded surface category was composed of saturated snow and bare deteriorated ice. The albedo of the saturated snow and bare ice was reasonably uniform and differences in magnitude were a function of depth, snow grain size and water content (i.e., water in liquid phase held within the lower portion of the snow/bare ice volume). Figure 3.9 illustrates differences in the averaged spectral albedo of various unponded surfaces observed through the melt season.

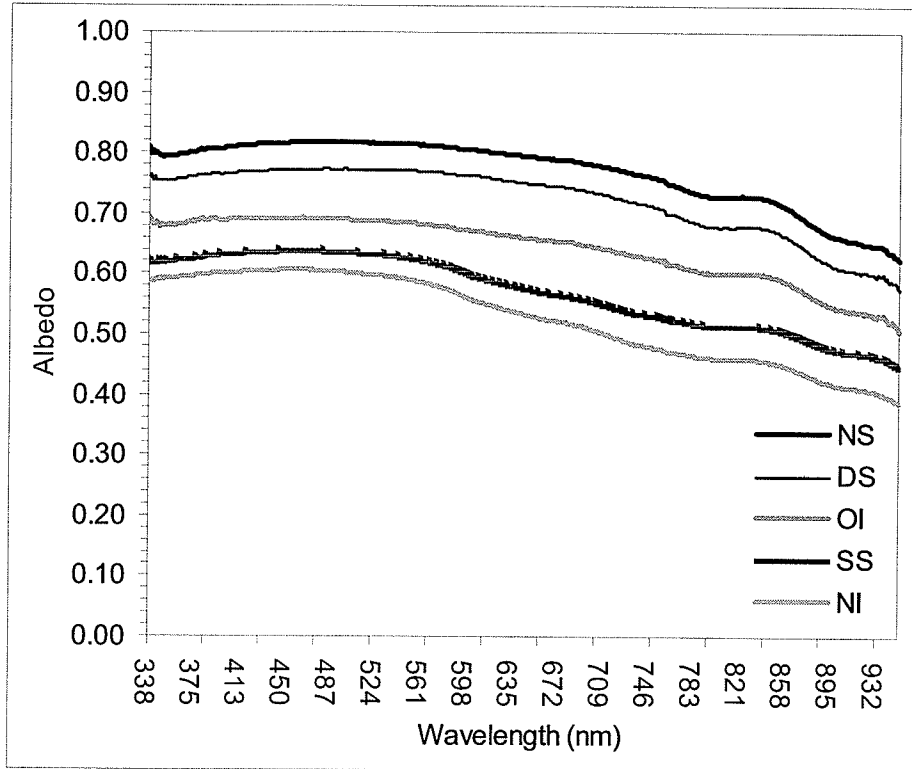


Figure 3.9. Averaged integrated albedo for snow and bare ice types observed through the melt season. New Snow (NS), Deep Saturated snow (DS), Saturated Snow (SS), New deteriorated Ice (NI) and Old deteriorated Ice (OI).

Saturated snow dominated the surface until its ablation on YD 172. Deep saturated (DS) and shallow saturated (SS) snow have a lower albedo than that of dry snow. This lower albedo was caused by large rounded snow grains created by equitemperature snow metamorphosis and was typical of the funicular snow regime. Also, the base of this snowpack was saturated in melt water, increasing absorption across all wavelengths as snow depths decreased, especially beyond 800nm, which acted to further reduce albedo.

A combination of warm weather and sunny skies caused the complete ablation of the snowpack between YD 171 and YD 172. The removal of the snowpack revealed a well developed layer of deteriorated FYI described in Chapter 2 as the "surface scattering layer". The remaining bare ice patches were narrow and elongated and observed to follow a cyclical pattern corresponding to the pattern of sastrugi, a remnant of winter snow distribution. The snow distribution pattern was observable from aerial photography and will be described in greater detail in Chapter 4.

Old deteriorated ice (OI) was a well developed surface scattering layer, establishing itself in the centre of bare ice patches and radiating out toward melt ponds. Old deteriorated ice was well drained, having a depth greater than 4cm, and a stable albedo near 0.65. The depth of OI was controlled by a balance in the rates of surface ablation due to the surface heat fluxes and the rate of internal melting due to the absorption of shortwave radiation (Grenfell and Perovich, 2004).

OI was composed of large ice agglomerates which allowed for continuous drainage of melt water from the surface. The albedo of old deteriorated ice was mainly a function of the absorption of solar energy by large ice agglomerates. OI became a ubiquitous feature of the icescape after YD 171.

New deteriorated ice (NI) was introduced once drainage channels became established and pond fraction began to recede. As ponds decrease in size due to pond deepening and a reduction of melt water on the surface, NI began to form as previously ponded areas became exposed and the columnar structure of the ice volume began to deteriorate. The shallow depths (1cm – 2cm) allowed for some of the optical properties of the underlying columnar structure to influence the albedo while water draining from both the OI and NI structure further decreased albedo. NI was first observed on YD 171 as transitional surfaces continue to deteriorate following the recession of melt pond extent.

During this time, solid precipitation will enhance albedo across all wavelengths. Snowfall resulted in only small accumulations with the majority of the snow melting shortly after deposition. However, even 1cm of snowfall can dramatically increase the albedo of unponded surfaces (Warren, 1982). New snow was found to have an albedo 16% higher than mature deteriorated ice and 24% higher than newly formed deteriorated ice. Snowfall accumulations were observed on YD 173, 182, 185 and 189/190.

3.3.1.2. The Transitional Surface Category

A ubiquitous “transitional” ring separated ponds from snow and/or ablating ice patches throughout the field season. This ring was represented by the transitional surface category and contains surface types that act as a buffer region between the unponded, and ponded surface categories. There were three distinct transitional surfaces based on their individual optical characteristics. These surfaces were characterized by a maximum in the 400nm – 500nm region with a decrease in the 500nm – 800nm region due to increased absorption by a moist surface in the longer wavelengths. Broadband albedo values for transitional surfaces ranged from 0.24 to 0.40. The level of influence for transitional surfaces varied from a few centimetres during pond advance to more than a metre during times of drainage. Figure 3.10 shows the averaged optical behaviour of observed transitional surfaces.

The first transitional surface (TR) was the most commonly observed and was present throughout the field season. TR was composed of large granular ice agglomerates saturated with melt water. During the early portion of the season, TR was a remnant of frazil ice, separating melting funicular snow from newly formed ponds. As the melt season progresses TR was observed as actively deteriorating bare ice along the fringe of melt ponds. TR has an average depth of 1.37cm.

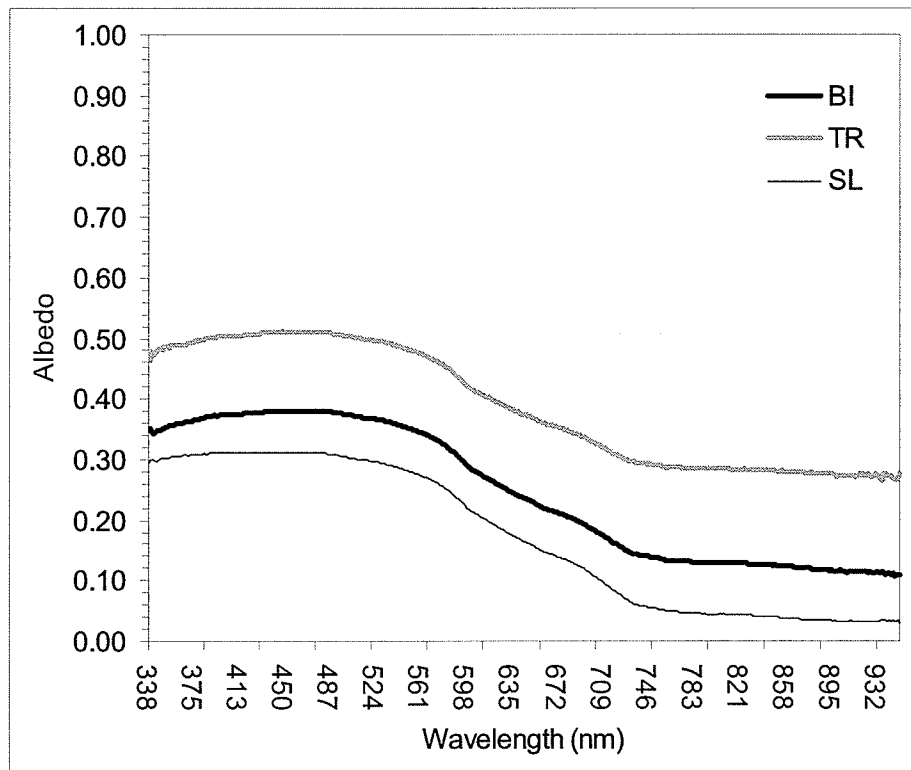


Figure 3.10. Averaged integrated albedo for the transitional surface category. Blue Ice (BI), Transitional pond/snow interface (TR) and Slush (SL).

Transitional blue (TR_B) was observed after periods of pond drainage. TR_B was described as 30% to 50% white speckle on a blue background and was consistent with the first stage of bare ice deterioration once the columnar FYI structure became exposed. This surface type consisted of granular ice agglomerates and/or hoar frost overlying a blue ice surface with an average depth of 2.75cm. The spectral albedo of TR_B was slightly lower than TR. TR_B was most often observed during morning sampling and was associated with the presence of hoar frost overlying the ice surface which formed in vertical strips above the ice surface. Depth measurements for TR_B were made to the top of

these vertical strips, thus amplifying the TR_B depth measurement over that of the more developed TR surface. TR_B was first observed on YD 180 and continued throughout the rest of the field season.

Blue ice (BI) was only seen during times of rapid pond drainage and is described as the exposed columnar ice surface of drained pond bottoms before the ice structure begins to deteriorate. The columnar ice gives this surface a sky blue colour with a smooth surface. At this stage, the pore space between ice crystals was filled with water thus increasing absorption in the longer wavelengths while transmission of shortwave lengths promoted scattering within the ice volume. However, within hours of the surface becoming exposed, water drainage from the upper portion of the ice volume caused the columnar structure of the ice to break down forming TR_B. Most blue ice was observed on YD 184 and 185, when rapid drainage of the surface occurred.

Finally slush (SL) has been grouped with the transitional surfaces however it is a pond surface which only occurs after snowfall events. Slush was present in areas of shallow water that became filled with snowfall to create an optically blue surface with high, near infrared absorption. High water content kept the albedo low in the longer wavelengths due to increased absorption while maximum reflection was observed in the 400nm – 500nm region. The presence of slush was short lived as it rapidly melted into the pond water. Slush was observed after snowfall events on YD 182, YD 185, YD 189 and YD 190.

3.3.1.3. The Poned Surface Category

Melt ponds occur on sea ice when rates of ablation exceed rates of drainage resulting in a pooling of water on the ice surface. Changes in the density of bubbles found in ablating frazil ice at the bottom of ponds played the largest role on the evolution of the pond optical characteristics. Initial ponds formed over frazil ice that contained a high volume of air trapped within its crystal lattice. As ponds matured, the frazil layer ablated and mature ponds exhibited scattering within the ice volume for shorter wavelengths (300nm – 550nm) and absorption within the water volume for longer wavelengths (>550nm). Figure 3.11 illustrates changes in albedo as melt ponds mature.

Of particular interest was the nature of pond albedo curves between 550nm and 750nm where an increase in absorption within the water volume resulted in a precipitous decrease in albedo. The effect of scattering between 750nm and 820nm, caused by bubbles, resulted in a stable albedo with a near linear decrease beyond 820nm. The difference in albedo between ponds with bubbles to those without suggested that the albedo between 750nm and 820nm was a function of absorption within both the ice and water volume. A combination of frequency of bubbles trapped within the frazil layer of newly formed ponds, and depth of water as ponds deepen, resulted in an 18% decrease in albedo within this range of wavelengths.

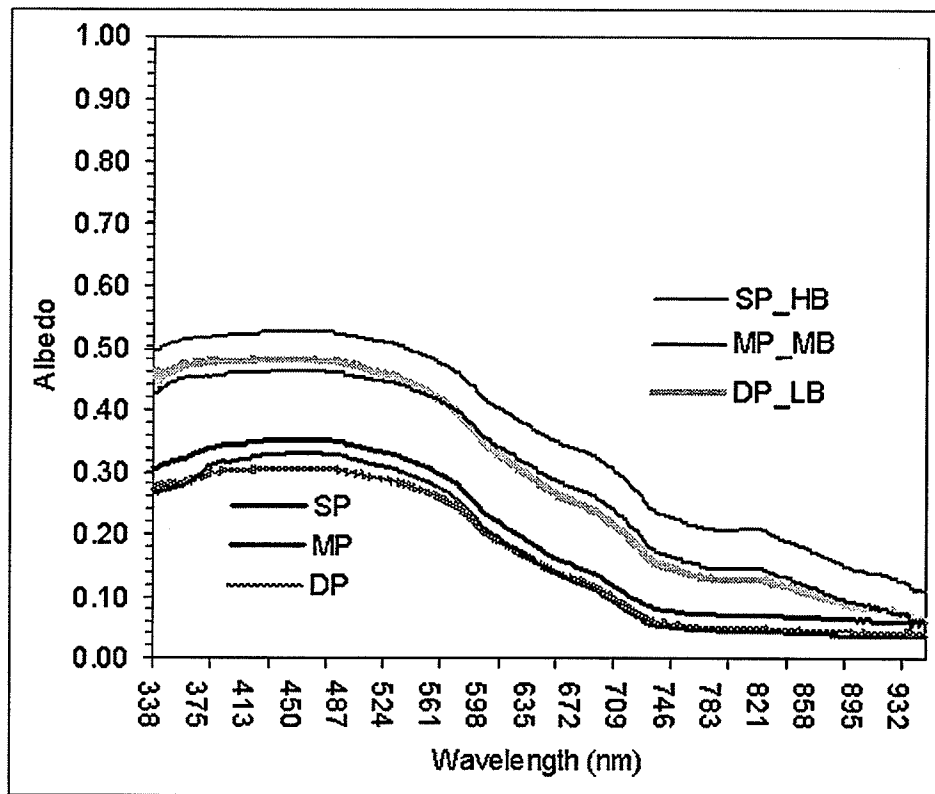


Figure 3.11. Averaged spectral albedo for melt ponds at different stages and depth. Deep Pond (DP), Moderate Pond (MP), Shallow Pond (SP), Deep Pond Low Bubble Density (DP_LB), Moderate Pond Moderate Bubble Density (MP_MB) and Shallow Pond High Bubble Density (SP_HB).

A rough interface at the water – ice interface, most likely a remnant of frazil ice ablation, explains the high albedo between 400nm and 500nm of shallow melt ponds (SP). The rough interface increased scattering in the blue – green portion of the EM spectrum and shallow melt ponds appeared aqua in colour. The average SP depth was 1.58cm. Differences between the albedo of medium (MP) and deep (DP) melt ponds was negligible despite an increase in average depth of 5.08cm from medium (4.92cm) to deep (10cm) ponds. This finding suggests that the ice volume remained optically thick (>0.5m) throughout the melt season.

Figure 3.12 demonstrates the transition of pond optical characteristics as bubbles are released. Picture ID in table 3.6 corresponds to figure 3.12 and illustrates the effect on albedo of bubbles held within the frazil layer of FYI as ponds begin to form over the surface. A correlation of 0.712 between bubble fraction and albedo suggests a relationship between these two variables. One possible explanation for the observed correlation is water depth. Albedo will decrease with increased depth due to attenuation of shortwave energy within the water volume, especially in wavelengths beyond 550nm. Due to limited data for the effect of bubbles on pond albedo (15 samples), the effect of depth was not taken into consideration.

The primary mechanism for bubble release was the ablation of the frazil layer due to shortwave absorption by the pond water and underlying ice. The second mechanism for bubble release was mechanical weathering due to wind. As wind induced wave trains come in contact with frazil ice, ice aggregates were broken and bubbles were released. Although not directly measured, a decrease in bubble densities was observed after wind events. Pond edge advance was also noted during times of high wind due to edge erosion corresponding to leeward pond advance.

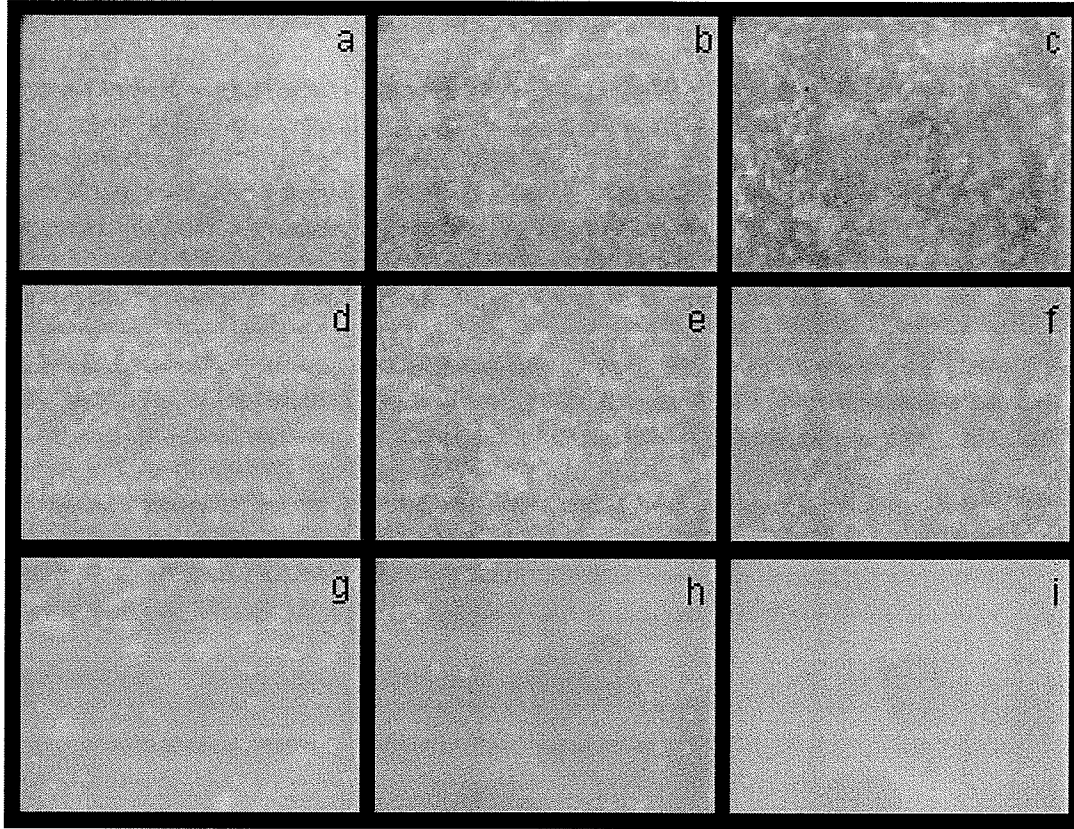


Figure 3.12. The evolution of melt ponds through the melt season. Bubble densities quickly reduced after initial ponding however a ring of high bubble density is found along pond fringes during times of advance. Picture ID correspond to table 3.6. Each image is roughly 30cm x 23cm.

Table 3.6. Evolution of pond bubble fraction and albedo during the early stages of pond formation. Bubble fraction estimates were made from the separation of bubbles from the photograph background using image histograms.

Picture ID	Sample ID	Albedo	Depth (cm)	Bubble Fraction
a	171b_03	0.413523	1	0.905
b	173b_05	0.310576	5.5	0.735
c	173b_04	0.29425	3.5	0.529
d	172a_5.31	0.289606	4	0.1948
e	172a_4.32	0.339534	3	0.1765
f	172a_8.28	0.317049	3	0.1488
g	172a_7.29	0.2859	4	0.1305
h	172a_05	0.280306	4	0.0658
i	183b_07	0.217092	5.5	0

As melt ponds expanded and matured the frazil layer ablated releasing bubbles and exposing the darker columnar ice below. This transition began immediately after pond formation, starting in the deeper parts of ponds and advancing towards the edge. However, complete removal of pond bubbles was not seen until after the maximum pond extent was reached. This was the result of a ring of high bubble density which formed through pond expansion as melt water advanced into the remaining bare ice patches. During the 2002 season, bubbles were released from the deeper sections of ponds beginning on YD 171 but complete removal of bubbles from pond bottoms was not observed until YD 180, three days after maximum pond advance was recorded. The release of bubbles reduced optical scattering at the pond – ice interface causing an increase in shortwave transmission into the ice volume and a corresponding reduction in albedo (figure 3.13).

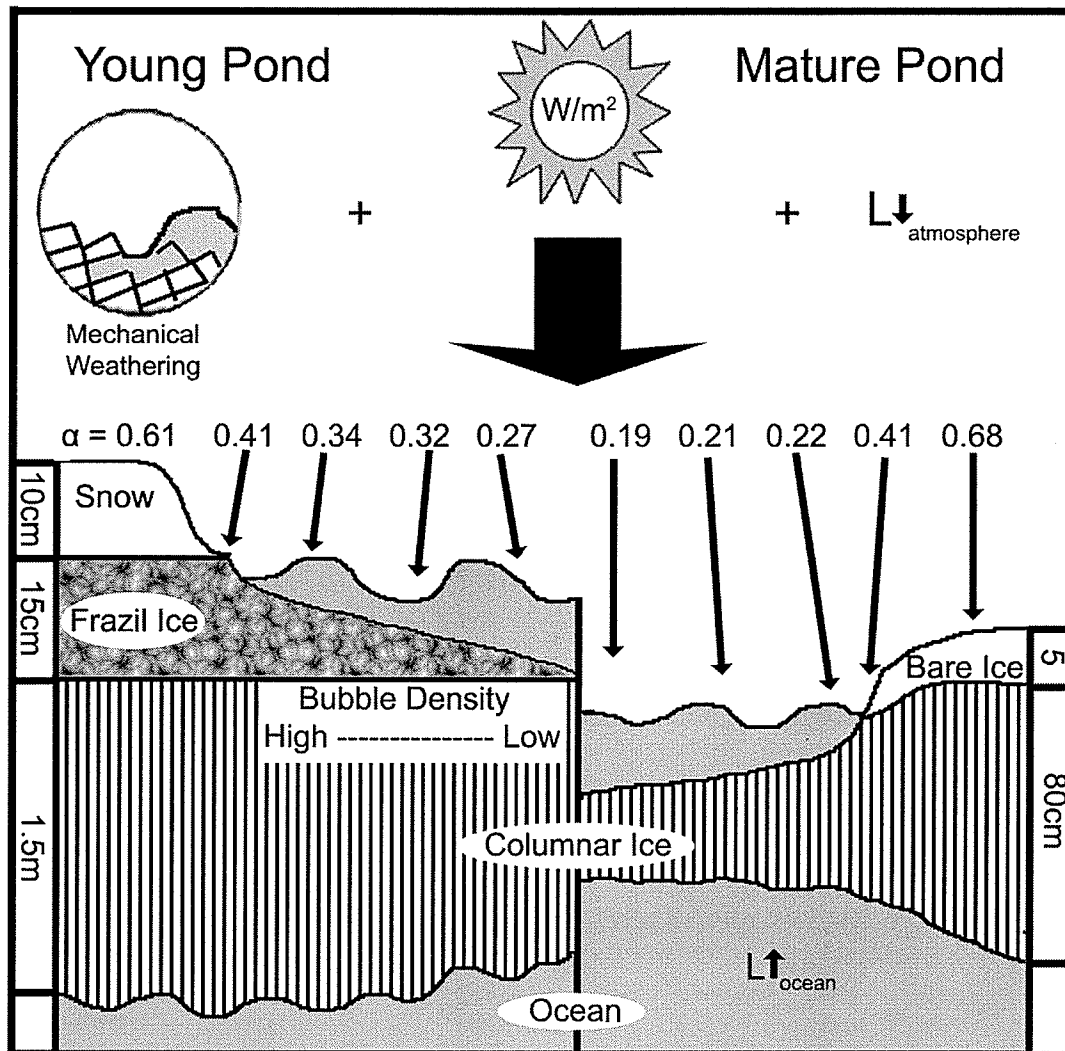


Figure 3.13. Processes leading to melt pond maturity over FYI. The melt pond – albedo feedback is initiated by an increase in the atmospheric heat flux (L), stimulating snow ablation and the development of melt ponds. During initial pond formation the albedo of young ponds is dictated by pond depth and the scattering properties of the frazil ice layer. Ablation of the frazil layer is a function of the wind induced mechanical weathering, and solar insolation (Wm^{-2}). As the melt ponds matured, the albedo is dictated by pond depth and the optical properties of the columnar ice volume.

The average pond depth observed during the melt season was considerably shallower than depths reported by other researchers (e.g. DeAbreu et al., 1994;

Hanesiak et al., 2001b; Grenfell and Perovich, 2004). Pond depths increased to a maximum depth of just over 10cm with the majority of ponds averaging just 5cm deep. Several factors combine to explain this observation. First, the ice surface was noted to be nearly homogenous with very few cracks or seal holes to act as drainage points. This resulted in a high degree of surface flooding before drainage channels became established and stabilized the surface. Secondly, long periods of fog and cloudy weather limited downwelling shortwave radiation while increasing the longwave flux. The reduction in shortwave flux at the surface slowed pond bottom ablation, forcing excess water to flood across the smooth surface. The increase in longwave flux accelerated the melt rate of snow and bare ice, increasing the flux of water to the surface. Finally, considerable amounts of precipitation accumulated on the surface, mostly in the form of rain, further increasing the amount of water on the surface (figure 3.14).

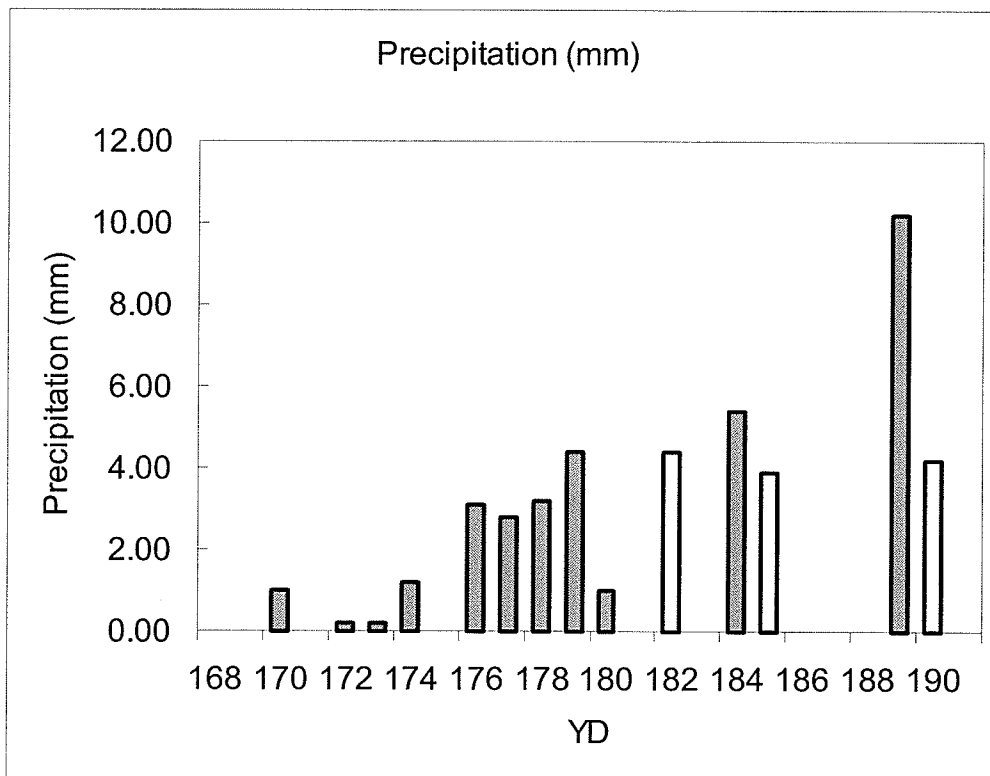


Figure 3.14. Liquid precipitation captured using a rain gauge and recorded during the melt pond field season. Shaded areas represent liquid precipitation and white areas represent solid precipitation. Precipitation for YD189 was a combination of both rain and snow. Most snow occurred in the latter portion of the melt season leading to an increase in overall surface albedo due to the formation of slush in melt ponds and increased optical scattering on ablating ice surfaces.

3.4. Conclusions

In this chapter, an exploration of the surface morphology of an ablating first year sea surface was conducted using in situ point sampling of physical and optical surface measurements. Over the course of the melt pond season, 16 individual surface types were observed. Each surface type was identified using a combination of physical and albedo characteristics. The surface types were then placed within one of three surface categories: ponded, unponded and transitional surfaces.

The albedo of the unponded surface was dependent on the state of the snowpack, the presence of transitional surfaces and, the extent of the bare ice surface scattering layer. As the ponds began to form the snowpack was isothermal and rapidly ablating. Snowpack albedo was reduced from 0.6 to 0.52 due to equitemperature grain growth, water saturation and the exposure of frazil ice. The removal of the snowpack resulted in the development of the surface scattering layer. This layer was shown to progress from blue ice to a deep, mature scattering layer having a progressive increase in albedo from 0.24 to 0.65. Unponded areas were observed to orient orthogonal to the predominant wind direction, with the deepest patches following the pattern of snow distribution.

Two factors were shown to influence melt pond albedo. First, the presence of frazil ice on the bottom of newly formed melt ponds was determined to have the greatest influence on albedo across all wavelengths. Early ponds formed over

flooded frazil ice containing a high fraction of air bubbles. Pond albedo decreased from 0.33 to 0.19 through the melt season with the greatest decrease in albedo occurring after frazil ice air bubbles were released. A correlation factor of 0.7 between bubble fraction and pond albedo was established however a more detailed study is needed.

In the following chapter, the use of point sample statistics will be assigned to aerial photography and up-scaled to the spatial level. This will facilitate the exploration of the temporal evolution of the physical and optical icescape as it progresses through the melt pond season.

CHAPTER 4. THE SPATIAL DISTRIBUTION OF THE PHYSICAL AND RADIATIVE PROPERTIES OF MELT PONDS

4.1. Introduction

As was observed in Chapter 3, during the ablation period over smooth first year sea ice (FYI) the surface was in a constant state of flux as it evolved from a volume covered by ablating snow to an icescape flooded with melt water which eventually drained. In order to explain this evolution I introduced 3 surface categories containing 16 distinct surface types based on their physical and optical properties. The motivation of this chapter is to assign the individual surface types to aerial photography in order to examine the icescape at the regional scale. This will allow me to investigate the role of the evolving surface morphology on the development of melt ponds of various depths and dimension and the associated development of bare ice patches, on the physical structure and surface albedo of this complex mosaic. Further, surface statistics derived from aerial photography will provide a foundation for the comparison of the physical, optical and microwave characteristics of the melt surface as described in the second scientific objective of this thesis, namely to:

- *“Construct a link between microwave and optical scattering based on the physical characteristics of the melt surface.”*

This objective will be met following two interrelated investigations set at different spatial scales. First the exploration of the physical and optical relationship will be investigated using point measures from individual frames of the aerial photography dataset. This will be followed by an investigation on the relationship between the physical and optical characteristics of the icescape at the regional scale.

4.2. Data and Methods

4.2.1. Aerial Photography

Aerial photographs of the surface were catalogued along a flight path beginning at the meteorological station and continuing through the 3km by 3km study area. Flights were conducted on 14 occasions through the melt season. A powered paraglider was piloted from Truro Island Base Camp using the meteorological station and three orange tarpaulins set within the Melt Pond Study Area to aid navigation and to provide scale in the digital aerial photography (figure 4.1). The main objective of the paraglider program was to digitally capture surface characteristics at local scales over the meteorological station and the Melt Pond Study Area as the spring season progressed from dry snow to full melt pond coverage (figure 4.2). These data were then reduced to provide information on surface morphology of both melt ponds and snow patches throughout the spring season.

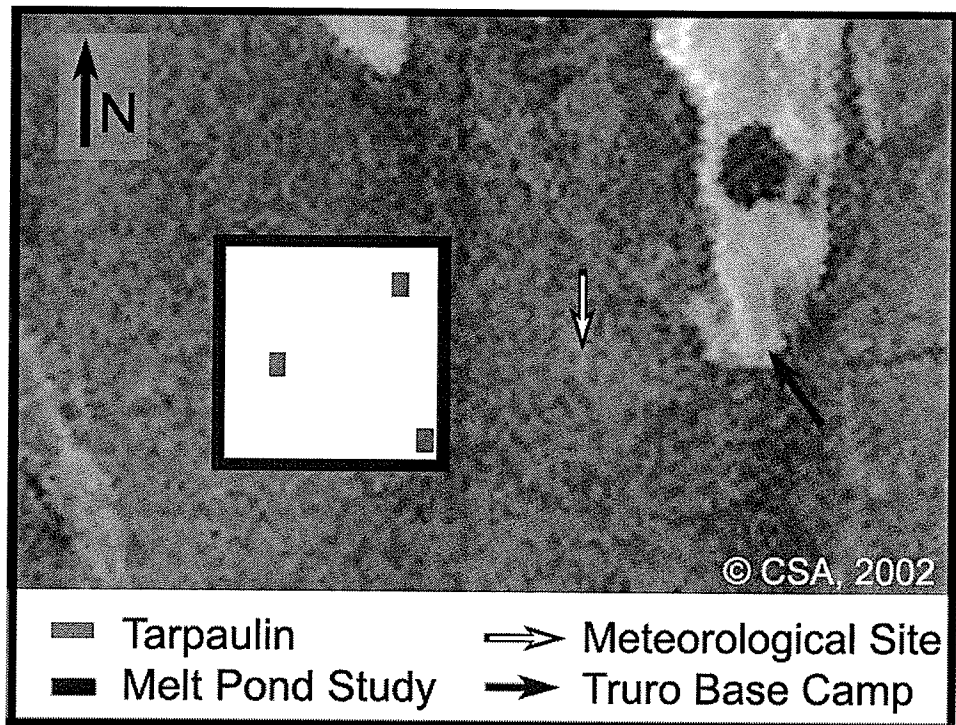


Figure 4.1. Locations of the Melt Pond Study Area, Meteorological Site, Truro Island Base Camp and three oranges tarpaulins.

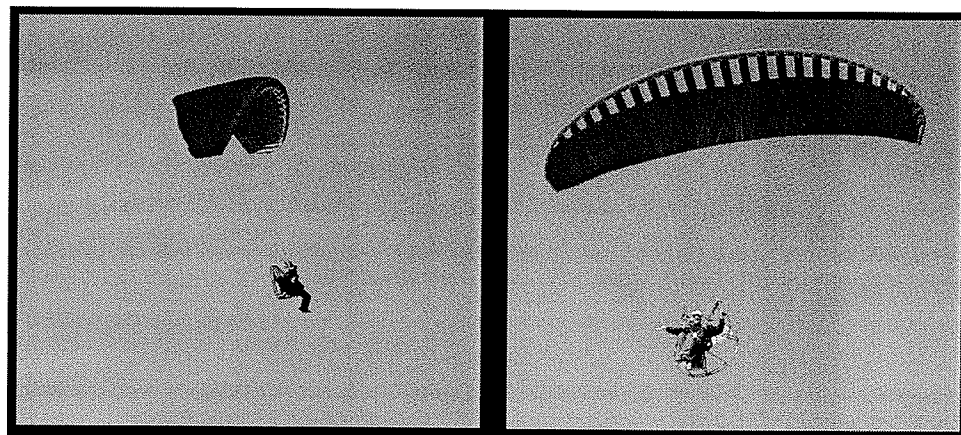


Figure 4.2. Motorized paraglider used during C-ICE 2002. Pilots: Dr. D. Barber (left) and Mr. D. Reimer (right).

The paraglider program was split into two segments during the melt season. Dr. D. Barber piloted the paraglider between YD 168 through 176 while Mr. D.

Reimer flew from 177 through YD 191. The paraglider was equipped with an Everest 4000.4GL infra-red surface temperature transducer, a Licor pyranometer (300-2800nm), and a Campbell Scientific (CS500) relative humidity sensor all connected to a Campbell Scientific 10x logger. Also on board was an Elmo MN42H RGB CCD camera (640x480 pixels) connected to a Sony digital camcorder (s-type connection), and a Trimble GPS Pathfinder Pocket receiver connected to a Compaq IPAQ via TerraSync software. A Trimble base station was also established at the Truro Island Base Camp to allow for differential correction of the paraglider GPS data, minimizing positional error in latitude, longitude and altitude. Digital stills were extracted at a five second interval from the digital video data in concert with the GPS point intervals. The combination of positional attributes with digital stills allowed for an accurate spatial scale to be determined for each image. A list of flight times and corresponding number of digital stills over the study region (meteorological station and melt pond study site) is shown in table 4.1.

Table 4.1. Paraglider flight information for C-ICE 2002.

Flight ID	Day of Year	Start time (CST)	Number of Images	GPS data
T1_0619	170	17:59	141	Y
T1_0620	171	10:25	218	N
T2	172	9:91	355	Y
T3_0621	172	17:02	225	Y
T3_0623	174	15:56	310	Y
T4	175	12:40	442	N
T5	177	10:35	348	N
T6	180	11:57	474	N
T7	183	12:58	150	N
T8	185	14:18	473	Y
T9	186	15:16	548	N
T10	187	12:34	606	Y
T11	189	14:47	166	Y
T12	191	11:38	524	Y

Figure 4.3 shows one of three 5m x 4m orange tarpaulins that were deployed on the ice within the Melt Pond Study Area. The tarpaulins were deployed to visually guide pilots through the study area, ensuring adequate coverage, and to provide a target from which to calculate pixel resolution (r) for the Elmo camera (equation 4.1). The camera was mounted on the cage of the paraglider motor orthogonal to the ice surface. A linear regression model was fitted to images of the tarpaulins taken at varying heights to determine an equation for image scale. This equation was then confirmed during a controlled experiment performed within the CEOS laboratory. The residuals in the model (R^2) were due to errors in camera lens geometry and altitude.

$$r \text{ (m)} = 0.001[\text{height (m)}] - 0.00001, R^2 = 0.9998 \quad [4.1]$$

Initially during the 2002 paraglider collection, the GPS had data blackouts due to a faulty pin in the GPS/IPAQ connector. The problem was eliminated with a new cable and protective case for the IPAQ. For those paraglider flights with GPS blackouts, flight paths were reconstructed using the meteorological site and tarpaulins as location markers. During the GPS blackouts, the pilots maintained a height of approximately 150m above the ice surface (using an in-flight barometric altimeter) to ensure consistent pixel size.



Figure 4.3. Paraglider image captured YD 186. Drainage caused by a seal hole in the upper left corner is evident in the photo along with the 5m x 4m tarpaulin deployed in the Melt Pond Study Area.

4.2.2. Extrapolation of Point Measurements to Regional Scales using Aerial Photography

The use of a powered paraglider for aerial photography proved very successful during the 2002 field season. However, extracting physical and albedo statistics from images required considerable post processing due to the behaviour of the digital camera. Firstly, the camera recorded digital video which was interlaced in order to maximize storage space. Secondly, changes on the surface, mainly the pond fraction from image to image, caused the iris on the Elmo camera (model MN42H) to automatically adjust to associated changes in intensity levels within the field of view (FOV). The changing iris resulted in a shift in the distribution of the image histogram which, in turn, affected the DN range for individual images. Each of these effects had to be taken into account before analysis of images could take place.

Frame capturing from digital video was done using standard video software connected to a PC. Eight-bit black and white intensity images were captured through the study region at five-second intervals corresponding to GPS data. Images were then de-interlaced using even-line interpolation. Vertical black lines form on both sides of the image as a residual of de-interlacing. To ensure a true representation of the surface, images were clipped to 612x480 pixels in order to remove this residual.

The effect of a changing iris during paraglider flights required a shift to the median intensity value to standardize the radiometry across images captured along each flight line. First, a global median value was calculated for each flight based on individual image median values. Then a histogram shift to the global median value was applied to individual images. With histograms aligned, the images were ready for surface type classification.

In order to separate individual surfaces present within images, an unsupervised isodata cluster algorithm was used. Isodata clustering looked for natural breaks within the histogram, similar to density slicing, with groups being identified by minimizing distance from cluster means. Once distance parameters had been set for each cluster, pixels were assigned to representative clusters. During the 2002 melt season a maximum of 8 individual surfaces were identified during sampling sessions. Therefore 8 clusters were requested for each image. The clustering algorithm identified between five and eight clusters per image. Isodata clusters were assigned using remote sensing software (figure 4.4).

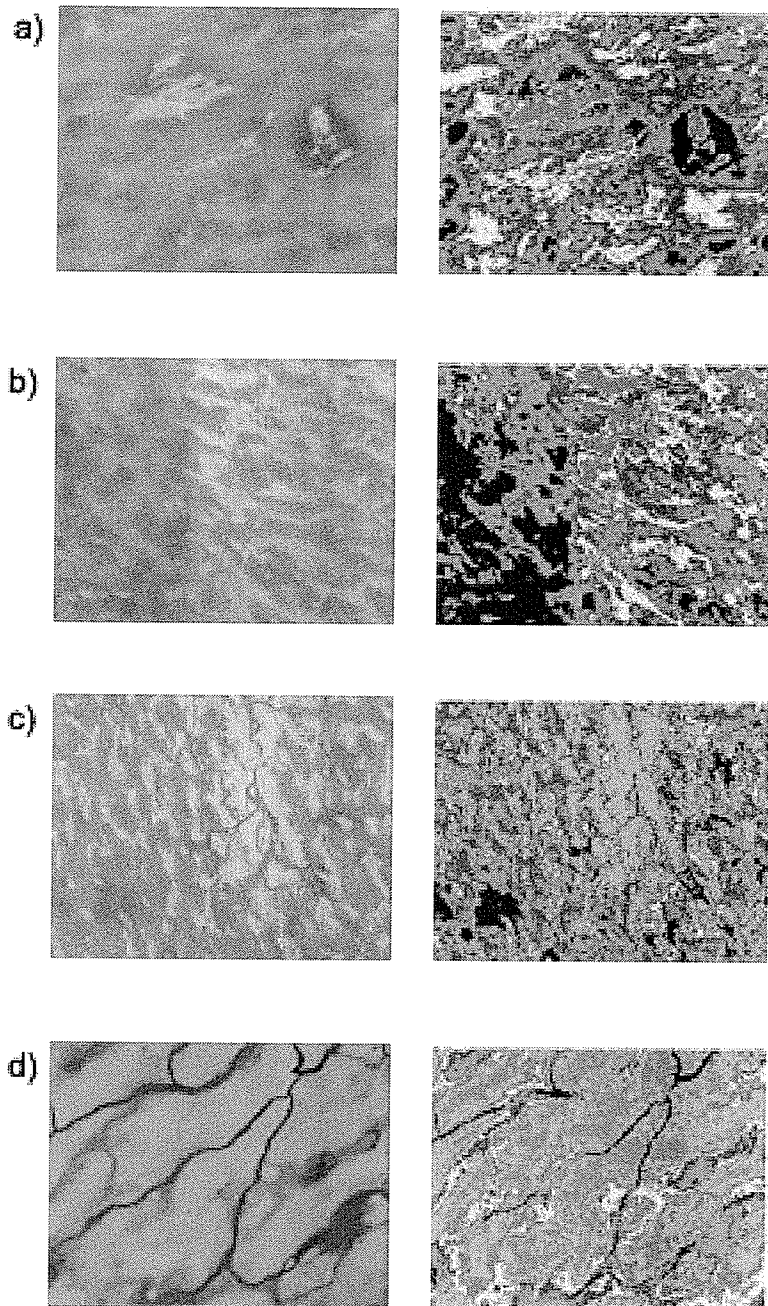


Figure 4.4. The use of isodata clustering on digital photographs of various surfaces observed over the course of the melt season. Images b) and c) show the linear arrangement of melt ponds following snow distribution patterns while both c) and d) illustrate the influence of drainage on pond fraction and corresponding albedo.

With clustering completed, images from individual flights were assigned albedo and physical attributes based on a comparison of individual images to field statistics. Purpose built software allowed images to be viewed along with the associated histogram, clustered image and cluster statistics. A comparison of image cluster statistics to field observations allowed for physical and albedo attributes to be applied to each image. This was done by applying surface type statistics for broadband and integrated albedo, and depth derived in Chapter 3 to the appropriate cluster observed in each image. Image attributes were then exported to a database for further analysis. The programs used for calculating physical and optical characteristics from the digital video are outlined in Appendix C. Figure 4.5 illustrates the process of transforming raw aerial images into physical and optical surface representations.

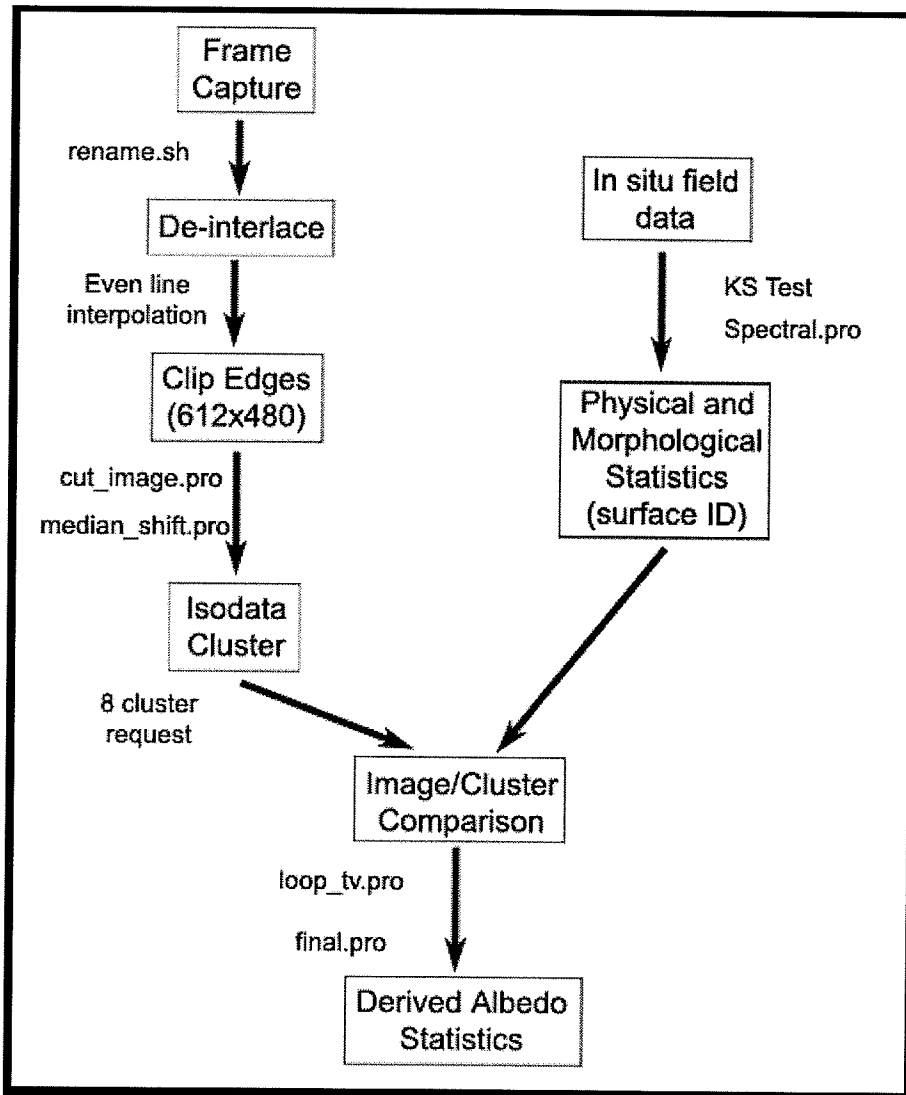


Figure 4.5. Cartographic model for the application of optical and physical surface attributes to aerial images based on representative clusters. Base programs used to apply field statistics to individual aerial photographs can be found in Appendix C.

4.3. Results and Discussion

4.3.1. Regional Physical and Albedo Characteristics from Digital Aerial Photography

Over the course of four weeks, 14 individual powered paraglider flights captured the evolution of melt ponds at a temporal scale previously unattained. Supervision of image clusters based on field observation allowed for local statistics to be derived for both the physical and optical evolution of the FYI surface through the melt season. This combination of aerial photography with field measurements will be used to answer the following research question.

- What is the relationship between surface observations and aerial photography?

Figure 4.6 compares observed pond fractions from individual study sites with derived aerial pond fraction box plots. Differences between estimates are explained primarily through proximity to drainage sites. Also, surface estimates of pond fraction were made for a 100m x 100m portion of the study area whereas aerial estimates incorporate a broader surface area. Aerial flights were conducted at an average height of 150m above the surface providing the camera with a field of view of approximately 273m x 164m. Due to the smaller spatial scale of the aerial photographs, field observations were more sensitive to localized variation in icescape morphology. This difference in resolution was most evident on YD 185 and YD 186 when surface sampling was conducted within a sampling grid

containing a seal hole and well established drainage. In both cases surface pond fraction estimates were observed near 5% and fell outside of the box plot interval for aerial pond fraction.

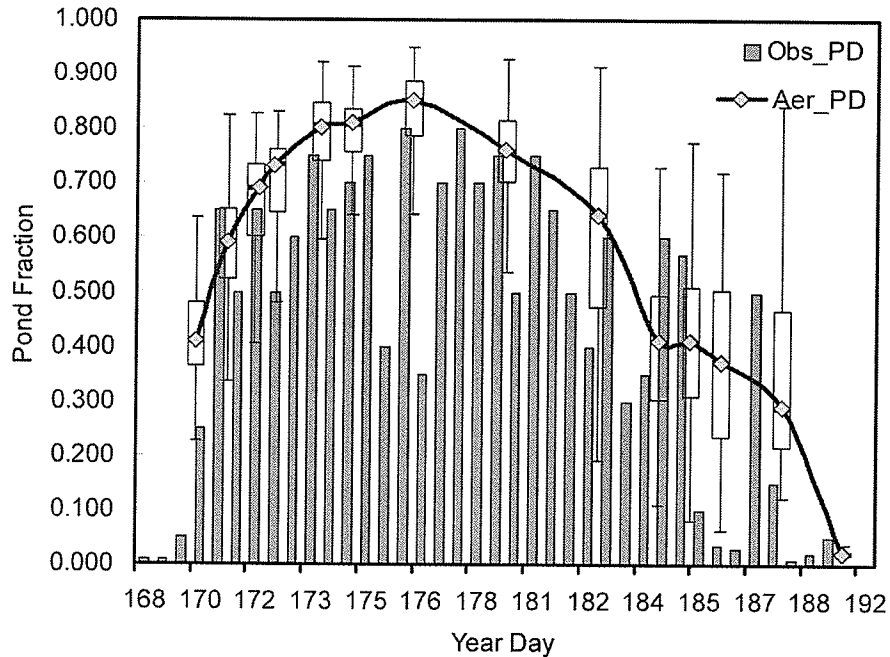


Figure 4.6. Comparison of the temporal evolution of both field observed (Obs_PD) and aerially interpolated (Int_PD) pond fraction. Box plot quartiles are plotted for each aerial photography flights.

4.3.1.1. The Effect of Surface Morphology on Derived Albedo

Figures 4.7 and 4.8 illustrate derived albedo patterns for flight lines captured during the field season. The albedo of integrated (INT), photosynthetically active radiation (PAR), near infrared (NIR) and blue (BLU) portions of the EM spectrum are represented. The albedo for each image was a weighted sum of the representative surface types. As such fluctuations in surface morphology were

represented by the oscillatory behaviour of the albedo trend. Peaks in albedo curves were characteristic of images captured over areas which were dominated by snow/bare ice whereas valleys were representative of surfaces dominated by ponding. As the melt season progressed, the establishment of drainage channels created a preferential drainage pattern across the ice and areas with high degrees of ponding and drainage became increasingly defined.

Table 4.2 outlines the distribution of surface types for individual flight lines and will be used as a reference for explaining the spatial heterogeneity of albedo seen in figures 4.7 and 4.8. The melt season began with a surface dominated with saturated snow and ponds over frazil ice. During this time, the difference in albedo for different increments within the EM spectrum remains quite small (YD 170). This was due to the presence of unponded surfaces with low albedo (saturated snow and transitional frazil ice) and ponded surfaces having a high albedo (ponds with high bubble density). Also, drainage had yet to be established so the distribution of these surface types was relatively uniform with the difference between peaks (minimum pond coverage) and valleys (maximum pond coverage) being small.

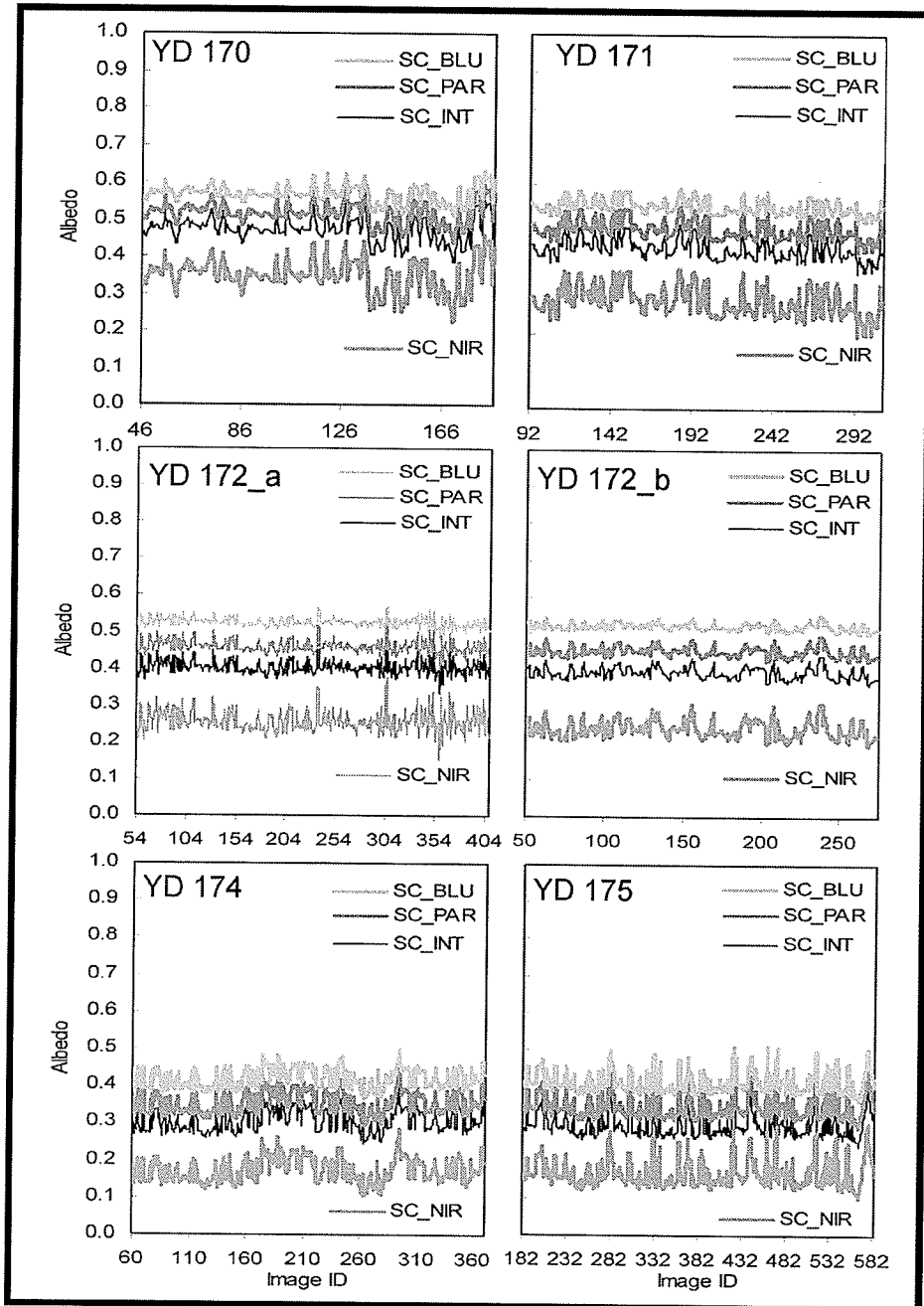


Figure 4.7. Changes in derived surface albedo following flight paths captured between YD 170 and YD 175. The albedo for each flight line is segmented into spectrally integrated intervals for blue (BLU), photosynthetically active radiation (PAR), integrated broadband (INT) and near infrared (NIR). Image ID represents the number of photographs captured having time and position attributes.

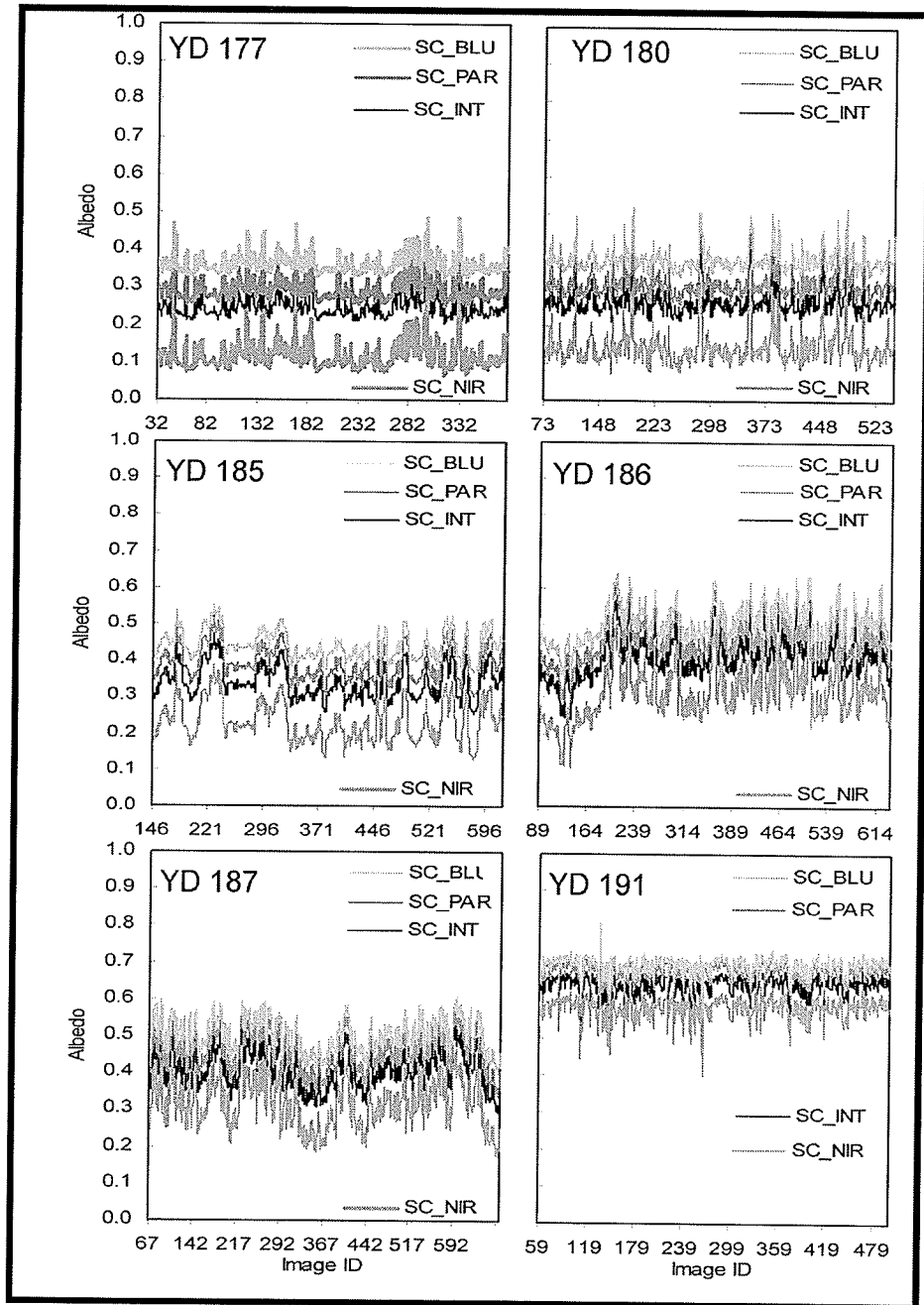


Figure 4.8. Changes in derived surface albedo along flight paths captured between YD 177 and 189. The albedo for each flight line is segmented into spectrally integrated intervals for blue (BLU), photosynthetically active radiation (PAR), integrated broadband (INT) and near infrared (NIR). Image ID represents the number of photographs captured having time and position attributes.

A more defined contrast between peaks and valleys across the flight line was seen on YD 175 (figure 4.7). The larger difference in the magnitude of albedo for individual images captured along flight lines was due to the formation of drainage channels across the surface. As the influence of drainage points began to radiate over the icescape, areas of high and low pond fraction became increasingly defined. Areas of low pond fraction corresponded to high points in the albedo trend while low points were associated with a high degree of ponding. As such, the evolution of the surface from saturated snow and shallow melt ponds with high bubble densities to an icescape composed of the bare ice scattering layer and melt ponds having little to no bubbles, was to increase the contrast in albedo found between ponded and unponded surface types. The influence of surface drainage will dictate the spatial heterogeneity of albedo through the remainder of the melt season.

Table 4.2. The distribution of surface types for individual flights derived from aerial photography through the melt season. Table a) shows seven flights from YD 170 through YD 177 while table b) completes the time series to YD 191. (seal hole – SH; deep melt pond – DP, w/ low bubble density – DP_LB; moderate depth melt pond – MP, w/ moderate bubble density – MP_MB; shallow melt pond – SP, w/ high bubble density – SP_HB; transitional surface – TR; transitional blue surface – TR_B; bare blue ice – BI; new deteriorated ice – NI; new snow – NS; old (mature) deteriorated ice – OI; shallow saturated snow – SS; deep saturated snow – DS; slush – SL).

a) YD	170	171	172	172.5	174	175	177
SH	7.0E-07	1.1E-06	7.0E-07	1.3E-06	8.0E-07	1.1E-06	4.0E-07
DP	0.0000	0.0000	0.0000	0.0003	0.2275	0.2452	0.2440
MP	0.0000	0.0000	0.0000	0.0000	0.3491	0.3652	0.3695
SP	0.0000	0.0000	0.0000	0.0000	0.0041	0.0061	0.2308
DP_LB	0.0032	0.0560	0.1236	0.1949	0.0000	0.0000	0.0000
MP_MB	0.1379	0.2431	0.2889	0.3045	0.0000	0.0000	0.0000
SP_HB	0.2719	0.2877	0.2763	0.2344	0.2172	0.1940	0.0018
TR	0.3044	0.2127	0.0671	0.0362	0.0361	0.0228	0.0433
TR_B	0.0000	0.0000	0.0000	0.0000	0.0000	0.0000	0.0000
BI	0.0000	0.0000	0.0000	0.0000	0.0000	0.0000	0.0000
NI	0.0000	0.0022	0.1697	0.1459	0.0957	0.0910	0.0609
NS	0.0000	0.0000	0.0000	0.0000	0.0000	0.0000	0.0000
OI	0.0000	0.0000	0.0744	0.0839	0.0703	0.0758	0.0497
SS	0.2184	0.1386	0.0000	0.0000	0.0000	0.0000	0.0000
DS	0.0642	0.0596	0.0000	0.0000	0.0000	0.0000	0.0000
SL	0.0000	0.0000	0.0000	0.0000	0.0000	0.0000	0.0000

b) YD	180	183	185	186	187	189	191
SH	9.1E-06	2.5E-05	1.4E-05	2.9E-05	1.4E-05	1.3E-06	9.0E-07
DP	0.2060	0.0049	0.0075	0.0000	0.0760	0.0018	0.0051
MP	0.3218	0.1668	0.1420	0.0207	0.1321	0.0511	0.0000
SP	0.2340	0.2964	0.2653	0.1592	0.1535	0.0000	0.0007
DP_LB	0.0000	0.0000	0.0000	0.0000	0.0000	0.0000	0.0000
MP_MB	0.0000	0.0000	0.0000	0.0000	0.0000	0.0000	0.0000
SP_HB	0.0000	0.0000	0.0000	0.0000	0.0000	0.1157	0.0000
TR	0.0062	0.0000	0.0000	0.0000	0.1297	0.0000	0.0000
TR_B	0.0860	0.1225	0.1229	0.1723	0.0087	0.1963	0.0211
BI	0.0000	0.0000	0.1849	0.0000	0.0000	0.0000	0.0000
NI	0.0794	0.1137	0.1299	0.1563	0.2967	0.0000	0.3005
NS	0.0000	0.0000	0.0000	0.1209	0.0000	0.2325	0.4609
OI	0.0666	0.1193	0.1476	0.1441	0.2032	0.2792	0.1935
SS	0.0000	0.0000	0.0000	0.0000	0.0000	0.0000	0.0000
DS	0.0000	0.0000	0.0000	0.0000	0.0000	0.0000	0.0000
SL	0.0000	0.1763	0.0000	0.2265	0.0000	0.1234	0.0181

The presence of water on the surface was best illustrated by the NIR pattern of surface albedo. As the surface flooded and ponds matured (YD 170 – YD 176), the pattern of NIR stayed noticeably separated from those of the INT, PAR and BLU albedo (figure 4.7). The lower albedo for NIR, as compared to the other increments, was due to the absorption of NIR within the high volume of water found within the saturated snow and transitional surfaces, and the high degree of surface flooding. However, after the surface began to drain on YD 177 and pond fraction was reduced, the spatial trend of NIR was observed to increase toward the other three (figure 4.8). On YD 191, melt ponds had drained from the surface and it was observed during this time that the value of NIR increased to just below that of the INT albedo.

4.3.2. The Relationship between Albedo and Pond Fraction

The relationship between the magnitude of albedo and the type of scattering surface was well illustrated by plotting surface albedo by pond fraction through the melt season (figure 4.9). Here the magnitude of the slope for individual flight regression lines was observed to fluctuate between flights with an increasing trend through the time series. The increases in slope magnitude were attributed to an increased divergence in the magnitude of albedo between melt ponds and snow/bare ice as the season progressed. A statistical approach was used to explore how the albedo of the surface changed over time using the slope (β) of regression lines for each flight. The null hypothesis of $\beta_1 = \beta_2 = \dots = \beta_{14}$ was proposed to the alternate hypothesis that the slopes differed between flights. Table 4.3 outlines the results of the analysis, showing adjacent slopes which were considered similar within a 95% confidence interval. A comment on the state of the surface completes the table.

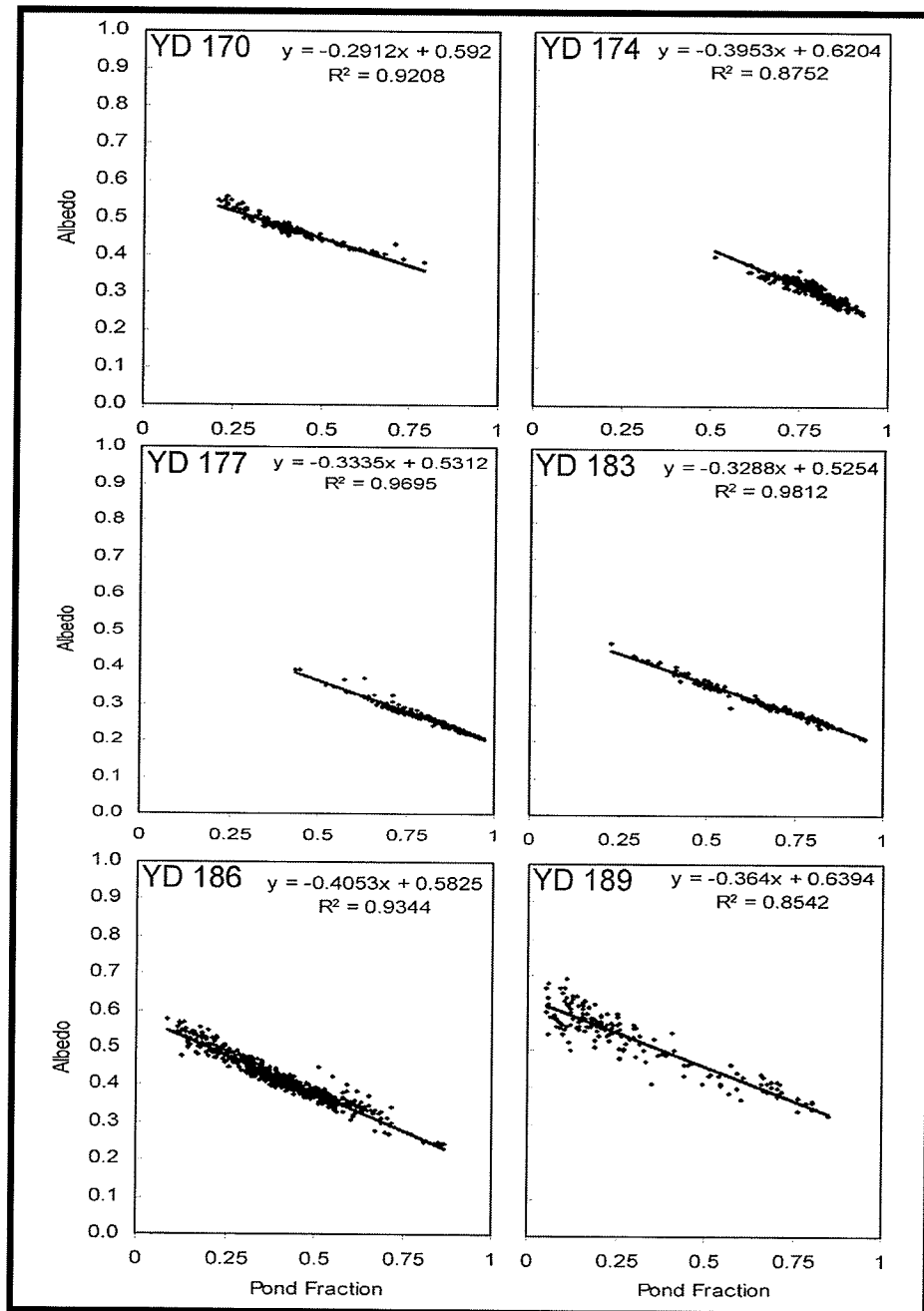


Figure 4.9. The relationship between aerially derived pond fraction and broadband albedo through the melt season. Albedo and pond fraction estimates are based on the weight sum of surface type field statistics applied to each aerial photograph.

Table 4.3. Individual flight slope of regression lines (β) for pond fraction versus broadband albedo. Flights having a statistically similar β suggest four stages of melt pond ablation. Comments outline major contributors to albedo: snowpack (S), pond bubbles (B), mature ponds (P), bare ice (I), maximum pond extent (M), surface drainage (D) and new snow (NS).

Tape ID	YD	β (slope)	Lower limit	Upper limit	Similar β	Comment
t1a	170	-0.2912	-0.306	-0.277		S & B
t1b	171	-0.2368	-0.243	-0.230		S & B
t2	172	-0.1659	-0.175	-0.157		S, B & I
t3a	172.5	-0.1946	-0.204	-0.185		B & I
t3b	174	-0.3953	-0.412	-0.379	4	P, B & I
t4	175	-0.3862	-0.398	-0.374	3b	P, B, I & M
t5	177	-0.3335	-0.340	-0.327	7, 8	D, P & I
t6	180	-0.3068	-0.313	-0.301	8	D, P & I
t7	183	-0.3288	-0.336	-0.321	5, 8	D, P & I
t8	185	-0.3163	-0.330	-0.303	5, 6, 7	D, P & I
t9	186	-0.4053	-0.414	-0.396		D, P & NS
t10	187	-0.3584	-0.371	-0.346	11	D, P & I
t11	189	-0.3640	-0.387	-0.341	10	D, P & NS
t12	191	-0.5794	-0.601	-0.558		D & NS

The confidence intervals for the slope found between pond fraction and albedo demonstrated that the ablating FYI surface was in a constant state of flux through the melt season. This was due to the evolution of surface albedo as the snowpack ablated into bare ice and bubbles were released from the bottoms of melt ponds. From the combination of the 'Similar β ' column in table 4.3 and field observations, it was observed that there appeared to be four distinct periods when the confidence intervals of regression slopes overlap with adjacent flights.

Before YD 172, there was no relationship between the slope of regression lines for albedo and pond fraction. This period was defined as pond onset and the relationship between surface and albedo and pond fraction was in flux due to the

rapid ablation of the snowpack and the presence of frazil ice underlying melt ponds. Field observations show that the complete removal to the snowpack occurred around YD 172 and the bare ice surface scattering layer dominated unponded surfaces thereafter. From YD 174 to YD 175, ponds were developing and expanding and the relationship between pond fraction and albedo remained consistent. This relationship shifts again from YD 177 through 185 as melt ponds matured and again between YD 186 and 189 as the surface underwent drainage. These results suggested there was a temporal pattern to the evolution of albedo over the course of the melt pond season. This pattern of albedo versus pond fraction will be further explored in the next section.

4.3.3. Time Series Evolution of Aerially Derived Albedo

Figure 4.10 describes the evolution of overall broadband (BRD) surface albedo for the study region during the Melt Pond Study. The figure illustrates the behaviour of the surface albedo (SC), unponded (SN) and ponded (PD) albedo based on the bulk characteristics of the study area derived from aerial photographs. The behaviour of the bulk characteristics for each integrated albedo segment over the study area is shown in figure 4.11. An examination of the time series combined with surface observations from Chapter 3 revealed a distinct pattern of pond evolution. This pattern of evolution can be described using four discrete melt pond stages; 1) pond onset, 2) pond development, 3) mature ponds

and 4) pond drainage. Each of these stages had a distinct pond fraction to albedo relationship as outlined in the previous section.

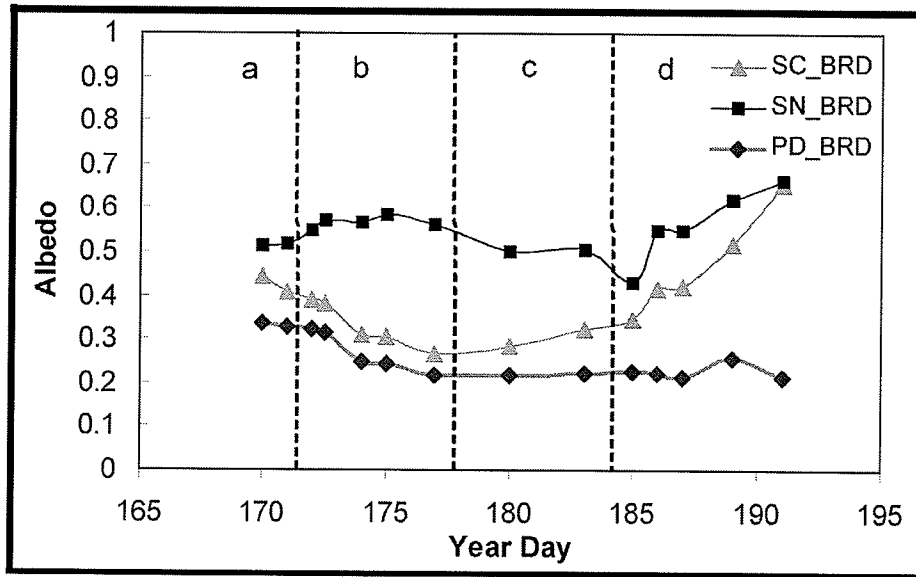


Figure 4.10. Comparison of the temporal evolution of broadband (BRD) study area albedo (SC), pond (PD) and snow/bare ice (SN) albedo estimates for the study area and meteorological station. The graph also illustrates the four stages of melt pond development: a) pond onset, b) pond development, c) mature ponds and d) pond drainage.

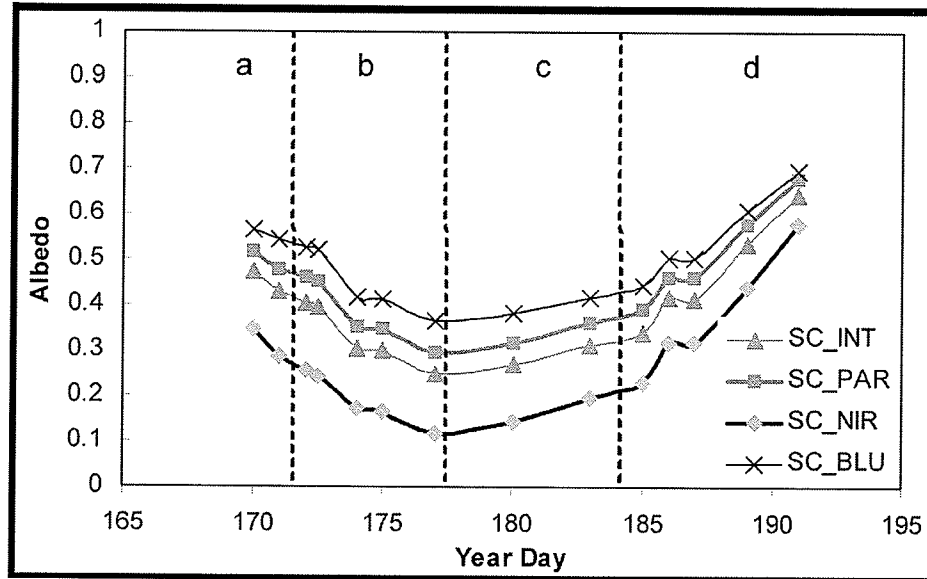


Figure 4.11. This graph illustrates the evolution of integrated spectral albedo over the 2002 season. The four stages of melt pond development; a) pond onset, b) pond development, c) mature ponds and d) pond drainage are also shown.

4.3.3.1. Pond Onset

Pond onset was characterized by the rapid ablation of the snowpack resulting in the formation of ponds. During this time the icescape was composed of a mixture of saturated snow, a transitional surface and puddles overlying frazil ice. The funicular snow regime was well established and the isothermal snowpack was completely saturated with water in liquid phase. Pond fraction was observed to increase rapidly as snowpack melt water flooded the surface. During 2002, pond onset began on YD 168 and finished with the complete removal of the snowpack on YD 171. Pond fraction increased exponentially from 1% to 59% during this time with all ponds containing air bubbles.

The divergence in albedo between ponded and unponded portions of the surface was at its lowest magnitude during pond onset. This was due to the high degree of water within the snowpack and the high degree of bubbles found in ponds. Surface albedo decreases from 0.6, characteristic of the pendular snowpack regime, to 0.4 as the surface became dominated by light melt ponds and saturated funicular snow. Unponded albedo reached its lowest level of 0.52 during this stage due to the high degree of water present in both snow and transitional surfaces while the albedo for melt ponds over frazil ice was observed near 0.33. Figure 4.12 illustrates the surface during pond onset.

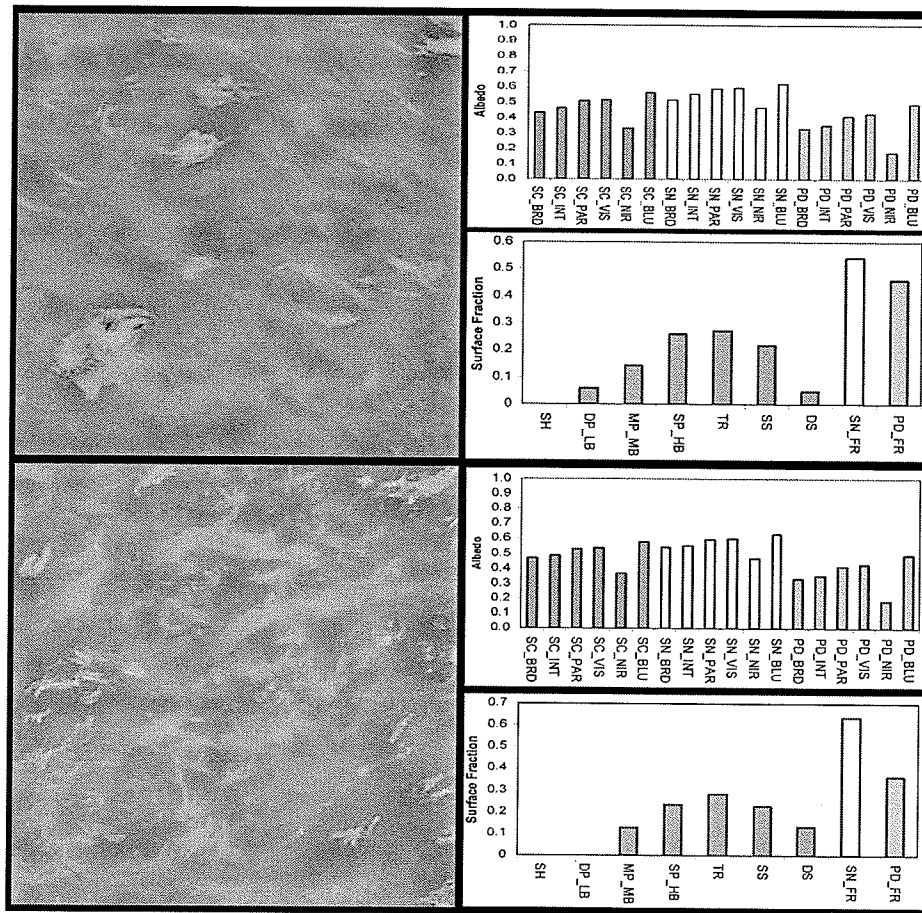


Figure 4.12. Images captured during “pond onset” (YD 168 – YD 171) over first year sea ice. Corresponding derived albedo and surface fraction highlight the physical and optical characteristics typical of this period of surface melt.

4.3.3.2. Pond Development

The pond development stage began with the complete removal of the snowpack and finished when maximum pond fraction was achieved. During this stage, ponds continued to expand as the influence of drainage points had yet to be established. This stage can be accelerated by long periods of high wind, when

mechanical weathering erodes bare ice, increasing pond fraction and decreasing bubble densities (see figure 3.12 in Chapter 3).

The pond development stage exhibited a rapid decrease in pond albedo due to a combination of bubble release and pond deepening which lowered albedo from 0.33 to 0.22. With frazil ice removed, increased solar insolation caused a deepening of the melt ponds, further decreasing the albedo owing to the increased absorption within the water and ice volumes. As pond bottoms continued to ablate, the smooth interface between the water and ice volumes allowed for an increased transmission of solar energy. The preferential scattering and low absorption of wavelengths between 400nm and 500nm within the ice volume resulted in mature melt ponds having a characteristic blue colour.

The pond development stage also saw the formation of bare ice and the bare ice scattering layer. Bare ice patches survived surface flooding along remnants of sastrugi where deep snow previously retarded pond formation. Drainage points had only a local influence during this period of pond evolution, however, as surface drainage began, bare ice will begin to dominate small areas surrounding these points. The establishment of the deteriorated bare ice scattering layer increased unponded albedo to 0.58 with the unponded surface becoming a mixture of transitional, new bare ice and old bare ice surface types. Maximum pond extent was observed on YD 177 when the derived pond fraction approached 85%.

Examples of the optical and physical state of the surface are presented in figure 4.13.

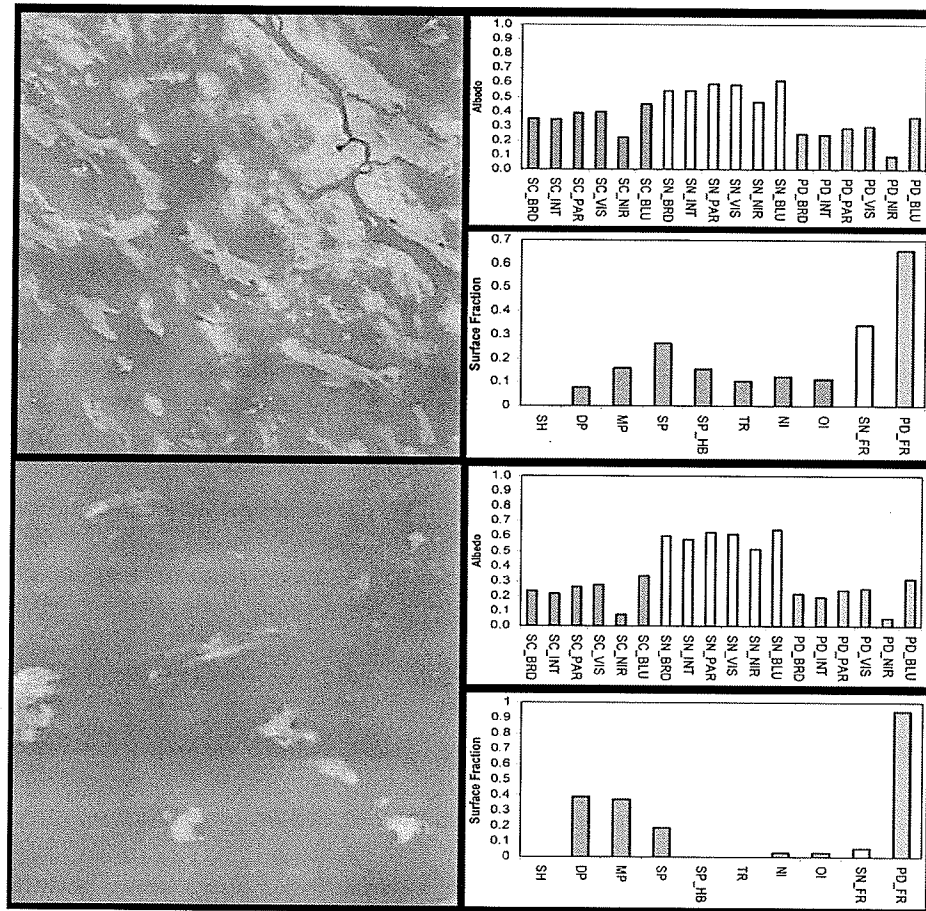


Figure 4.13. During the “pond development” stage (YD 172 – YD 177) of spring melt the effect of surface drainage is limited to a localized area in close proximity to drainage point while the bulk of the surface remains highly flooded.

4.3.3.3. Mature Ponds

After maximum pond extent was achieved, the surface entered the mature pond stage of development. This stage of development was characterized by the establishment of drainage channels spanning out across the icescape from seal

holes, cracks and leads. Surface drainage stabilized the pond fraction between 50% and 60%. The duration of the mature pond stage was dependent on an increase in the percolation rate through the ice volume. The percolation rate remained low until the ice volume became isothermal and brine channels, previously plugged with fresh melt water, began to flow and enlarge. Thus periods of atmospheric cooling will prolong this stage.

Areas in close proximity to drainage points became dominated by bare ice with increasing pond fraction radiating out from these areas during this stage. Pond fractions in close proximity to drainage points were as low as 10% and as high as 70% in areas having no immediate drainage. Figure 4.14 demonstrates difference in the morphology of the icescape as the surface began to drain from maximum pond extent.

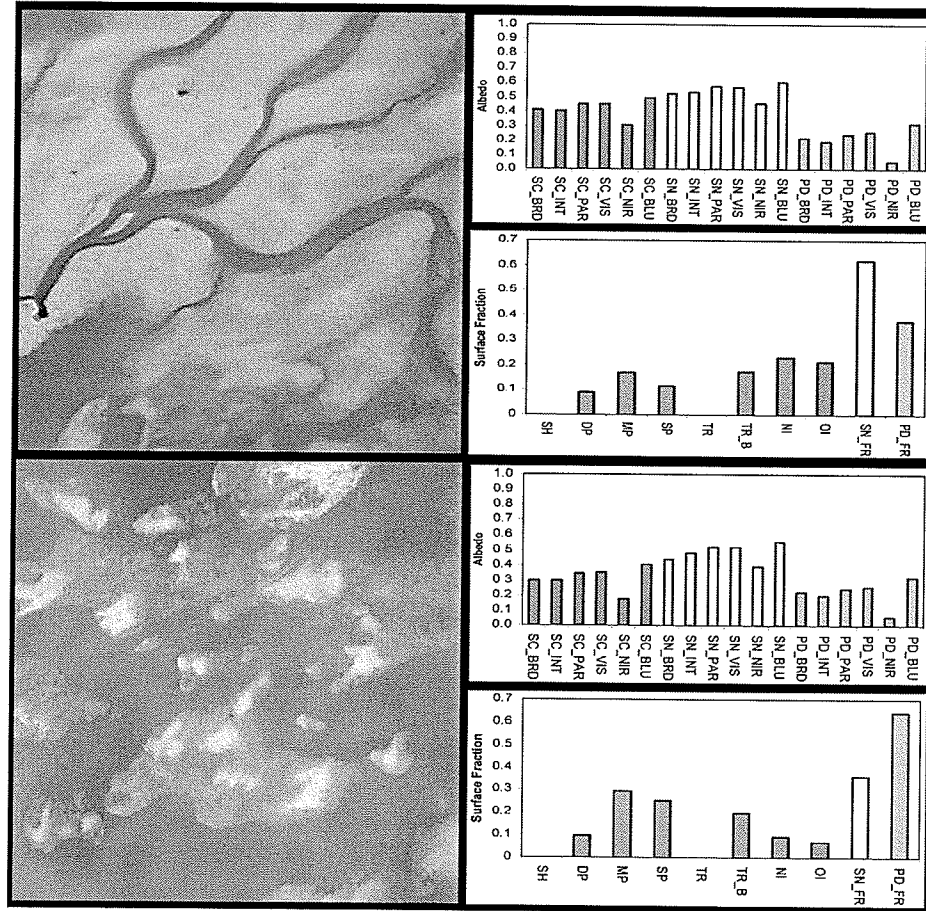


Figure 4.14. The “mature pond” stage of surface ablation (YD 178 – YD 184). As the surface stabilizes after maximum pond extent resulting from drainage channel expansion, previously ponded areas deteriorate into the surface scattering layer.

Generally, it is expected that during the melt season, periods of partly cloudy and clear skies will promote an increase in pond depth due to solar insolation. An increase in the shortwave flux through the ice volume under melt ponds resulted in an increase in ocean temperatures immediately below melt ponds promoting an increase in sub-ice ablation (Eicken et al., 2002). The thinning of the ice volume below the optical depth for FYI (~50cm) allowed for pond bottoms to darken as the optical characteristics of the underlying ocean began to influence albedo. The

continued decrease in pond albedo throughout the melt season has been noted by other researchers (Hanesiak et al., 2001b; Perovich, 1996; DeAbreu et al., 1994). However, during this study, pond albedo remained stable around 0.22 through this stage. It is believed that long periods of cloudy and foggy weather limited solar insolation during the field season thus limiting pond deepening (and sub-ice ablation) which would account for the subsequent decreases in albedo observed by other researchers.

During pond maturity, bare ice patches were a combination of transitional ice surfaces and established bare ice. During surface drainage, the fractional extent of transitional surfaces fluctuated between times of pond expansion and retreat. As ponds began to drain at the start of the mature pond stage, the fraction of transitional surfaces increased. Transitional surfaces have a considerably lower albedo than unponded surfaces. This is due to their shallow depths and high quantities of liquid water. The increase in surface fraction of transitional surfaces resulted in a decrease of bare ice albedo during the mature pond stage. Unponded albedo dropped to 0.51 however the decrease in pond fraction resulted in an increase in overall scene albedo to 0.32 by YD 184. The mature pond stage occurred between YD 178 – YD 184)

4.3.3.4. Pond Drainage

The rapid drainage of the surface signifies the final stage of the melt pond season, pond drainage. A dramatic shift in pond fraction was first observed on YD

185 when pond fraction dropped by 23% from 0.64 to 0.41. Drainage continued through YD 190 when pond fraction estimates of less than 1% were recorded. During the 2002 field season, surface drainage was accompanied by a mixture of snowfall and rain on YD 189 and snowfall on YD 190. The combination of shallow ponds and snowfall resulted in the formation of slush and floating ice crystals within the remaining ponds. This dramatically increased the albedo of ponded surfaces to 0.27 immediately after the snowfall event, as illustrated in figure 4.10. Albedo was then reduced as the snow and slush ablated. With the pond fraction approaching 1%, the FYI volume was termed dry ice. The dry ice was highly porous with brine channels actively contributing to pond drainage.

A consequence of rapid surface drainage was the exposure of blue ice on the surface. Blue ice has the lowest albedo across all wavelengths of the transitional and unponded surface types. The high fraction of blue ice, due to rapid pond drainage, on YD 185 resulted in an unponded surface albedo of 0.43, the lowest observed during the melt season. However, a decrease in the influence of pond albedo resulted in an increase in overall scene albedo to 0.35. Blue ice deteriorated shortly after exposure, evolving into a new deteriorated ice surface scattering layer. As a result the unponded albedo increased to 0.57 on YD 186. Finally, on YD 189 and 190, snowfall over the icescape caused the highest snow/bare ice patch albedo of 0.65. Images captured during pond drainage and dry ice conditions are shown in figure 4.15.

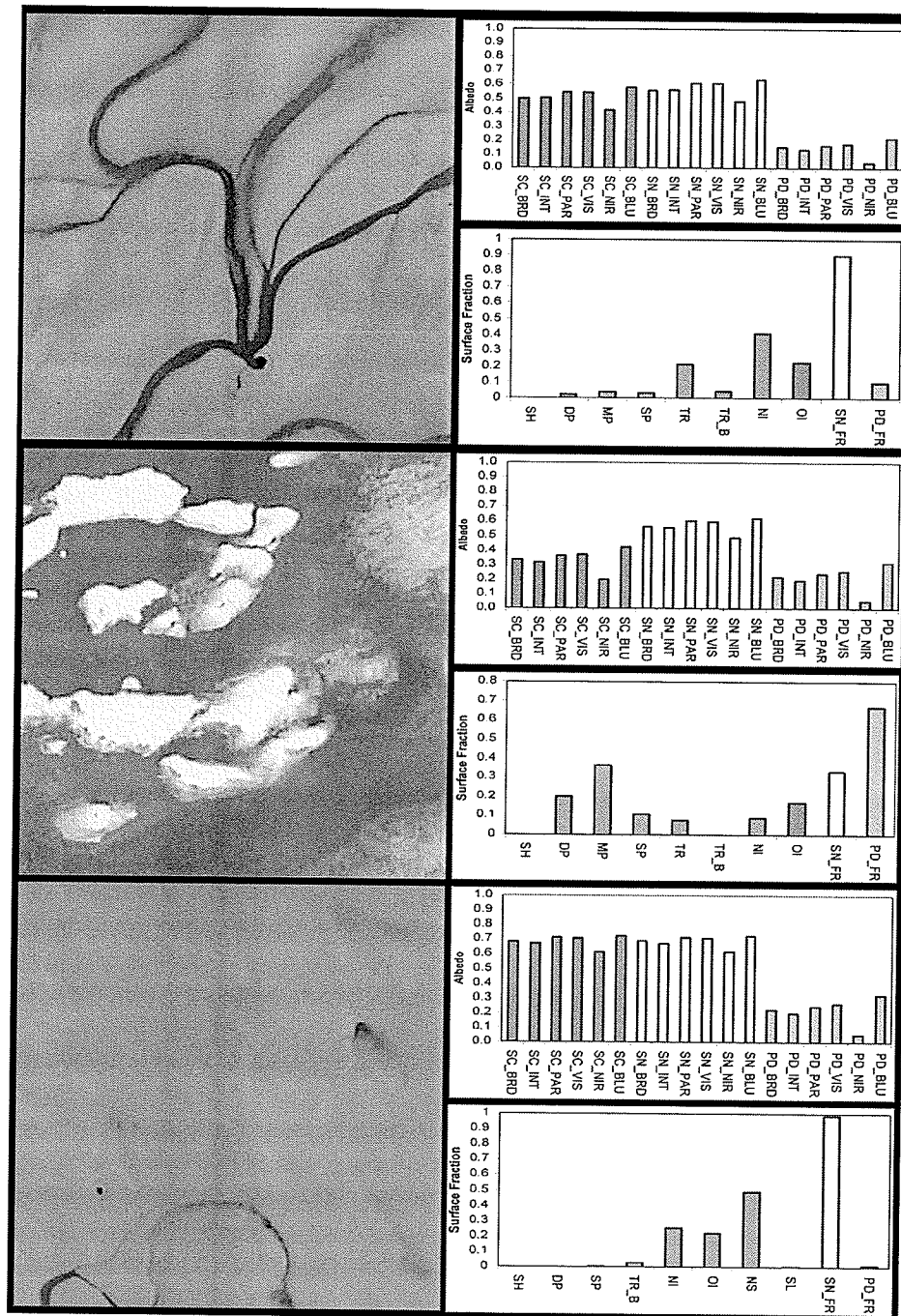


Figure 4.15. The “pond drainage” stage of spring ablation (YD 185 – YD 190). Elaborate surface channels, pond drainage and finally “dry ice” are typical of the pond drainage stage of the melt season.

4.3.3.5. The Effect of Snow on Surface Albedo

The effect of snowfall on surface albedo was dependent on three factors; the depth of accumulation, the amount of bare ice present and the depth of ponds. The depth of accumulation was very important. Trace amounts of snowfall had little or no effect on surface albedo as the snow will melt on contact with the surface. However, with sufficient accumulation of snowfall (>0.5cm) the albedo of unponded surfaces rapidly increased. During this study, an increase in broadband albedo of 22% was observed for shallow deteriorated ice and 9% for deep, mature deteriorated ice. Large accumulations of snow also affected pond albedo as shallow depths are filled with slush and ice crystals floating within the pond volume. Slush had an almost identical albedo to shallow ponds but the presence of floating ice crystals in the pond water caused an increase in shortwave scattering with a subsequent increase in albedo. This effect was similar to the increase in albedo due the presence of bubbles observed in the early stages of pond onset.

The effect of snowfall on YD 182, YD 185, YD 189 and YD 190 was captured by the albedometer (integrated reflectance) and ASD (spectral reflectance) during surface sampling and its contribution to surface albedo was inferred using pond fraction estimates from aerial flights. For the purpose of simplicity, I assumed that there was sufficient snowfall to cover all unponded surfaces with a minimum accumulation of 1cm. A second assumption was that only unponded albedo was

affected during pond onset and pond development. This assumption was valid as the presence of bubble within ponded frazil ice negates the presence of floating ice crystals within the pond. It was also assumed that during the mature pond and pond drainage stage only shallow pond fractions were affected by slush and floating frazil ice. Given these assumptions, changes in surface albedo, due to snowfall across the icescape, were inferred.

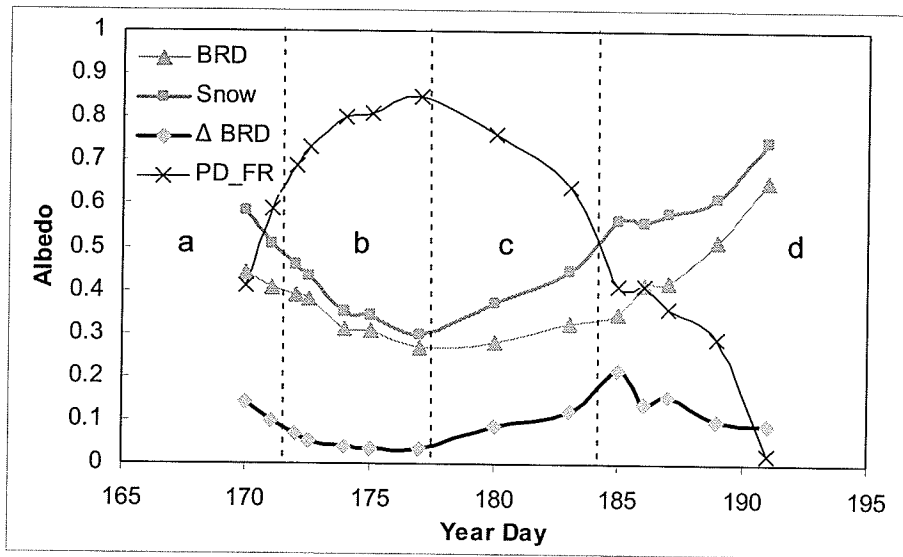


Figure 4.16. The effect of snowfall (snow) on broadband (BRD) albedo during the 2002 melt season. The difference in albedo (Δ BRD) and pond fraction (PD_FR) are also plotted and show the relationship between increased albedo due to the availability of unponded surfaces. The four stages of melt pond development; a) pond onset, b) pond development, c) mature ponds and d) pond drainage are also shown.

Figure 4.16 illustrates the effect of snowfall on the icescape. The relationship between pond fraction, the affect of snowfall, and albedo was evident. During the period of pond development, the surface was flooded with melt water and the addition of snowfall had a minimal effect, averaging an increase of 4.5% in

broadband albedo. The greatest effect occurred immediately after pond drainage when a large fraction of unponded surfaces were covered in transitional surface types (BI, TR_B and TR). An increase in broadband albedo of 21% corresponds to periods of rapid pond drainage. The affect of snowfall was observed for YD 186, YD 189 and YD 191. These flights were taken after snowfall events and it was assumed that the majority of snowfall had ablated previous to the time of data collection.

Although snowfall can have a dramatic affect on surface albedo, it is important to note that the influence of snowfall was short lived as the surface energy balance had sufficient surplus to melt the new snow. If the snow deposition coincides with a decrease in the amount of available energy at the surface it is possible for the system to revert to an earlier pond state or even back to what we could consider pre-melt conditions. During pond onset, snowfall accumulations are expected to be quite rare as the ablating snowpack was isothermal and the majority of snowfall would ablate on contact. Later in the season, the duration of snow accumulations on bare ice often occurred during the night with only a small fraction of snow lasting more than one day. The system functioning in this late season period is still poorly understood and requires further examination of the relationship between surface energy balance and surface type evolution.

4.4. Conclusions

In this chapter the temporal sequence of the spatial physical and optical properties of a melting first year sea ice surface have been presented. The combination of field measurements and aerial photography allowed for an examination of the spatial distribution of the physical and optical characteristics of the surface through the melt season. This was accomplished through the application of known physical and optical surface characteristics observed during the field season to 14 sets of aerial photography. The time period captured began with pond onset and continued through complete drainage of the surface.

A statistical analysis of the relationship between pond fraction and surface albedo revealed that the surface was in a constant state of flux throughout the melt season. The results were attributed to the fractional extent of the 16 surfaces observed as the melt season progressed. A statistical relationship between pond fraction and albedo for different flights within the time series aerial photography dataset revealed four stages of melt pond development over first year sea ice. These ponding regimes follow the evolution of the physical surface and were described as; 1) pond onset, 2) pond development, 3) mature ponds and 4) pond drainage. Over the course of spring ablation, the melt pond – albedo feedback was shown to follow a non-linear evolution with the majority of change occurring during the pond development stage.

The effect of snowfall on surface albedo was found to be dependent on accumulation, pond extent, pond depth and the stage of ponding. During pond onset and pond development the effect of snowfall was minimal as the snowpack was isothermal and pond advance limited accumulation. The averaged effect of snowfall on surface albedo was a 10% increase with the minimal affect occurring during pond development (+4.5%) and the maximum occurring after rapid pond drainage (+21.7%). These estimates are based on the assumption that measurements were taken immediately after snow accumulation as the majority of snow ablated within one day.

In the next chapter, estimates of pond fraction presented within this chapter will be used to examine trends in time series microwave backscatter. The relationship between backscatter and pond fraction will be explored. Once this relationship is established, the physical and optical attributes calculated for each stage of pond development will be applied and the relationship between the physical surface, surface albedo and microwave backscatter will be explored.

CHAPTER 5. EXTRACTING MELT POND CHARACTERISTICS FROM MICROWAVE BACKSCATTER

5.1. Introduction

Synthetic aperture radar (SAR) is a powerful tool for monitoring the transition from winter to spring ablation over smooth, landfast first year sea ice (FYI). This is because of the association of the temporal trend observed in time series SAR backscatter to changes in the thermodynamic forcing across the ocean – sea ice – atmosphere (OSA) interface. The relationship between SAR backscatter and the physical processes acting on the snow and ice volumes is due to the effect of a warming temperature gradient on the electrical conductivity of the volume. This electro-thermophysical relationship provides an estimation of the timing of melt onset and the development of melt ponds over first year sea ice. As such, it has been used for first order geophysical inversion (e.g. Hanesiak et al. 2001b; Yackel and Barber, 2000; Barber and Nghiem, 1999; Jeffries et al. 1997).

In this chapter I will explore the temporal trend of SAR backscatter over the 2002 Melt Pond Study Area and determine if changes in SAR backscatter can be used as an indicator of the four stages of the melt pond season mainly, pond onset, pond development, mature ponds and pond drainage. The in situ physical and optical surface statistics, developed in Chapters 3 and 4, will be used to assess the utility of active microwave remote sensing for determining the

climatological state of the surface during spring ablation. This fulfills the second scientific objective of this thesis, namely to:

- “Construct a link between microwave and optical scattering based on the physical characteristics of the melt surface.”

I will meet this objective by conducting two interrelated investigations set at different spatial scales in order to determine the relationship between changes in backscatter and the stage of spring ablation. First, the relationship of the physical and optical icescape to low resolution microwave backscatter will be investigated using point measures from individual frames of the aerial photography dataset. This will be followed by an investigation on the relationship between the physical and optical characteristics of the icescape to microwave backscatter at the regional scale.

5.2. Data and Methods

RADARSAT-1 SAR data used in this thesis was collected and processed at the Alaska SAR Facility (ASF) and acquired under the permission of the Canadian Space Agency (CSA). RADARSAT-1 follows a circular, sun synchronous polar orbit with a 98.6° inclination and an average elevation of 798km above the Earth's surface. Operating at 5.3GHz, RADARSAT-1 transmits and receives a horizontally oriented pulse (HH) having a 5.66cm wavelength (λ). In standard beam mode, RADARSAT-1 provides surface imaging from 7 beams across a 20° to 49° swath. The ASF standard beam product has a four time look filter applied to the data resulting in a nominal pixel resolution of 100m^2 .

Beginning on YD 89, 105 standard beam ascending and descending RADARSAT-1 images were collected during the 2002 C-ICE field season. A list of the raw RADARSAT-1 data collected can be found in Appendix D. In order to develop a temporal trend, several properties inherent to SAR imagery must be addressed. First, images were calibrated to sigma naught (σ^0) values and geocoded. Then, the images were adjusted for the effect of a changing incidence angle across the swath of the radar pulse. The following sections outline the procedures developed to address these properties.

5.2.1. RADARSAT-1 Calibration and Geocoding

Binary RADARSAT-1 images were archived at ASF using an 8-bit CEOS format with sensor calibration coefficients and image coding information embedded within the header file. Public domain binary SAR processing utilities were applied for radiometric calibration, geocoding and the projection of the RADARSAT-1 data. These “ASF_tools” are a package of programs developed to calibrate and explore CEOS format SAR data and are available through ASF (<http://www.asf.alaska.edu/apd/software/index.html>).

The calibrate utility was used to transform raw binary RADARSAT-1 images to either an 8-bit sigma naught (σ^0), or beam-specific standardized incidence angle gamma values (δ). Values in decibels (dB) were then derived from 8-bit digital numbers (DN) following equation 5.1. The resulting backscatter has a range of 0dB to -25.5dB.

$$\sigma^0 (\delta) \text{ dB} = \text{DN}/10 - 25.5 \quad [5.1]$$

Images were then geocoded using a polar stereographic projection and reduced from 1024 x 1024 pixels to 200 x 200 pixels (20km²) centred just east of the Melt Pond Study Area (75.27N, 97.17W), and a 40 x 40 pixel (4km²) area focused at the centre of the Melt Pond Study Area (75.243111944N, 97.373886194W). Figure 5.1 shows the two areas of interest used to create the SAR dataset. Data were then exported to GIS raster images as well as to ASCII

tables for import into spreadsheets. Program specifications and batch processing routines can be found in Appendix E.

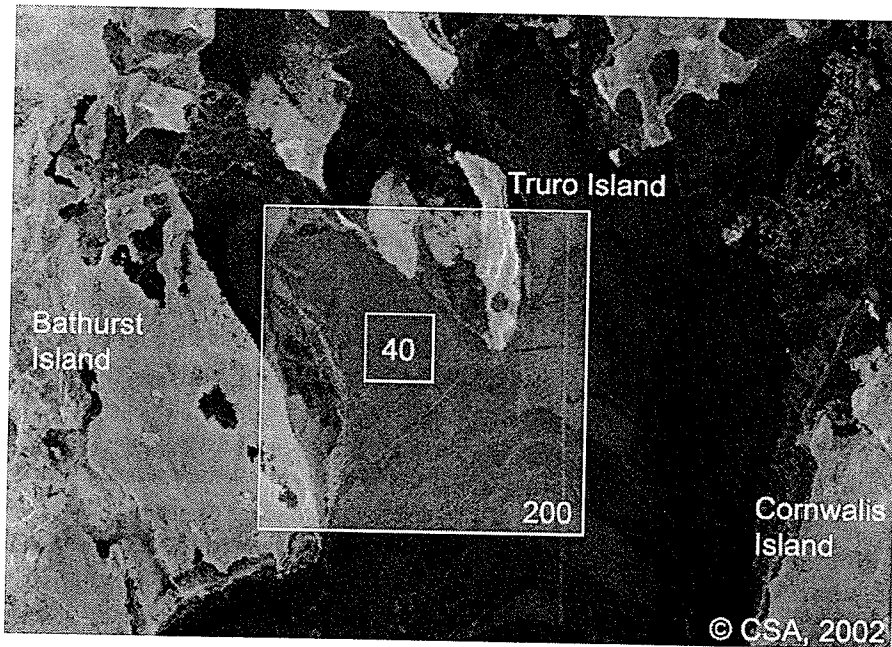


Figure 5.1. RADARSAT-1 image outlining the two spatial areas used in the development of the SAR dataset. The inner square (40) represents the dataset used for calculating the bulk SAR backscatter statistics while the outer square (200) was imported into a GIS format for comparison to aerial flight point data.

5.2.2. Development of the Sigma Naught Temporal Trend

Standard beam RADARSAT-1 data products were collected from a variety of incidence angles (beams 1 – 7). The combination of beams and ascending and descending passes allowed for data to be captured over the study area 5 to 7 times per week. The value of σ° was incident angle dependent. Because incidence angle changes over each beam swath a correction must be made for the effect of incident angle on σ° before images can be compared. Gamma naught

(δ°) is a measure of SAR backscatter which has been adjusted for the effect of changing incident angle across the RADARSAT-1 swath. The value of δ° is independent of viewing geometry which allows for the comparison of backscatter from different beams. The RADARSAT-1 standard beam geometry and the relationship between σ° and δ° are shown in figure 5.2.

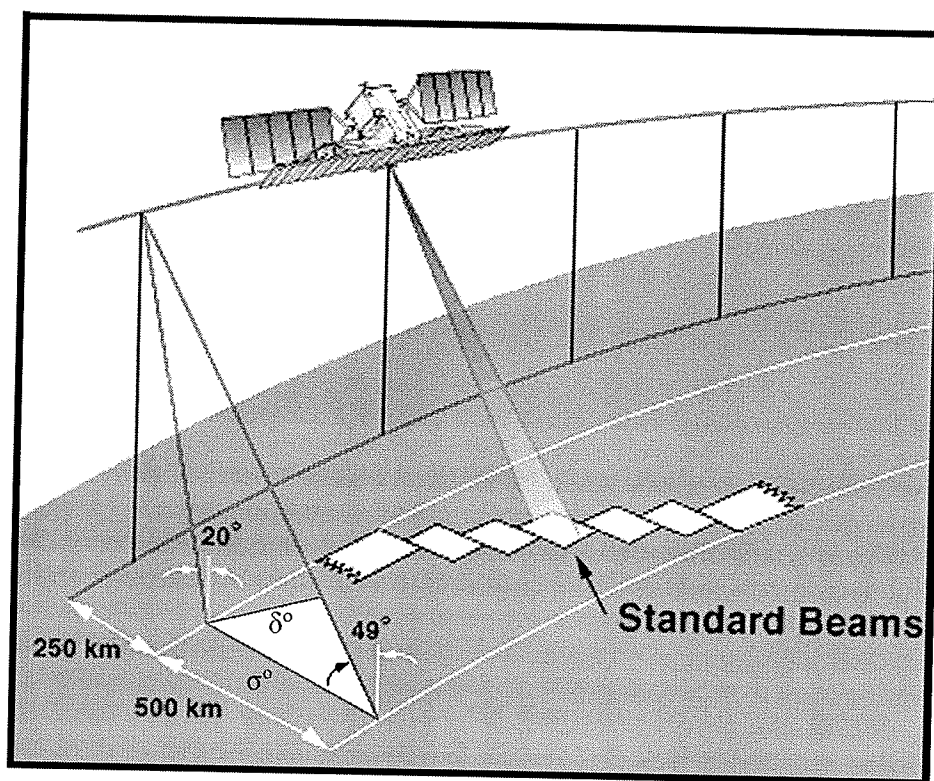


Figure 5.2. RADARSAT-1 standard beam geometry. Radiometric calibration for each beam must be standardized from σ° to δ° before comparison of backscatter can be made. (Adapted from the Canadian Centre for Remote Sensing website, 2004).

The theory behind the winter model method developed by Yackel and Barber (2000) was applied to the 2002 dataset with one modification (see Chapter 2.4.3). ASF now provides the gamma algorithm (δ) which corrects for the effect of

incidence angle across the swath of individual beams. Using this option simplifies the correction function to a scalar shift between beam modes. The scalar shift coefficient (ω) can then be applied to individual beams in order to standardize images to a designated incidence angle (δ°).

The Incidence Angle Calibration Model (IACM) dataset included ascending and descending images captured between YD 89 and YD 120, representing beams 1,2,3 and 7. Because there is no meteorological information regarding the state of the snow – ice interface during this time, data used to create the IACM was analyzed for outliers by limiting the standard deviation of backscatter for each beam to 1dB. The limitation of the standard deviation to 1dB ensures that the atmospheric and oceanic forcing across the OSA interface remained constant through the winter sampling period. This constraint limited the dataset to 30 images from which gamma values were extracted using 9 points within the Melt Pond Study Area. A relationship between δ values and standard beam was then established and scalar coefficients were calculated to shift σ° values to δ° values. Once shift coefficients were applied, the temporal trend was plotted for the entire dataset. The granule, year day, orbit and beam mode used in the creation of the IACM are shown in table 5.1.

Table 5.1. The RADARSAT-1 dataset used for calculation of winter incidence models.

Granule	Year Day	Standard Beam	Orbit
R1_33734_ST1_191	111	1	Ascending
R1_33357_ST1_260	84	1	Descending
R1_33500_ST1_259	95	1	Descending
R1_33600_ST1_259	102	1	Descending
R1_33600_ST1_260	102	1	Descending
R1_33700_ST1_259	109	1	Descending
R1_33700_ST1_260	109	1	Descending
R1_33843_ST1_259	119	1	Descending
R1_33434_ST2_190	90	2	Ascending
R1_33434_ST2_191	90	2	Ascending
R1_33677_ST2_189	107	2	Ascending
R1_33677_ST2_190	107	2	Ascending
R1_33457_ST2_259	92	2	Descending
R1_33457_ST2_260	92	2	Descending
R1_33557_ST2_260	99	2	Descending
R1_33657_ST2_260	106	2	Descending
R1_33657_ST2_261	106	2	Descending
R1_33477_ST3_189	93	3	Ascending
R1_33477_ST3_190	93	3	Ascending
R1_33820_ST3_189	117	3	Ascending
R1_33820_ST3_190	117	3	Ascending
R1_33414_ST3_260	89	3	Descending
R1_33514_ST3_261	96	3	Descending
R1_33614_ST3_260	103	3	Descending
R1_33614_ST3_261	103	3	Descending
R1_33506_ST7_188	96	7	Ascending
R1_33506_ST7_189	96	7	Ascending
R1_33606_ST7_188	102	7	Ascending
R1_33606_ST7_189	102	7	Ascending
R1_33849_ST7_188	120	7	Ascending
R1_33849_ST7_189	120	7	Ascending

5.2.3. Associating SAR Backscatter to Point Surface Properties

RADARSAT-1 SAR data and aerial GPS data from the melt season (see Chapter 4) was imported into commercial GIS software. The GPS data was limited to points covering the Melt Pond Study Area and a corridor which links the study region to the meteorological station. Geophysical surface statistics, derived in Chapter 4 (physical and optical), were added as attributes to the GPS data. A backscatter attribute (σ^0) was appended to the GPS coverage database and the value of σ^0 was assigned to each point based on geographic location. The dataset includes melt pond fraction, optical albedo and corrected sigma naught values.

5.3. Results and Discussion

5.3.1. The Temporal Evolution of Sigma Naught

The temporal evolution of sigma naught over smooth, first year sea ice has been shown to include geophysical information within the transition of the surface from winter to summer (e.g. Breneman, 2003; Kirk, 2001; Yackel and Barber, 2000; Barber and Nghiem, 1999; Fetterer and Untersteiner, 1998; Jeffries et al. 1997). This transition is observed within the temporal trend because microwave sensors are able to detect changes in the dielectric nature of the FYI volume. The use of multi-beam data from RADARSAT-1 has the advantage of improving the temporal resolution of the dataset. However, the difficulty with using beams with varying viewing geometry is that changes in backscatter become a function of the dielectric properties of the surface and the effect of incidence angle. In order to ensure that changes within the temporal trend are strictly a function of thermodynamically driven changes to σ^0 , a correction for viewing geometry must first be made (Yackel and Barber, 2000).

During winter the temperature at the snow/ice interface was cold ($<-11^{\circ}\text{C}$) and the dielectrics of the FYI volume can be assumed constant. Thus, any change to SAR backscatter during this time was a function of surface roughness and incidence angle. In our case the assumption of smooth FYI was valid. Our study area was located amongst fast ice which formed within a single consolidation period (figure 5.3). Further, surface observations made during the field season

confirmed the study region was located over smooth FYI. This eliminated the surface roughness term and confined changes in backscatter observed by the sensor to changes in the incidence angle of the microwave illumination beam.

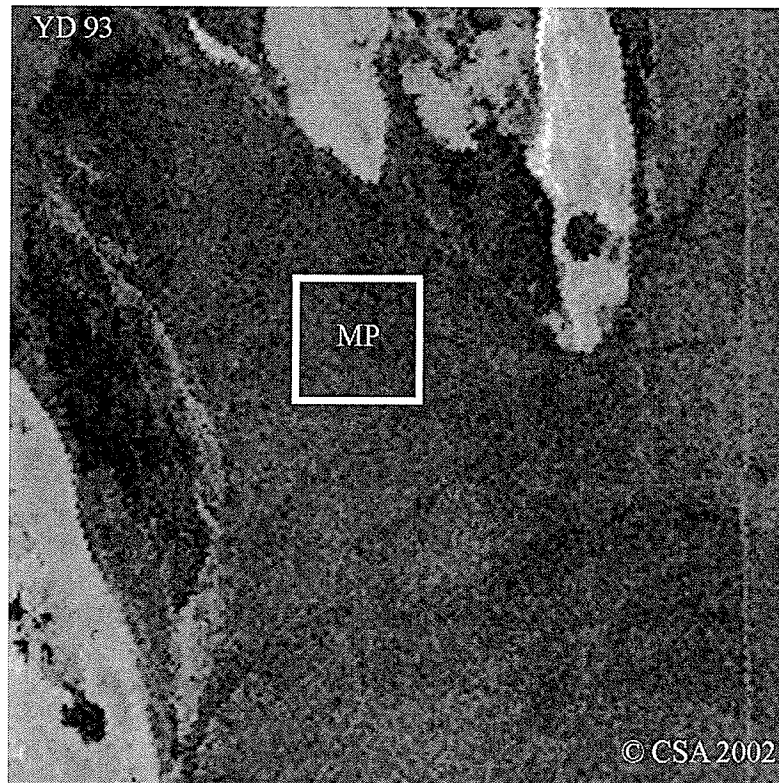


Figure 5.3. RADARSAT-1 standard beam 3 image captured on YD 93. Notice the consistent texture of the FYI surface suggesting a smooth, homogeneous volume. This image has undergone radiometric calibration and was standardized for incidence angle effects with the Melt Pond (MP) Study Area outlined in white.

Using beam specific standardized δ values, a model was created to account for the effect of incidence angle between RADARSAT-1 standard beam modes. The Incident Angle Calibration Model (IACM) standardized σ^0 to the near range of the RADARSAT-1 swath (δ^0). The IACM explained in excess of 99% of the variability in backscatter which resulted from changes in incidence angle (figure

5.4a). Figure 5.4b shows the shift coefficient (ω) applied to each beam. The linear model fitted to the shift coefficient was the first derivative of the relationship between backscatter and incidence angle (beam mode). Equation 5.2 expresses the formula used to standardize gamma values. For the remainder of this discussion, backscatter (σ^0) will refer to this corrected value.

$$\sigma^0 (\delta^0) = [\delta_n + (\omega_{(n-1)} + \omega_{(n-2)} \dots + \omega_1)], n > 1 \quad [5.2]$$

Where σ^0 is backscatter standardized to the near range of the sensor (δ^0), δ_n is the gamma value for RADARSAT-1 standard beam (n), and ω is the shift coefficient specific to the standard beam mode interval, (n – 1). It is important to note that there is no shift coefficient for standard beam 1 (n > 1) as calibrated δ values default to the near range of the sensor. Finally, shift coefficients are cumulative and must be summed for progressive increments in beam modes.

Once backscatter has been adjusted for the effect of incidence angle, the temporal trend of σ^0 was developed. The temporal trend within the Melt Pond Study Area was used to determine how microwave backscatter changed as the surface evolved from winter to spring melt.

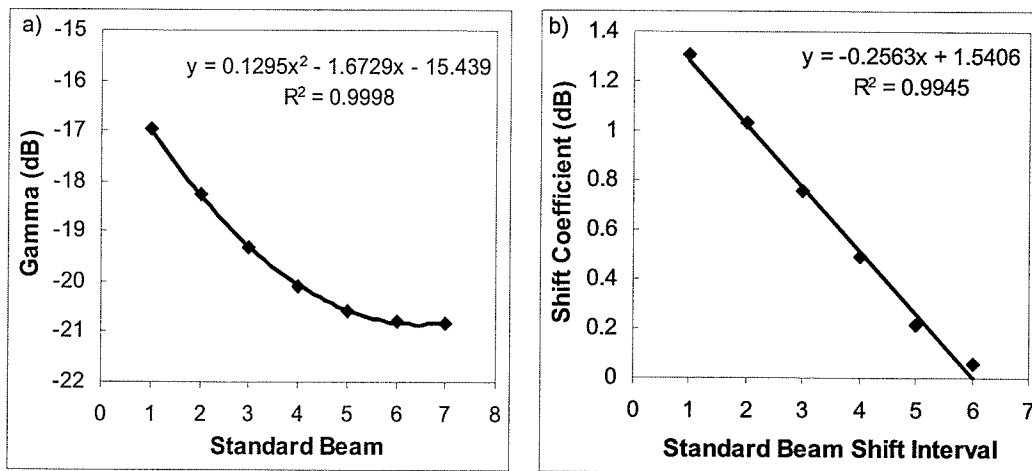


Figure 5.4. The RADARSAT-1 backscatter coefficient (σ^0) as a function of standard beam incidence angle observed during the winter season. a) Second order polynomial model of backscatter (δ) values averaged over 9 sites within the study region. b) Shift coefficient (ω) for standardizing RADARSAT-1 standard beam backscatter to the near range. The shift interval ranges from 1 – 6 corresponding to the standard beam interval n , $n+1$ where $n > 1$ (ie. beams 2, 3).

The temporal trend shown in figure 5.5 has been averaged over nine points within the Melt Pond Study Area and was considered representative of the region. The trend included data captured during ascending and descending passes of the RADARSAT-1 sensor. As descending passes were imaged during the morning (0930 CST) and ascending passes were captured during the late afternoon (1800 CST), information on the diurnal cycle was embedded within the temporal trend. The magnitude of microwave backscatter and the variability observed within the diurnal cycle revealed changes in seasonal stages defined as 'winter', 'transition', 'melt onset', and 'melt ponds'. In the following sections, a brief interpretation of each surface state will be given.

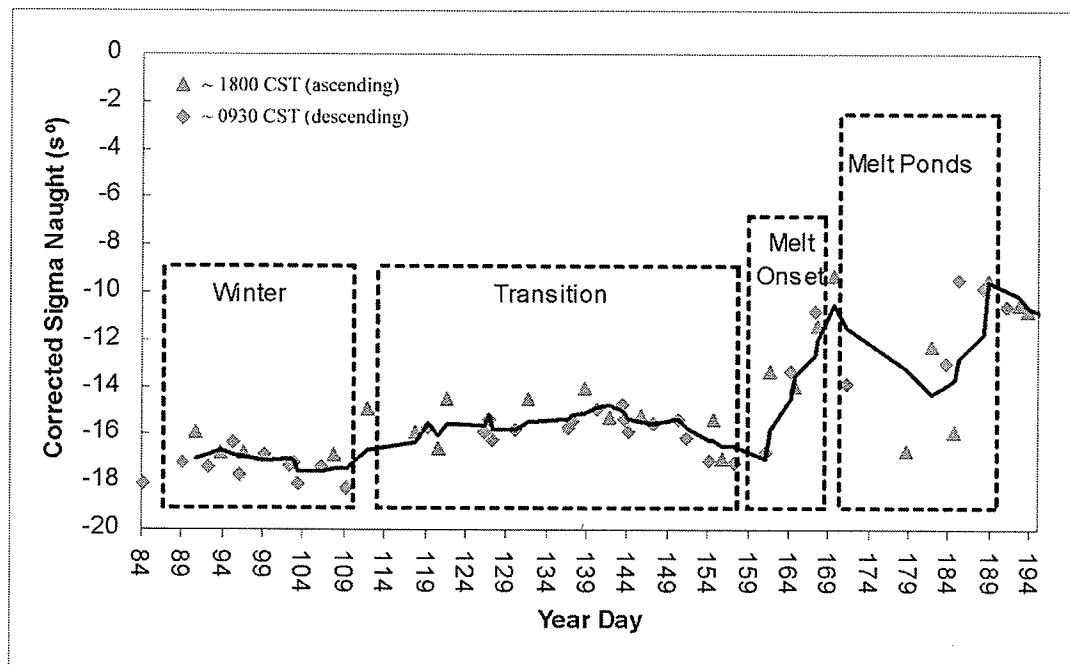


Figure 5.5. Temporal trend of σ° for the 2002 Melt Pond Study. Dashed boxes envelop observed backscatter for winter, transitional, melt onset and melt pond surface states as described in the text.

5.3.1.1. Winter

During winter, σ° was low and stable as the snow/ice interface had a sufficient dielectric mismatch that the majority of microwave energy was reflected off the smooth ice surface and away from the sensor. Any backscatter recorded by the sensor was due to volume scattering by air and brine pockets found within the frazil layer of the FYI volume and/or brine wetted crystal in the basal layer of the snowpack. However, oscillations were seen during the winter period due to changes in the equilibrium between the oceanic and atmospheric heat fluxes (see section 2.4.5).

During the winter period, changes in the atmospheric heat flux can be inferred by examining the temporal trend for noticeable increases in backscatter for images captured during the afternoon (Barber and Nghiem, 1999; Barber and Thomas, 1998). In 2002, only one noticeable oscillation was observed between descending (~0930 CST) and ascending (~1800 CST) passes. The oscillation seen between YD 89 and YD 91 suggested that a warming trend moved through the study region. The variance during the winter period was 0.428 with the averaged ascending/descending pass values for σ^0 equivalent to -16.695dB/-17.446dB. Winter conditions prevailed over the study site until YD 109.

5.3.1.2. Transition

The transitional stage of the SAR temporal trend encompassed the late winter and early melt stages of the FYI lifecycle. It was distinguished by a moderate increase in overall backscatter as well as a discernable increase in variability within the diurnal cycle. During the transitional period, ambient temperatures remain below freezing but daytime warming was sufficient to allow for the temperature of the snow/ice interface to rise above -11°C. Daytime warming initiated a diurnal temperature wave through the snowpack. This warming/cooling trend caused an oscillating temperature gradient through the snow and ice volume (Hanesiak et al., 2001b). This cyclical diurnal pattern was characteristic of microwave backscatter during the first half of the transitional period (YD 110 – YD 139).

In the latter portion of the transitional stage, increased ambient temperatures throughout the diurnal cycle reduced the temperature gradient through the snowpack. As the temperature gradient moved toward isothermal, the crystal grain size and brine volume concentrations remained high in the basal layer. This stabilized backscatter and caused the cyclical diurnal pattern of σ^0 to diminish (YD 140 – YD 153).

Finally, the end of the transitional stage was characterized by a dip in backscatter of about 1.5dB on YD 154. The mechanism responsible for this dip was the advection of cold air into the area, resulting in a reduction in brine volume thereby reducing volume scattering. As brine volume decreased, the reduction in volume scattering corresponded to an increase in surface scattering along the snow – ice interface. Ambient air temperatures recorded at the meteorological station confirmed that the maximum daytime temperature decreased from 0.235°C on YD 153 to -1.20°C, -2.46°C, -2.79°C and -0.78°C between YD 154 and YD 158 before maximum daily temperatures rose above the freezing mark on YD 159.

During the transitional stage, average backscatter for ascending/descending passes increased to -15.342dB/-15.726dB with an associated increase in variance to 0.555. For 2002, the transitional stage began on YD 111 and finished on YD 158.

5.3.1.3. Melt Onset

Melt onset began with the presence of liquid water within the snowpack throughout the diurnal cycle. Wet snow metamorphosis transformed the snowpack to the pendular regime and water was held within the crystal lattice structure. The increase in water volume further stimulated grain growth and brine wicking. The resulting increase in snow volume dielectrics caused an exponential increase in backscatter during the initial stage of this period. During melt onset, water held within the pendular regime caused a maximum σ^0 value of -13.32dB on YD 165.

As the temperature gradient within the snowpack approached isothermal, a transition from the pendular to the funicular snow regime was observed. The resulting drainage of the upper portion of the snowpack flushed salinity from the snowpack and the upper portion of the ice volume (Yackel and Barber, 2000). This transition was observed on YD 165 when σ^0 captured during the afternoon dropped below σ^0 obtained during the morning sensor pass (-13.32dB at 0800/-13.92dB at 1800).

Within the funicular regime, a 'dielectrically rough' scattering surface developed along the snow/ice interface as a consequence of the uneven distribution of melt water within the snowpack. The undulating pattern of water within the snow volume contributed to the highest level of σ^0 observed during snowpack ablation (-9.28dB). Once the snowpack entered the funicular regime, the melt rate accelerated and melt ponds rapidly formed. During the melt onset

stage of spring ablation the averaged ascending/descending value for backscatter was -13.634dB/-14.511dB with a variance of 5.743.

5.3.1.4. Melt Ponds

The melt pond stage of surface ablation was easily identified as it followed the peak in the temporal trend on YD 169. During the melt pond stage, backscatter was extremely variable as σ^0 became a function of pond fraction and wind velocity. Averaged ascending/descending backscatter during this stage was -12.570/-11.049 having a variance of 7.382. The melt pond period of spring ablation began on YD 168 and lasted until YD 190.

In the following sections, the melt pond portion of the temporal trend will be explored in detail. I will first look at the effect of wind on the dataset. Then, by combining RADARSAT-1 backscatter with surface and aerial derived surface characteristics, the four melt pond stages of evolution outlined in Chapter 4 (pond onset, pond development, mature ponds and pond drainage) will be identified within the temporal trend.

5.3.2. The Effect of Wind on SAR Signatures over Melt Ponds

Over the course of the melt pond ablation period, SAR signatures took on a wide range of values (figure 5.5). The variability in σ^0 has been shown to be a function of pond fraction, incidence angle and wind speed (Yackel and Barber, 2000). The effect of incidence angle was addressed using the IACM thus

fluctuations in σ^0 over the course of the melt pond season were attributed to changes in pond fraction and wind speed. In this section, I address the effect of wind speed on SAR signatures during the melt pond season.

Under calm conditions, volume scattering within bare ice (σ_i) results in backscatter which is greater than backscatter caused by surface scattering from melt ponds (σ_m) (Jeffries et al. 1997). So long as this relationship is maintained, an estimation of melt pond fraction from backscatter is possible. However, wind traveling across the melt pond surface has been shown to alter this relationship (Yackel and Barber, 2000). As wind speeds increase, surface roughness also increases due to the formation of wave trains across melt ponds. As discussed in Chapter 2, this results in an amplification of σ^0 as a function of wind speed.

Figure 5.6 clearly illustrates the incoherent backscatter signatures observed when wind speeds range between 1.5ms^{-1} and 2.5ms^{-1} (YD 171, YD 181 and YD 183). This effect was due to an increase in the surface roughness of melt ponds resulting in the values of σ_m becoming equal to σ_i . The effect of higher wind speed was observed in data captured on YD 178 and YD 184. The data captured during periods of high wind velocities ($>4.6\text{ms}^{-1}$) illustrated the separation of backscatter from surface scattering (melt ponds) and volume scattering (bare ice). Areas having low backscatter (dark) were attributed to areas dominated by melt ponds, that is $\sigma_m < \sigma_i$. However, this result was in contrast to the relationship found between σ^0 and wind speed reported by Yackel and Barber (2000). In their work,

periods of high wind speed caused backscatter over melt ponds to be in excess of backscatter values for bare ice patches ($\sigma_m > \sigma_i$).

The negative relationship of low backscatter during times of high wind speed observed in the 2002 dataset can be explained by wind direction. RADARSAT-1 is a right looking sensor following a polar orbit. This means that the illumination pulse travels approximately west to east for ascending passes and conversely for descending passes ($90^\circ \leftrightarrow 270^\circ$). If wind direction was taken into account for data captured on YD 178 and YD 184, both data acquisitions were taken under wind directions following a south – north orientation ($180^\circ \rightarrow 0^\circ$). Under these conditions, the wind direction created wave trains oriented orthogonal to the incident SAR pulse and thereby minimized their effect on surface scattering. This suggested that data used for the investigation by Yackel and Barber (2000) had wind directions which were parallel to the sensor thus causing an amplification of σ° over ponded surfaces.

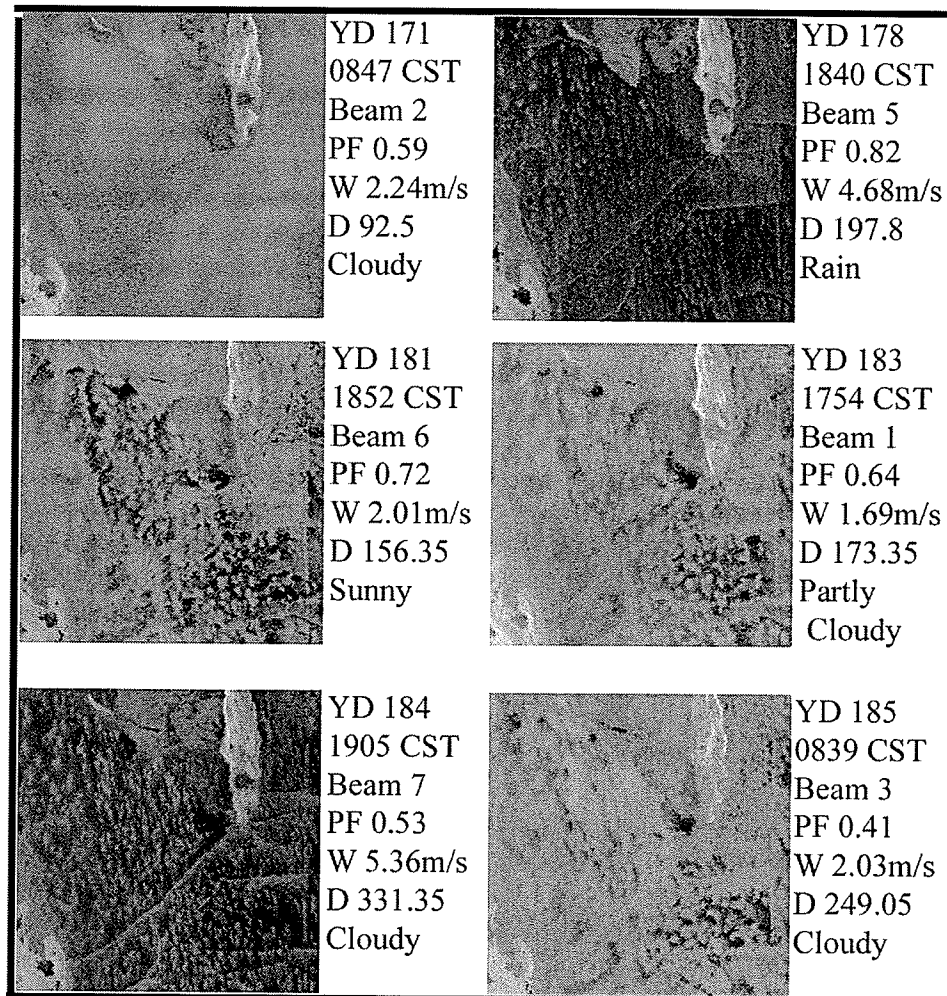


Figure 5.6. The effect of wind on SAR backscatter. Pond fraction (PF), wind speed (W), wind direction in degrees (D) and weather are all indicated for each image. The images have been corrected for viewing geometry and areas of low backscatter appear dark. All images are courtesy of the Canadian Space Agency (© CSA, 2002).

The effect of wind on σ^0 will be referred to in this work based solely on my personal observations and will not be rigorously tested. The effect of wind on SAR signatures will be explored in detail in the thesis work of Randall Scharien at the University of Calgary.

5.3.3. The Relationship between Microwave Backscatter and FYI Pond Fraction during the Melt Pond Season

Over the course of the melt pond season, microwave backscatter at 5.3GHz was a function of volume scattering within snow/bare ice patches and surface scattering along the pond water – atmosphere interface. The objective of this section is to explore the use of RADARSAT-1 standard beam data as a means of estimating the geophysical and optical state of the surface. The use of physical and optical surface statistics developed in Chapter 4 will facilitate the exploration of the following research question:

Can geophysical and optical characteristics be extrapolated from RADARSAT-1 standard beam microwave backscatter during the melt pond period of spring ablation?

Two methods will be used to investigate this question. First, a direct comparison of point statistics for surface characteristics to RADARSAT-1 σ^0 will be performed over the Melt Pond Study Area. This will be followed by a comparison of the bulk backscatter and surface characteristics derived for the entire study region. The pond onset, pond development, mature ponds and pond drainage stages of the melt pond period developed in Chapter 4 provide a convenient way to explain the progression of the FYI surface and will be used to explicate changes in backscatter during spring ablation.

5.3.3.1. A Comparison of SAR Backscatter to Point Estimate

Surface Characteristics

The comparison of RADARSAT-1 backscatter to point estimates of the optical and physical surface characteristics was performed using aerial flight GPS point data. This allowed for the direct comparison of pond fraction, albedo and backscatter for two paraglider flights and inferred comparison (within one day of data capture) of three additional flights. A list of RADARSAT-1 and paraglider flight comparisons is shown in table 5.2.

Table 5.2. List of RADARSAT-1 data used for the direct comparison of derived surface characteristics through the melt season. The explained variance (R^2) between pond fraction and σ^0 is provided.

RADARSAT-1 YD	Granule	Aerial YD	Tape ID	R^2
169	R134563190	170	t1a	0.0004
171	R134586260	172	t2	0.0048
184	R134778188	185	t8	0.0001
185	R134786260	185	t8	0.0011
191	R134872259	191	t12	0.0063

Over the course of the melt season, the surface of the ablating FYI volume was composed to varying degrees of ponded, transitional and unponded surfaces, as defined in Chapter 3. The value of σ^0 observed during the melt season was a function of the dielectric properties of the representative surfaces within the resolution of the pixel, and in the case of ponded surfaces, of the magnitude and direction of wind induced wave trains. The comparison of RADARSAT-1 σ^0 values to pond fraction and albedo estimates revealed no observable relationship (table

5.2). Four possible reasons exist for this result: noise due to coherent and incoherent wave amplification, the effect of wind on σ^0 , error in estimating surface and volume scattering fractions, and error due to the resolution of the sensor.

Noise estimates for RADARSAT-1 have been established at 1.5dB (see technical specifications on CCRS website). This gives a range of 3dB for each pixel and could explain the low correlation between pond fraction and sigma naught. In order to test for the error in pond fraction estimates due to noise a progressively larger averaging window was applied to the dataset in order to minimize speckle. A 3x3, 5x5 and 7x7 window was applied to the dataset with no significant increase in the observed relationship. This result suggests that the error falls within the resolution of the sensor and is independent of signal noise at 100m.

As discussed in section 5.3.2, there is great variability in σ^0 over ponded surfaces due to the effect of wind. Currently there is no method for correcting for the effect of wind. However, because the comparison of σ^0 to pond fraction was performed for individual flights, the effect of wind should not play a significant role in the observed relationship as the effect of wind is assumed homogeneous across the individual images.

Secondly, surface observations may not have accurately described the scattering characteristics for the different surface types present during the RADARSAT-1 data acquisition. The icescape was partitioned into backscatter

resulting from either surface (ponded) or volume (transitional and unponded) scattering constituents based on surface statistics derived in Chapter 4. Due to the lack of data on the scattering properties of the transitional surface category, the proportion of surfaces that contributed to surface scattering may have been underestimated.

Transitional surfaces were assumed to contribute to the volume scattering component of σ^0 , yet the high concentration of water and shallow depth typical of these surface types suggested that they would have a significant surface scattering term. In order to examine the variability in σ^0 over the unponded surface, an examination of data captured on YD 191 was conducted. The SAR overpass on YD 191 captured the surface shortly after the drainage of melt ponds from the surface. Field and aerial observations estimated only 1% - 2% of the surface was covered by water. Previously, the volume scattering component of ablating bare ice has been assumed constant, around -12dB (Jeffries et al., 1997). However, data captured on YD 191 demonstrates that σ^0 over bare ice has a large degree of variability. The average backscatter observed on YD 191 was -10.595, having a standard deviation of 0.684 and a range of $-12.85 < \sigma^0 < -8.25$. On YD 191, the unponded surface types were represented by transitional blue ice (2%), newly formed bare ice (30%) and mature bare ice (65%). The mature bare ice, having large ice agglomerates and an average depth greater than 5cm, most likely produced the diffuse volume scattering required to account for the lower backscatter values (i.e. < -10 dB). Whereas, the newly formed bare ice (NI) was

characterized by shallow depths which was saturated with melt water. It is expected that NI would constitute a dielectrically rough scattering interface which would produce backscatter in the -8dB to -10dB range. Due to the small percent of transitional surfaces present on YD 191 (2%), it is unknown to what degree transitional surfaces contributed to σ^0 . It is recommended that scatterometer work be conducted over the individual surface types found during spring ablation to resolve uncertainty in the value of σ^0 found over these surfaces.

Finally, error introduced due to the resolution of the sensor may arise from two separate sources: error while registering the appropriate σ^0 value to corresponding pond fraction, and error due to the spatial scale of melt ponds/bare ice patches. The horizontal error for the GPS data was minimized using differential correction from base station data located at the Truro Island Base Camp. This limited horizontal error to 1.5m and 3m for all 14 flights. The positional error value was well within the resolution of the RADARSAT-1 sensor and thus would have little effect on the sampling between GPS point data and SAR backscatter.

At an average flying height of 150m above the surface, the digital camera has a FOV of 273m x 164m. In order to test for error in surface estimates due to the differences in resolution between the aerial photographs and RADARSAT-1, a 3 x 3 averaging window was applied to smooth the RADARSAT-1 data. The relationship between pond fraction and backscatter was equally poor at the 95%

level of confidence for both smoothed and original σ^0 values. As the relationship between pond fraction and σ^0 does not improve when the FOV of both instruments was approximately equal, we can conclude that changes in surface morphology, that is ponded and unponded surfaces, occur on a scale larger than 100m^2 .

Field observations confirm that at a spatial resolution of 100m^2 the surface exhibits considerable heterogeneity in terms of pond size and distribution. A useful measure of the size of melt ponds/bare ice patches is to measure the major and minor axis of a best fit ellipse around their perimeter. During the pond onset stage, both the major/minor axis of melt ponds increased exponentially from $0\text{m}/0\text{m}$ on YD 167 to $43\text{m}/12\text{m}$ on YD 171. This occurred as the surface rapidly transitioned from melt ponds on a funicular snow background to snow patches on a flooded ice background.

Bare ice survived as discrete patches within a flooded background during the pond development and mature pond stages of FYI ablation. The average major and minor axis of bare ice patches during pond development was $21.6\text{m}/6.2\text{m}$ respectively. Over the duration of the mature pond stage, the major and minor axis of average bare ice patches increased to $22.7\text{m}/7.2\text{m}$. During both stages, 5 to 10 patches of variable size were observed within each of the 100m^2 study sites with the size and distribution of the ice patches linked to their proximity to drainage points. A complete description of surface morphology as it related to surface drainage can be found in Chapter 4.

As ponds began to drain, the surface transformed back to melt ponds connected by channels amongst a bare ice background. During the pond drainage stage, the average major and minor axes of melt ponds were 42.1m/17.5m and were found to decrease as melt ponds drained to 1% - 2% of the surface by YD 190.

The size of the melt pond/bare ice patches suggested that both were too small to be resolved in the low resolution RADARSAT-1 data. Thus, the variability in SAR backscatter using a point comparison was independent of melt pond development stage. As a consequence of these results, it is suggested that during the melt pond period, high resolution SAR imagery be used for melt pond estimation. High resolution data has a resolution of 12.5m² which would be able to resolve bare ice patches and melt ponds observed in 2002. Indeed, Yackel and Barber (2000) found that 90.3% of the variability in high resolution SAR σ^0 could be explained by pond fraction and wind velocity using aeri ally derived point surface statistics and high resolution SAR data.

5.3.3.2. A Comparison of Bulk SAR Backscatter to Bulk Surface Characteristics

In the last section, the relationship between pond fraction and σ^0 on a 1:1 scale produced poor results. If the assumption that changes in the surface morphology is at a greater scale than the resolution of the imaging sensor, in our case 100m², it should be possible to filter out this error using bulk values for both

pond fraction and σ^0 , averaged on a sufficiently small scale. To test this assumption the pond fraction and albedo values derived from aerial flights were compared to corresponding σ^0 values averaged over the 3km² Melt Pond Study Area.

Figure 5.7 illustrates the inverse relationship found between pond fraction and σ^0 . In this case the explained variance was low (0.6134). The low correlation was attributed to the effect of wind on the value of σ^0 . Data points 1, 2, and 3 in figure 5.8 appear to overestimate backscatter for the derived pond fraction. Under closer examination, each of these points was captured during moderate wind conditions when values of σ_m were approximately equal to σ_i . Point 1 was captured on YD 181 having a wind speed of 2.0065ms⁻¹, point 2 on YD 183/1.6865ms⁻¹ and point 3 on YD 185/2.0320ms⁻¹. The elimination of these values improved the linear relationship between pond fraction and backscatter to 0.920.

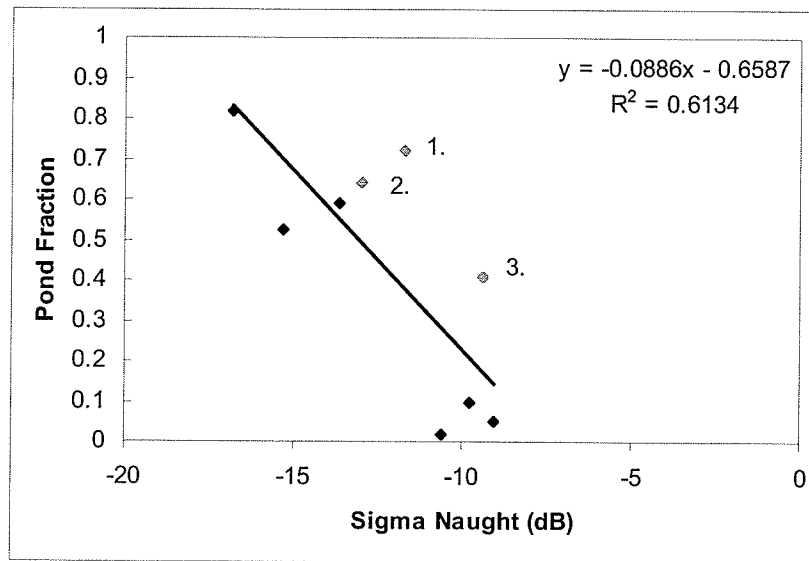


Figure 5.7. Comparison of bulk sigma naught values to pond fraction during the melt pond season. Data points 1, 2, and 3 represent values obtained under moderate wind speeds ($1.6\text{ms}^{-1} - 2.1\text{ms}^{-1}$).

In figure 5.8 the comparison of sigma naught to albedo characteristics over the Melt Pond Study Area revealed a positive relationship. However, the relationship had considerable variability ($r^2 = 0.384$). Again, the misrepresentation of σ^0 captured during moderate wind conditions was observed (points 1, 2 and 3). The explained variance improved to 0.721 when these points were eliminated from the equation.

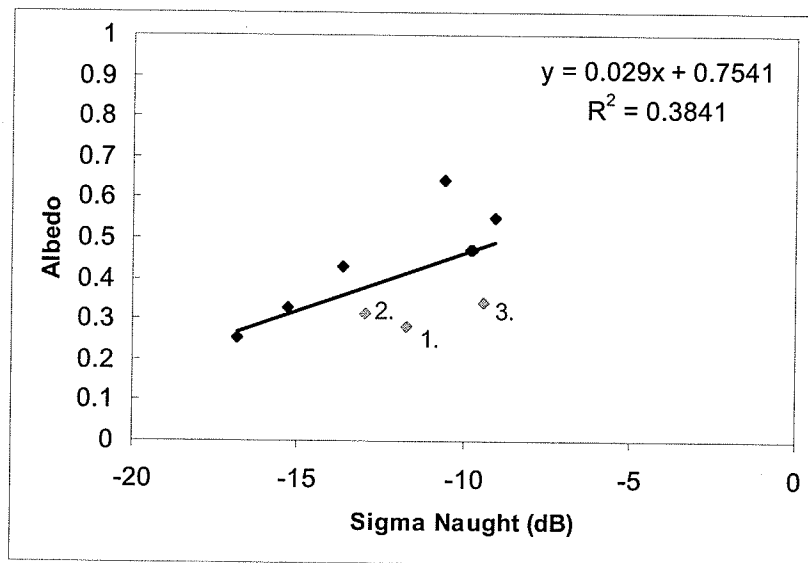


Figure 5.8. A comparison of sigma naught to albedo bulk characteristics during the melt pond season. Increases in backscatter exhibit a positive relationship to surface albedo. Data points 1, 2, and 3 represent values obtained under moderate wind speeds ($1.6\text{ms}^{-1} - 2.1\text{ms}^{-1}$).

In Chapter 4 the relationship between pond fraction and albedo was established using aerial photography. Figure 5.9 shows the strong inverse relationship found between pond fraction and albedo ($r^2 = 0.8861$). A multiple regression analysis was performed to estimate the geophysical state of the surface using the relationships between σ^0 versus pond fraction and albedo respectively. Using these relationships the expected value of σ^0 was found to have an r^2 of 0.658. When data captured on YD 181, 183 and YD 185 was removed, the explained variance improved to 0.888, a value approximately equal to results from Chapter 4.

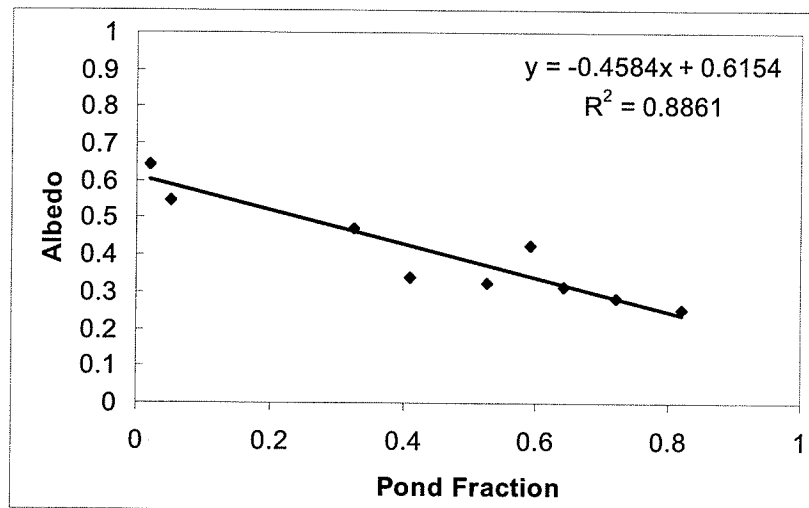


Figure 5.9. The relationship between averaged albedo and pond fraction, derived from surface observation and aerial photography during the melt pond season.

In figure 5.10 the relationship between pond fraction, surface albedo and microwave backscatter is illustrated for the melt pond season. The figure has been segregated into the discrete stages of the melt pond season over first year sea ice. During pond onset (segment a), backscatter drops rapidly as surface water flooded the icescape and the dominant contributor to σ^0 transitioned from volume scattering (σ_v) within the funicular regime to surface scattering (σ_m) over melt ponds. Backscatter was observed to decrease from -9.28dB to -13.85dB during this period, corresponding to an increase in pond fraction from 0% to 59%. Backscatter was expected to decrease through the pond development stage as the fraction of ponded surfaces continued to rise. Pond fraction increased to 85% during pond development, however there was no RADARSAT-1 data for this period (segment b).

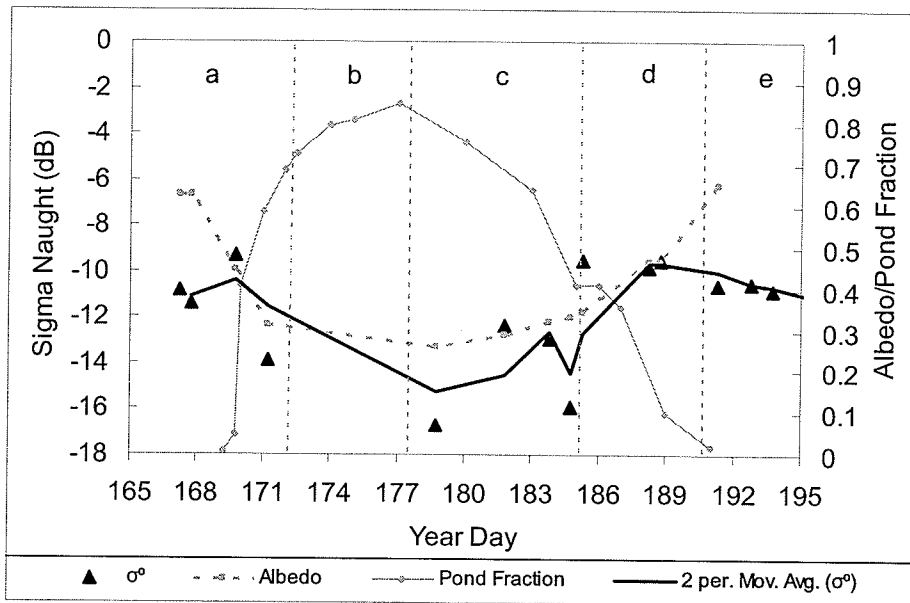


Figure 5.10. A comparison of average backscatter (σ°), albedo and pond fraction found within the Melt Pond Study Area. Notice the inverse relationship between pond fraction and σ° . The graph has been partitioned into pond onset (a), pond development (b), mature pond (c), pond drainage (d) stages of the melt pond season and drained ice (e).

For the mature pond stage, surface drainage was established across the surface and the pond fraction reduced (segment c). Backscatter values increased from -16.83dB on YD 178 to -15.31dB on YD 184, corresponding to the decrease in pond fraction from 85% to 52%. However the data captured on YD 181 (-11.74dB / 72%), YD 183 (-12.98dB / 64%) and YD 185 (-9.42dB / 41%) had moderate wind conditions, which overestimated the value of σ° .

During pond drainage, backscatter rapidly increased with decreasing pond fraction (41% - 1%). Using data captured on YD 191 as a baseline of backscatter obtained for a drained surface (-10.5dB), imagery captured on YD 188 (-9.79dB / 10%) also appeared to have σ° values which were overestimated. Unfortunately

there was no wind data after YD 187. With the removal of surface water over the icescape on YD 190 (segment e), σ^0 enters a stable period having values ranging between -10.5dB to -11.3dB. The surface will continue to have stable σ^0 until either the drained melt ponds become flooded with sea water or the ice begins to breakup and open water becomes a measurable surface feature.

5.4. Conclusions

The objective of this chapter was to examine the usefulness of synthetic aperture radar (SAR) for geophysical inversion of pond fraction and surface albedo during the melt pond stage of spring ablation. The low resolution SAR data was obtained using the RADARSAT-1 satellite platform. RADARSAT-1 captures data over 7 beams. Each beam has a specific range of incidence angle and an Incidence Angle Calibration Model (IACM) for smooth FYI was developed to correct for the effect of incidence angle prior to data analysis. The IACM used a beam specific calibration coefficient (ω) to standardize backscatter (σ^0) values to the near range of the RADARSAT-1 swath (20°).

Applying the IACM to SAR data allowed for the development of a temporal trend as the FYI volume transitioned from winter to spring conditions. When viewed temporally, the trend in σ^0 was shown to contain information on the geophysical state of the surface. The temporal trend revealed the winter, transitional, melt onset and melt pond periods of the FYI lifecycle.

One of the obstacles of working with microwave data for the development of the relationship between backscatter and pond fraction was the sensitivity of σ^0 to changing wind speed across the surface. During periods of moderate wind speed ($1.5\text{ms}^{-1} - 2.5\text{ms}^{-1}$), SAR signatures from melt ponds and bare ice patches were shown to be indistinguishable as the contributions to σ^0 from surface and volume scattering was approximately equal. Moreover the effect of high wind speed on σ^0

was observed to be insignificant when wind direction was orthogonal to the direction of the microwave illumination beam.

The comparison of σ^0 to pond fraction and albedo estimates using point surface statistics from GPS data proved inconclusive. Four possible types of error were suggested for this. First, signal noise was shown to be an insignificant in contributing to error at a resolution of 100m^2 . Secondly, the effect of wind was not taken into consideration. Third, there was a lack of scatterometer field measurements for various types of unponded surface types, especially for transitional surfaces. This limited our understanding of the proportion of surface and volume scattering each of these surface types represented in the overall backscatter observed by the sensor. Lastly, both melt ponds and bare ice patches were on a scale which was too large to be resolved in the low resolution SAR data. The use of high resolution SAR data was recommended for future studies conducted during the melt pond period.

In contrast to point comparisons, the use of bulk surface and microwave statistics averaged over the entire Melt Pond Study Area revealed good results for determining pond fraction and surface albedo when times of moderate wind conditions are removed ($1.5\text{ms}^{-1} - 2.5\text{ms}^{-1}$). The melt pond period of the temporal trend was segmented into the pond onset, pond development, mature pond and pond drainage stages. Backscatter was shown to decrease through the pond onset and pond development stages from -9.28dB to -16.66dB , corresponding to

increases in pond fraction from 0% to 59%. The value of σ° then decreased with the reduction of pond fraction during the pond maturity stage and a backscatter value of -16dB was found to correspond to 52% pond fraction. Finally, a rapid increase in σ° to -10.5dB was the result of complete pond drainage. With the removal of surface water, σ° entered a stable period having σ° values ranging from -10.5dB to -11.3dB.

A negative relationship was found to explain 0.613 of the variability between σ° and pond fraction. Removing data captured during moderate wind conditions improved this relationship to 0.92. In contrast, the comparison of σ° and albedo revealed a positive relationship with an explained variance of 0.384. Again, the elimination of data captured during moderate wind conditions improved the value of r^2 to 0.721. Finally, a multiple regression analysis for the relationship between melt ponds and surface albedo based on σ° values gave an r^2 value of 0.658. This value increased to 0.888 with the removal of data captured during moderate wind conditions. This value was within 0.002 of the relationship found between up-scaled surface observations of albedo to derived melt pond fractions from aerial photography ($r^2 = 0.886$). These results exhibit the importance of establishing appropriate wind conditions and their effect on SAR data.

CHAPTER 6. CONCLUSIONS AND RECOMMENDATIONS

6.1. Conclusions

The first scientific objective which I outlined for this thesis was to understand the geophysical and thermodynamic processes which control optical and microwave scattering during the melt season. The role that FYI plays in cryospheric processes was presented within the context of the geophysical and thermodynamic characteristics of the ocean – sea ice – atmosphere (OSA) interface. The goal was to illustrate the physical constraints which contribute to the overall structure of the FYI volume and to link the interactions acting through the snow, ice and melt pond volumes which comprise the OSA interface. Specific subsections focused on the interactions of solar and microwave energy with the seasonally evolving FY icescape. A review of our current understanding of these processes established a need for a detailed investigation on the physical, optical and microwave characteristics of the FYI volume during spring ablation.

In Chapter 3 I introduced a field experiment conducted over smooth, landfast FYI during spring ablation. The motivation of this chapter was to document the physical, optical and spatial characteristics of the icescape from point observations made within a designated study area. The observations recorded on a sub-daily basis were designed to provide a foundation from which to explore the link between the physical surface and its optical characteristics.

During spring ablation the FYI surface undergoes a transition from a surface dominated by ablating snow to one composed of melt ponds and bare ice. Discrete surface categories of unponded, transitional, and ponded surfaces were developed to help describe this process. Each of these categories was composed of several surface types having distinct physical and optical characteristics.

I found the optical behaviour of the unponded surface category was dependent on the state of the snowpack during melt onset as well as with the level of development of the surface scattering layer over bare ice once the snowpack had ablated. Transitional surfaces were found to exist as a ubiquitous ring surrounding melt ponds and act as a barrier between melt water and the bare ice scattering layer. The transitional category was composed of surfaces which form during the initial stage of FYI surface disintegration. The physical and optical characteristics of the transitional surface category were linked to the degree of crystal disintegration of the exposed FYI volume and the presence of water on the surface. Finally, the ponded surface category was shown to consist of areas of the icescape flooded by melt water. Both the physical and optical characteristics were shown to be strongly influenced by the presence of bubbles trapped within the frazil layer of the FYI volume. Initial bubble density was shown to be high with a correspondingly high surface albedo. Both the albedo and bubble density decreased over time which was attributed to melt pond – albedo feedback mechanism linking bubble release to the ablation of the frazil layer. Further, with

the removal of the frazil layer, albedo was shown to decrease with increasing melt pond depth.

In Chapter 4, I introduced the use of aerial photography captured from a powered paraglider for the up-scaling of point observations of the physical and optical characteristics of the FY icescape. The combination of field measurements and aerial photography allowed for an examination of the spatial distribution of the physical and optical characteristics of the surface at the regional level.

Results from a statistical analysis of the surface morphology and optical albedo illustrated that over the course of the melt pond season both variables are in a constant state of flux. Consistencies between pond fraction and surface albedo revealed that during the melt pond season, the surface transitions through four discrete stages. The pond onset stage was determined by the presence of an isothermal snowpack and melt ponds covering frazil ice. During this period the albedo of unponded surfaces was at its lowest (0.54). The albedo of ponded surfaces was high (0.33) which was attributed to shallow depths and high degree of scattering within the submerged frazil ice layer of the sea ice volume.

The removal of the snowpack exposed the bare ice surface and marked the beginning of the pond development stage. During this time, the aerial fraction of transitional surface types was minimized as the melt pond surface expanded. Pond fraction reached a maximum of 85% at the end of this stage. During this period, the melt pond – albedo feedback was shown to be non-linear and

undergoes its largest change owing to the ablation of the frazil layer along the bottom of melt ponds. The lowest value of albedo occurred over deep melt ponds where the pond bottom interfaced with the columnar FYI volume. Regional albedo values dropped to their lowest level of 0.28 during this period.

The pond development stage transitioned to the mature pond stage of spring ablation with the development of surface drainage. During the mature pond stage the pond fraction was correlated to proximity to drainage sites. The establishment of drainage channels across the icescape stabilized the surface near 50%. The decrease in pond fraction increased regional albedo to 0.32 through this period.

As the temperature gradient through the ice volume approached isothermal, brine drainage channels became active and rapid drainage of the surface occurred through the ice volume. This rapid drainage of the surface determined the start of the pond drainage stage. During pond drainage, transitional surfaces were shown to have a considerable influence on the albedo with aerial fractions of up to 30% during times of rapid drainage. Again, regional albedo was shown to increase to above 0.6 as the melt ponds drained to only 1% – 2% of the surface.

In Chapter 5, I explored the microwave characteristics of the melt season. The objective of this chapter was to examine the usefulness of synthetic aperture radar (SAR) for geophysical inversion of pond fraction and surface albedo during the melt pond stage of spring ablation. The scattering characteristics of SAR were presented in order to satisfy the second scientific objective for this thesis, namely

to construct a link between microwave and optical scattering based on the physical characteristics of the melt surface.

In order to ensure that the RADARSAT-1 data was comparable, an incidence angle correction model (IACM) was developed and applied to each of the 7 standard beam modes used by the sensor. The correction of incidence angle to a single look angle allowed for the development of the temporal trend of SAR signatures. The temporal trend clearly illustrated the seasonal transition of the surface from winter to spring ablation with the melt pond season showing the greatest level of variability in backscatter.

Data captured during the melt pond season also illustrated that the effect of wind has a considerable influence on backscatter (σ^0). Backscatter values become inflated when wind direction was parallel to the SAR illumination beam. The use of SAR signature at wind speed of 1.5ms^{-1} – 2.5ms^{-1} masks the separation of the surface (melt pond) and volume (bare ice) components of σ^0 .

The use of SAR for the determination of point estimates of pond fraction and surface albedo proved inconclusive. As a consequence, bulk morphological, optical and σ^0 statistics for the entire study region were developed in order to examine the relationships between these variables at the regional level (3km^2). With the elimination of wind effected data, SAR backscatter showed a strong negative relationship to pond fraction ($r^2 = 0.92$). In contrast, σ^0 was positively correlated to regional albedo ($r^2 = 0.72$). Finally, a multiple regression analysis

explained 0.888 of the variance found when relating albedo, pond fraction and SAR σ° . These results illustrated that SAR can be used for geophysical inversion at the regional scale, answering the second scientific objective.

6.2. Summary

The results of this research can be summarized into two themes which have contributed in the development of our understanding of the optical and microwave interaction with an actively ablating first year sea ice surface.

- 1) The observation and analyses of the geophysical and optical conditions obtained during the field season are considered to be an evolution of our understanding of the natural conditions existing across an actively ablating smooth first year sea icescape. The statistical comparison of temporal albedo revealed the surface evolved through four stages of melt pond ablation. The main factors contributing to each stage were pond fraction and, the physical and optical properties of the ponded, unponded and transitional surface types. Projecting these variables to the regional scale revealed that the melt pond – albedo feedback is non-linear in nature with the majority of change occurring due to the ablation of the frazil layer in the second stage of melt pond evolution.
- 2) Results from the comparison of the geophysical, optical and microwave characteristics of the melt pond season reinforced our current understanding of these relationships. With regards to the microwave dataset, the development of the Incidence Angle Correction Model (IACM) significantly simplifies the methodology required for the construct temporal trends and comparisons of RADARSAT-1 multi-beam data.

However, three variables were identified as key factors needed to be addressed in order for information derived from SAR data to progress. First, the geophysical characteristics of the surface can only be resolved using high resolution SAR sensors. Secondly, the contribution of transitional surfaces to the surface and volume scattering components of σ^0 need to be quantified. Finally, the effect of wind needs to be modeled for both speed and direction.

The results of this research are limited mainly due to the single sampling year of the dataset. A second sampling season would have allowed for the monitoring of the bubble evolution of melt ponds, the use of high resolution SAR, scatterometer work to quantify backscatter for various surface characteristics, and the refinement of the GPS system used to register aerial photographs to the surface. With the launch of the CASES project in 2003, these limitations are in the process of being addressed.

6.3. Recommendations

This thesis is a first step towards the development of a detailed description of the radiative and microwave properties occurring through the melt pond season over first year sea ice. A better understanding is required of several key variables with regards to the interaction of electromagnetic energy as the surface transitions through the pond onset, pond development, mature ponds and pond drainage stages of the spring ablation period over first year sea ice.

In terms of the optical surface, a detailed examination of the effect of bubbles held within the frazil ice during the early stage of pond onset is required. The focus of this investigation should be on the role that bubble density and pond depth play in determining the degree of the melt pond – albedo feedback. An examination of the role of mechanical weathering on bubble release and pond expansion should be included in this investigation. This knowledge has immediate application for the development of a meaningful representation of the evolution of melt pond albedo over first year sea ice.

Three key factors relating to the SAR data would greatly improve the usefulness of the results. In order to capture the diversity of the physical and optical environment, high resolution SAR data is recommended during the spring ablation period. Surface statistics developed from both field observations and aerial photography illustrated that surface morphology during the melt pond season occurs on a scale greater than that of low resolution SAR data. Secondly,

a relationship is required to correct for the effect of wind over melt ponds. This model should be based on wind velocity and direction. Finally, the contributions of volume and surface scattering to overall backscatter should be investigated using a microwave scatterometer. This investigation should be conducted over transitional and unponded surface types. Each of these recommendations would provide a significantly better understanding of the relationship between backscatter, surface morphology and regional albedo.

REFERENCES

- Barber, David G. 1993. *Assessment of the Interaction of Solar Radiation (0.3 to 3.0 nanometers) with a Seasonally Dynamic Snow Covered Sea Ice Volume, from Microwave (2.0 to 5.0 cm) Scattering*. PhD Thesis, Faculty of Environmental Studies, Earth Observations Laboratory Technical Report Series ISTS-EOL-TR93-002. Department of Geography, University of Waterloo, Ontario.
- Barber, David G. and E. F. LeDrew. 1991. *SAR sea ice discrimination using texture statistics: A multivariate approach*. Photogrammetric Engineering and Remote Sensing. Vol. 57, No. 4, Pages 385-395.
- Barber, David G. and Son V. Nghiem. November 1999. *The role of snow on the thermal dependence of microwave backscattering over sea ice*. Journal of Geophysical Research. Vol 104. No. C11. Pages 25,789 –25,803.
- Barber, D.G., S.P. Reddan and E.F. LeDrew. 1995. *Statistical characterization of the geophysical and electrical properties of snow on landfast first-year sea ice*. Journal of Geophysical Research. Vol. 100, No. C2, 2673-2686.
- Barber, D.G. and A.Thomas. 1998. *The Influence of Cloud on the Radiation Balance, Physical Properties and Microwave Scattering of First Year and Multi-Year Sea Ice*. IEEE Transactions on Geoscience and Remote Sensing. Vol. 36. No. 1. pp. 38-50.
- Barber, D.G. and J.J. Yackel. 1999. *The physical, radiative and microwave scattering characteristics of melt ponds on Arctic landfast sea ice*. International Journal of Remote Sensing. Vol. 20. No. 10. pp. 2069-2090.
- Barber, David G., John J. Yackel and John M. Hanesiak. 1999. *Sea Ice Decay for Marine Navigation: Final Report*. Centre for Earth Observation Science (CEOS). Winnipeg, Manitoba.
- Barber, David G., John J. Yackel and John M. Hanesiak. 2001. *Sea Ice, RADARSAT-1 and Arctic Climate Processes: A Review and Update*. Canadian Journal of Remote Sensing. Vol 27. No 1.
- Barry, R. G. 1996. *The parameterization of surface albedo for sea ice and its snow cover*. Progress in Physical Geography. Vol 20. No 1. pp. 63-79.

- Breneman, Carrie. 2003. *RADARSAT-1 Detection of First Year Sea Ice Melt and Pond Onset in the Central Canadian Archipelago: 1992 to 2001*. Honour Thesis. Department of Geography. University of Calgary.
- Carlström, Anders. 1995. *Modelling Microwave Backscattering from Sea Ice for Synthetic-Aperture Radar Application*. Technical Report No. 271. Chalmers University of Technology. Goteborg, Sweden.
- Colbeck, S.C. 1982. *An overview of the seasonal snow metamorphism*. Reviews of Geophysics and Space Physics. Volume 20. pp. 45-61.
- Curry, Judith A., Julie L. Schramm and Elizabeth E. Ebert. 1995. *Sea Ice – Albedo Climate Feedback Mechanism*. Journal of Climate. Vol. 8. pp. 240-247.
- Curry, J.A., J.L. Schramm, D.K. Perovich and J.O. Pinto. 2001. *Applications of SHEBA/FIRE data to evaluation of snow/ice albedo parameterizations*. Journal of Geophysical Research. Vol. 106. No. D14. pp. 15,345-15,355.
- DeAbreu, Roger, David G. Barber, Kevin Misurak and E.F. LeDrew. 1994. *Spectral albedo of snow-covered first-year and multi-year sea ice during spring melt*. Annals of Glaciology. Vol. 21. pp. 337–342.
- Derksen, C., J. Piwowar and E. LeDrew, 1997. *The Evolution of Arctic Sea Ice Melt Pond Fraction as Determined from Low Level Aerial Photographs*. Arctic and Alpine Research. Vol. 24. No. 3. pp. 345-351.
- Drinkwater, Mark and G.B. Crocker. 1988. *Modelling changes in the dielectric and scattering properties of young snow-covered sea ice at GHz frequencies*. Journal of Glaciology, Vol. 34, No. 118. 274-282.
- Drobot, S.D. 1997. *Microwave Radiometry and Snow Water Equivalence Retrievals on Snow Covered Sea Ice in the Marine Cryosphere*. Thesis. Department of Geography. University of Manitoba.
- Eicken, Hajo. 2003. *From the microscopic to the macroscopic to the regional scale: Growth, microstructure and properties of sea ice*. Sea Ice – An introduction to its physics, biology, chemistry and geology. Eds: Thomas D. and G.S. Dieckmann. Blackwell Science. London.
- Eicken, Hajo and Peter Lemke. 2001. *The response of polar sea ice to climate variability and change*. In: Climate of the 21st century: Changes and risks. Editors: Lozan, Jose L., Hartmut Grassl and Peter Hupfer. GEO, Hamburg, Germany. pp. 206-211.

- Eicken, H., H.R. Krouse and D.K. Perovich. 2002. *Tracer studies of pathways and rates of meltwater transport through Arctic summer sea ice*. Journal of Geophysical Research. Vol. 107. No. C10. pp. SHE 22-1 – SHE 22-20.
- Falkingham, John C. 2000. *Sea Ice in the Canadian Arctic in the 21st Century*. Internal Report. Canadian Ice Service.
- Fetterer, Florence and Norbert Untersteiner. 1998. *Observations of melt ponds on Arctic sea ice*. Journal of Geophysical Research. Vol. 103. No. C11. pp. 24,821-24,835.
- Fukusako, S. 1990. *Thermophysical properties of ice, snow and sea ice*. International Journal of Thermophysics. Vol 11. pp. 353-372.
- Grenfell, T.C. 1991. *A radiative transfer model for sea ice with vertical structure variations*. Journal of Geophysical Research. Vol. 96. No. C9. pp. 16991-17001.
- Grenfell, Thomas, C. David G. Barber, A. K. Fung, Anthony J. Gow, Kenneth C. Jezek, E. J. Knapp, Son V. Nghiem, Robert G. Onstott, Donald K. Perovich, Collin S. Roesler, C. T. Swift, and F. Tanis. September 1998. *Evolution of Electromagnetic Signatures of Sea Ice from Initial Formation to the Establishment of Thick First – Year Ice*. Geoscience and Remote Sensing. Vol. 36. Number 5. Part II. IEEE Periodicals. NJ. Pages 1642-1654.
- Grenfell, T.C., D.J. Cavalieri, J.O. Comiso, M.R. Drinkwater, R.G. Onstott, I. Rubinstein, K. Steffen and D.P. Winebrenner. 1992. *Considerations for microwave remote sensing of thin sea ice*. Microwave Remote Sensing of Sea Ice. Edit. F.D. Carsey. Geophysical Monograph 68. American Geophysical Union. Washington D.C. pp. 291-301.
- Grenfell, T. C. and G.A. Maykut. 1977. *The optical properties of ice and snow in the Arctic Basin*. Journal of Glaciology. Vol. 18. No 30. pp. 445-463.
- Grenfell, T.C., and D. K. Perovich. 2004. *Seasonal and spatial evolution of albedo in a snow- ice-land-ocean environment*. Journal of Geophysical Research. Vol. 109, C01001. Pages 1029 – 1039.
- Grenfell, T.C. and D.K. Perovich. 1984. *Spectral Albedo of Sea Ice and Incident Solar Irradiance in the Southern Beaufort Sea*. Journal of Geophysical Research. Vol. 89. No. C3. pp. 3573-3580.
- Grenfell, T.C., S.G. Warren and P.C. Mullen. 1994. *Reflection of solar radiation by the Antarctic snow surface at ultraviolet, visible, and near-infrared wavelengths*. Journal of Geophysical Research. Vol 99. No. D9. pp. 18699-18683.

- Hanesiak, John M. 2001. *Development of a One-Dimensional Electro-Thermophysical Model of the Snow Sea-Ice System: Arctic Climate Processes and Microwave Remote Sensing Applications*. Thesis. Department of Geography. University of Manitoba.
- Hanesiak, J.M, D. G., Barber, R. De Abreu and J.J. Yackel. 2001a. *Local and regional albedo. Observations of arctic first-year sea ice during melt ponding*. Journal of Geophysical Research-Oceans. Vol. 106. No. C1. pp. 1005-1016
- Hanesiak, J.M., D.G. Barber, and G.M. Flato. 1999. *The role of diurnal processes in the seasonal evolution of sea ice and its snow cover*. Journal of Geophysical Research. Vol. 104. pp.13593 - 13604.
- Hanesiak, J.M, D. G., Barber and J.J. Yackel. 2001b. *Effect of Melt Ponds on First Year Sea Ice Ablation – Integration of RADARSAT-1 and Thermodynamic Modeling*. Canadian Journal of Remote Sensing. Vol. 27. No. 5. pp. 433-442.
- Henderson, Floyd M. and Anthony Lewis. 1999. *Principles and Application of Imaging Radar: Manual of Remote Sensing 3rd Edition*. Volume 2. John Wiley & Sons, Inc. Toronto.
- Iacozza, John. 1997. *Models of Snow Distribution Pattern for Various Types of Sea Ice in the Canadian High Arctic*. Thesis. Department of Geography. University of Manitoba.
- Iacozza, John and David Barber. 2001. *Ablation patterns of snow cover over smooth first-year sea ice in the Canadian Arctic*. Hydrological Processes. Vol. 15. Pages 3359-3569.
- Iacozza, John and David Barber. 1999. *Modeling the Distribution of Snow on Sea Ice Using Variograms* Atmosphere-Oceans. Vol. 37. Pages 21-51.
- IPCC (Intergovernmental Panel on Climate Change), 2001. *Climate Change: The Scientific Basis*.
- Folland, C.K., T.R. Karl, J.R. Christy, R.A. Clarke, G.V. Gruza, J. Jouzel, M.E. Mann, J. Oerlemans, M.J. Salinger and S.-W. Wang. 2001. *Observed Climate Variability and Change*. In: *Climate Change 2001: The Scientific Basis. Contribution of Working Group I to the Third Assessment Report of the Intergovernmental Panel on Climate Change* [Houghton, J.T., Y. Ding, D.J. Griggs, M. Noguer, P.J. van der Linden, X. Dai, K. Maskell, and C.A. Johnson (eds.)]. Cambridge University Press, Cambridge, United Kingdom and New York, NY, USA, 881pp.

- Jeffries, M.O., K. Schwartz and S. Li. 1997. *Arctic summer sea-ice SAR signatures, melt-season characteristics, and melt-pond fractions*. Polar Record. Vol. 33. No. 185. pp. 101-112.
- Jezeq, Kenneth C., Donald K. Perovich, K. M. Golden, Charles Luther, David G. Barber, Prasad Gogineni, Thomas C. Grenfell, Arthur K. Jordan, Curtis D. Mobley, Son V. Nghiem and Robert G. Onstott. September 1998. *A Broad Spectral, Interdisciplinary Investigation of the Electromagnetic Properties of Sea Ice*. Geoscience and Remote Sensing. Vol. 36. Number 5. Part II. IEEE Periodicals. NJ.
- Jordan, R.E. 1991. *A one-dimensional temperature model for a snow cover: Technical documentation for SN THERM89*. US Army Core of Engineers, Cold Regions Research and Engineering Laboratory. CRREL Report No. 91-16.
- Kirk, Robert B. 2001. *On the Use of Synthetic aperture RADAR for Detecting the Onset of Melt Over Landfast First Year Sea Ice*. Thesis. Department of Geography. University of Calgary.
- Kwok, Ronald, Son V. Nghiem, S. Martin, D.P. Winebrenner, Anthony J Gow, Donald K. Perovich, C. T. Swift, David G. Barber, K. M. Golden and E. J. Knapp. September 1998. *Laboratory Measurements of Sea Ice: Connections to Microwave Remote Sensing*. Geoscience and Remote Sensing. Vol. 36. Number 5. Part II. IEEE Periodicals. NJ.
- Langham, E.J. 1981. *Physics and properties of snow cover*. Handbook of snow. Pergamon Press Canada Ltd. Willowdale, Ontario. pp.275-337. Editors: D.M. Gray and D.H. Male.
- Lee, Yun Hee and Jay Kyoong Lee. 1995. *Theoretical models for active and passive remote sensing of sea ice*. IGARSS 1995. Quantitative Remote Sensing for Science and Applications. Volume 1.
- LeDrew, E.F., D.G. Barber, T. Agnew and D. Dunlop. 1992. *Canadian Sea Ice Atlas from Microwave Remotely Sensed Imagery: July 1987 to June 1990*. Climatological Studies Number 44, p 80.
- Lindsay, R. W. 2001. *Assimilation of ice thickness information into a sea ice model*. Proceedings of the Sixth Conference on Polar Meteorology and Oceanography, Amer. Meteorol. Soc., 15-20 January 1999, San Diego CA, 219-222.

- Livingston, C.E., R.G. Onstott, L.D. Arsenault, A.L. Gray, and K.P. Singh. 1987. *Microwave sea-ice signatures near the onset of melt*. IEEE Transactions on Geoscience and Remote Sensing. GE-25, 174-187. IEEE Periodicals. NJ.
- Malmgren, F. 1927. *On the properties of sea-ice. Norweg. North Pole Expedition. "Maud". 1918-1925. Vol. 1. No. 5. pp. 1-67.*
- Mätzler, Christian. 1987. *Applications of the Interaction of Microwaves with the Natural Snow Cover*. Remote Sensing Reviews. Vol.2, pages 259-3878.
- Mätzler, Christian. 1996. *Autocorrelation functions of granular media with free arrangement of spheres, spherical shells and ellipsoids*. Journal of Applied Physics. Vol. 81, No. 3, Pager 1509-1517.
- Mätzler, Christian. 2002. *Relation Between Grain Size and Correlation Length of Snow*. Session C04 Cryosphere. AGU Fall Meeting. San Francisco, CA.
- Mätzler, C., H. Aebischer and E. Schanda. 1984. *Microwave Dielectric Properties of Surface Snow*. IEEE Journal of Oceanic Engineering. Vol. OE-9, No. 5. Pages 366-371.
- Maykut, G.A. and T.C. Grenfell. 2001. *Experimental and Theoretical Studies of Ice – Albedo Feedback Processes in the Arctic Basin*. SHEBA Phase II Data Report.
- Mundy, C.J. and D.G. Barber (eds.) *C-ICE 2002 Data Report*. CEOS-Tech-03-01.
- Nghiem, S.V. and C. Bertoia. 2001. *Study of multi-polarization C-band backscatter signatures for Arctic sea ice mapping with future satellite SAR*. Canadian Journal of Remote Sensing. Vol. 25, No. 5, Pages 387-402.
- Nghiem, S.V., R. Kwok, J.A. Kong and R.Y. Shin. 1993. *A model with ellipsoidal scatterers for polarimetric remote sensing of anisotropic layered media*. Radio Science. Vol. 28, No. 5, Pages 687-703.
- Nghiem, S.V., R. Kwok, J.A. Kong, R.Y. Shin, S.A. Arcone and A.J. Gow. 1996. *An electrothermodynamic model with distributed properties for effective permittivities of sea ice*. Radio Science. Vol. 31, No. 2, Pages 297-311.
- Nghiem, S.V., R. Kwok, S.H. Yueh and M.R. Drinkwater. 1995. *Polarimetric signatures of sea ice: 1. Theoretical model*. Journal of Geophysical Research. Vol. 100, No. C7, Pages 13665-13679.

- Onstott, Robert G. 1992. *SAR and Scatterometer Signatures of Sea Ice. Microwave Remote Sensing of Sea Ice*. Frank D. Carsey Editor. American Geophysical Union. Washington, DC. 73-104.
- Onstott, R.G. and S. Gogineni. 1985. *Active microwave measurements of Arctic sea ice under summer conditions*. Journal of Geophysical Research. Vol. 90. pp. 5035-5044.
- Papakyriakou, T.N. 1999. *An Examination of Relationships among the Energy Balance, Surface Properties and Climate over Snow-Covered Sea Ice during the Spring Season*. PhD. Thesis, Geography Department. University of Waterloo.
- Papakyriakou, T.N. 2003. *Micrometeorological Data*. C-ICE 2002 Data Report. Mundy, C.J. and D.G. Barber (eds.). University of Manitoba. CEOS-Tech-03-01.
- Parkinson, C.L., D.J. Cavalieri, P. Gloersen, H.J. Zwally and J.C. Comiso 1999. *Arctic sea ice extents, areas and trends, 1978 – 1996*. Journal of Geophysical Research 104: 20, 837-20,856.
- Perovich, D.K. 1996. *The optical properties of sea ice*. Monograph 96-1. US Army Corps of Engineers. Cold Regions Research and Engineering Laboratory.
- Perovich, D.K., T.C. Grenfell, b. Light and P.V. Hobbs. 2002. *Seasonal evolution of the albedo of multiyear Arctic sea ice*. Journal of Geophysical Research. Vol. 107. No. C10. pp. SHE 20-1 – SHE 20-13.
- Perovich, D.K., J.A. Richter-Menge and W.B. Tucker III. 2001. *Seasonal changes in sea ice morphology*. Annals of Glaciology. Vol 33. pp. 171-176.
- Perovich, D.K., W.B. Tucker III. and K.A. Ligett. 2002. *Aerial observations of the evolution of ice surface conditions during summer*. Journal of Geophysical Research. Vol. 107. No C10. pp. SHE 24-1 – SHE 24-14.
- Rothrock, D.A., Y. Yo and G.A. Mayhut, 1999. *Thinning of the Arctic sea ice cover*. Geophysical Research Letters. 26: 3469-3472.
- Sedlacek, Jan. 2001. *An albedo parameterization for sea ice models*. Thesis. Department of Earth Science. Swiss Federal Institute of Technology. Zurich, Switzerland.

- Shine, K.P. and A. Henderson-Sellers. 1985. *The Sensitivity of a Thermodynamic Sea Ice Model to Changes in Surface Albedo Parameterization*. Journal of Geophysical Research. Vol 90. NO. D1. pp. 2243 – 2250.
- Stiles, William H. and Fawwaz Ulaby. 1980. *The Active and Passive Microwave Response to Snow Parameters: 1. Wetness*. Journal of Geophysical Research. Vol. 85. No. C2. Pages 1037-1044.
- Tiuri, M.E., A.H. Sihvola, E.G. Nyfors and M.T. Hallikainen. 1984. *The Complex Dielectric Constant of Snow at Microwave Frequencies*. IEEE Journal of Oceanic Engineering OE-9 No. 5. Pages 377-382.
- Tucker, W.B. III, D. K. Perovich, A. J. Gow, W. F. Weeks, M. R. Drinkwater 1992. *Physical Properties of Sea Ice Relevant to Remote Sensing: Microwave Remote Sensing of Sea Ice*. Frank D. Carsey Editor. American Geophysical Union. Washington D.C.
- Ulaby, F. T., R. K. Moore, and A. K. Fung. 1986. *Microwave Remote Sensing – Active and Passive, Vol. III: From Theory to Applications*. Artech House. Dedham, Massachusetts.
- Vant, M.R., R.O. Ramseier and V. Makios. 1986. *The complex dielectric constant of sea ice at frequencies in the range 0.1 to 40 GHz*. Journal of Applied Physics. Volume 49, Number 3, pp 1264 –1280.
- Warren, Stephen G. 1982. *Optical Properties of Snow*. Reviews of Geophysics and Space Physics. Vol. 20. No. 1. pp. 67 – 89.
- Weeks, W.F., and S.F. Ackley. 1986. *The growth, structure and properties of sea ice*. The Geophysics of Sea Ice. Edited by N. Untersteiner, pp. 9-164. NATO ASI Series B: Physics vol. 146. Plenum Press, New York.
- Wiscombe, W.J. and S.G. Warren. 1980. *A model for the spectral albedo of snow: 1. Pure snow*. Journal of Atmospheric Science. Vol. 37. pp. 2712-2733.
- Yackel, John J. 2001. *On the Use of Synthetic aperture RADAR (SAR) for Estimating the Thermodynamic Evolution of Snow Covered First Year Sea Ice*. Ph.D. dissertation, Faculty of Graduate Studies. Centre for Earth Observation Studies, Department of Geography, University of Manitoba.
- Yackel, John J. and D.G. Barber. September 2000. *Melt ponds on sea ice in the Canadian Archipelago 2. On the use of RADARSAT-1 synthetic aperture RADAR for geophysical inversion*. Journal of Geophysical Research. Vol. 105, No. C9, Pages 22,061 – 22,070.

Yackel, John J., D.G. Barber and J.M. Hanesiak. 2000. *Melt ponds on sea ice in the Canadian Archipelago: 1. Variability in morphological and radiative properties*. Journal of Geophysical Research. Vol. 105 No. C9. pp 22,049-22,060.

APPENDIX A. YEAR DAY CONVERSION

Table A.1. Year day conversion table.

Day	JAN	FEB	MAR	APR	MAY	JUN	JUL	AUG	SEP	OCT	NOV	DEC	DAY
1	1	32	60	91	121	152	182	213	244	274	305	335	1
2	2	33	61	92	122	153	183	214	245	275	306	336	2
3	3	34	62	93	123	154	184	215	246	276	307	337	3
4	4	35	63	94	124	155	185	216	247	277	308	338	4
5	5	36	64	95	125	156	186	217	248	278	309	339	5
6	6	37	65	96	126	157	187	218	249	279	310	340	6
7	7	38	66	97	127	158	188	219	250	280	311	341	7
8	8	39	67	98	128	159	189	220	251	281	312	342	8
9	9	40	68	99	129	160	190	221	252	282	313	343	9
10	10	41	69	100	130	161	191	222	253	283	314	344	10
11	11	42	70	101	131	162	192	223	254	284	315	345	11
12	12	43	71	102	132	163	193	224	255	285	316	346	12
13	13	44	72	103	133	164	194	225	256	286	317	347	13
14	14	45	73	104	134	165	195	226	257	287	318	348	14
15	15	46	74	105	135	166	196	227	258	288	319	349	15
16	16	47	75	106	136	167	197	228	259	289	320	350	16
17	17	48	76	107	137	168	198	229	260	290	321	351	17
18	18	49	77	108	138	169	199	230	261	291	322	352	18
19	19	50	78	109	139	170	200	231	262	292	323	353	19
20	20	51	79	110	140	171	201	232	263	293	324	354	20
21	21	52	80	111	141	172	202	233	264	294	325	355	21
22	22	53	81	112	142	173	203	234	265	295	326	356	22
23	23	54	82	113	143	174	204	235	266	296	327	357	23
24	24	55	83	114	144	175	205	236	267	297	328	358	24
25	25	56	84	115	145	176	206	237	268	298	329	359	25
26	26	57	85	116	146	177	207	238	269	299	330	360	26
27	27	58	86	117	147	178	208	239	270	300	331	361	27
28	28	59	87	118	148	179	209	240	271	301	332	362	28
29	29		88	119	149	180	210	241	272	302	333	363	29
30	30		89	120	150	181	211	242	273	303	334	364	30
31	31		90		151		212	243		304		365	31
Day	JAN	FEB	MAR	APR	MAY	JUN	JUL	AUG	SEP	OCT	NOV	DEC	DAY

APPENDIX B. MELT POND STUDY SCHEDULE

Table B.1. List of location and times for the Melt Pond Study Site.

Grid Cell	Y	X	Session	Day	Time (sched)	Time (arr)	Notes
n/a	75.244833	-97.15383	n/a	n/a	n/a	n/a	Base Camp Coordinate
n/a	75.256495	-97.426851	n/a	n/a	n/a	n/a	NW Grid Corner
n/a	75.256591	-97.321332	n/a	n/a	n/a	n/a	NE Grid Corner
n/a	75.229630	-97.426379	n/a	n/a	n/a	n/a	SW Grid Corner
n/a	75.229726	-97.321054	n/a	n/a	n/a	n/a	SE Grid Corner
n/a	75.256543	-97.374091	n/a	n/a	n/a	n/a	North RD. 1.5km
n/a	75.243158	-97.321193	n/a	n/a	n/a	n/a	East Rd. 1.5 km
n/a	75.244258	-97.354651	168-a	17/Jun	700	800	
n/a	74.237567	-97.35715	169-a	18/Jun	900	900	
n/a	75.244830	-97.348620	170-a	19/Jun	600	838	
825	75.244510	-97.348810	170-b	19/Jun	1800	1905	
729	75.238690	-97.345950	171-a	20/Jun	600	937	
195	75.246240	-97.393670	171-b	20/Jun	1600	1730	
558	75.248640	-97.351110	172-a	21/Jun	600	745	
115	75.255130	-97.404740	172-b	21/Jun	1300	1420	
191	75.250310	-97.378520	172-c	21/Jun	2100	2200	
621	75.25	-97.35	173-a	22/Jun	700	830	
244	75.233330	-97.388600	173-b	22/Jun	1600	1600	
848	75.240000	-97.317320	174-a	23/Jun	1400	1515	
502	75.251950	-97.363070	174-b	23/Jun	2100	2205	
25	75.254840	-97.415410	175-a	24/Jun	1000	1330	
587	75.247960	-97.348580	176-a	25/Jun	0	125	
748	75.246970	-97.311300	176-b	25/Jun	800	935	
795	75.246180	-97.324260	176-c	25/Jun	2300	2330	
433	75.243310	-97.364650	177-a	26/Jun	1000	1230	
333	75.234850	-97.377240	177-b	26/Jun	2300	30 (jd178)	
n/a	n/a	n/a	178-a	27/Jun	1300	n/a	Missed rain
781	75.232860	-97.324600	178-b	27/Jun	2100	2100	
n/a	n/a	n/a	179-a	28/Jun	1500	n/a	Missed (heavy fog)
n/a	n/a	n/a	180-a	29/Jun	1400	n/a	Missed (steady rain/flight

							staging)
Grid Cell	Y	X	Session	Day	Time (sched)	Time (arr)	Notes
353	75.253510	-97.377180	180-b	29/Jun	2100	2100	
48	75.248950	-97.410570	181-a	30/Jun	800	1045	
437	75.247900	-97.365900	181-b	30/Jun	1900	2050	
280	75.241580	-97.385360	182-a	01/Jul	600	815	
613	75.244390	-97.344890	182-b	01/Jul	1600	1750	Cancelled (bear in area)
175	n/a	n/a	183-a	02/Jul	100		Missed (thick fog)
611	75.242460	-97.349250	183-b	02/Jul	1000	1250	
223	75.244430	-97.384340	183-c	02/Jul	2100	2150	
12	75.244060	-97.414840	184-a	03/Jul	1200	1310	
748	75.257390	-97.331160	184-b	03/Jul	2100	2130	
306	75.238020	-97.377250	185-a	04/Jul	700	830	
863	75.253660	-97.316640	185-b	04/Jul	2000	2115	
587	75.247960	-97.348170	186-a	05/Jul	800	1130	
301	75.232660	-97.381190	187-a	06/Jul	200	310	
410	75.250810	-97.369820	187-b	06/Jul	1100	1220	
429	75.24	-97.36	187-c	06/Jul	1900	2215	
31	75.232440	-97.412510	188-a	07/Jul	200	420	
619	n/a	n/a	188-b	07/Jul	1500		Missed (steady rain, camp logistics)
712	n/a	n/a	188-c	07/Jul	2300		Missed (steady rain)
296	75.255690	-97.382730	189-a	08/Jul	1300	1430	

All coordinates in decimal degrees - NAD 27 Datum, True North Ref
Grid Cell - refers to randomly-scheduled grid cell

APPENDIX C. PROGRAMS USED WITH AERIAL PHOTOGRAPHY

Spectral.pro – IDL program used to integrate binary spectral albedo (ASD) to segmented albedo normalized to incident irradiance.

```
; program to calculate F albedo

SP = fltarr(1, 430) ; incident irradiance values interpolated
                      linear for study
openr, 1, 'solar_950.txt'
readf, 1, SP

SN = fltarr(1,430) ; band width (1.4nm) range 338nm - 950nm
openr, 2, 'spectral.txt'
readf, 2, SN

ASD = fltarr(15,430) ; asd albedo
openr, 3, 'asd.txt' ; file containing 15 surface type albedos
readf, 3, ASD

openw, 4, 'solar_final.txt' ;write integrated albedos

VIS = where(SN ge 379.5 and SN le 740.5)
PAR = where(SN ge 399 and SN le 700.5)
NIR = where(SN ge 699.5 and SN le 951)
BLU = where(SN ge 399.5 and SN le 500.5)

SINT = int_tabulated(SN(0,*), SP(0,*))
SVIS = int_tabulated(SN(0,VIS), SP(0,VIS))
SPAR = int_tabulated(SN(0,PAR), SP(0,PAR))
SNIR = int_tabulated(SN(0,NIR), SP(0,NIR))
SBLU = int_tabulated(SN(0,BLU), SP(0,BLU))

for i=0,14 do begin

FA = ASD(i,*) * SP(0,*) ;solar albedo

INT = int_tabulated(SN(0,*), FA(0,*))
IVIS = int_tabulated(SN(0,VIS), FA(0,VIS))
IPAR = int_tabulated(SN(0,PAR), FA(0,PAR))
INIR = int_tabulated(SN(0,NIR), FA(0,NIR))
IBLU = int_tabulated(SN(0,BLU), FA(0,BLU))

TINT = INT/SINT
TVIS = IVIS/SVIS
TPAR = IPAR/SPAR
TNIR = INIR/SNIR
TBLU = IBLU/SBLU

printf, 4, TINT, TVIS, TPAR, TNIR, TBLU, format= '(5f10.6)'

endfor

free_lun, 1,2,3,4

end
```

Rename.sh – unix shell to rename frame captures to flight specific ID.

```
#program assume file id from BTV frame capture (Tlapse_###.tif)
#program requires list of numbers for extension (Number.txt).
#csh

foreach loop (`cat Number.txt`)
echo $loop
ls -d T*{$loop}.tif
mv T*{$loop}.tif Flight_ID_{$loop}.tif
end
```

Cut_image.pro – IDL program to clip black vertical lines from image border.

```
X = 612
Y = 480
XY = 293280
File_Len = 391; specific to each flight

tmp = BytArr(640,480)

num = '000'
openr, lun, 'numbers.txt' /get_lun

name = 'Flight_ID_'
name_re = 'Cflight_ID_'

For i=0,File_Len-1 Do Begin
  readf, lun, num
  print, name+num+'.tif'
  infile = name+num+'.tif'
  infile_re = name_re+num+'.tif'

  tmp = read_tiff(infile)
  tmp_re = tmp(19:630,0:479)
  write_tiff, infile_re, tmp_re, 1
Endfor

END
```

Median_shift.pro – IDL program to calculate flight global median and shift image median to global value. This program will also shift to mean values. Simply deactivate the “md” and activate “avg” variables. This program has been adapted from code created by Phillip Hwang at the Centre for Earth Observation Science.

```
X = 612
Y = 480
XY = 293760
File_Len = 474
MAXDN = BytArr(File_Len)
MINDN = BytArr(File_Len)
AVGDN = BytArr(File_Len)
MEDDN = BytArr(File_Len)
SUM_MAX = 0.
SUM_MIN = 0.
SUM_AVG = 0.
SUM_MED = 0.
```

```

data_new = LonArr(XY)
shift_mean = 0.
kk = 0LL

tmp = BytArr(X,Y)

num = '000'
openr, 1, 'list.txt'
; openw, 2, 'AVG_out.txt' ; AVG
openw, 2, 'md_t8_out.txt' ;MED

name = 'ctape8_'
; name_re = 'mn_t8_' ; AVG
name_re = 'md_t8_' ; MED

For i=0,File_Len-1 Do Begin
  readf, 1, num
  infile = name+num+'.tif'
  infile_re = name_re+num+'.tif'
  tmp = read_tiff(infile)
  data = reform(tmp,[XY])
  MAXDN(i) = max(data)
  MINDN(i) = min(data)
  AVGDN(i) = mean(data)
  MEDDN(i) = median(data)
  SUM_MAX = SUM_MAX + MAXDN(i)
  SUM_MIN = SUM_MIN + MINDN(i)
  SUM_AVG = SUM_AVG + AVGDN(i)
  SUM_MED = SUM_MED + MEDDN(i)

  print, num, MAXDN(i), MINDN(i), AVGDN(i), MEDDN(i)
;  printf, 2, num, MAXDN(i), MINDN(i), AVGDN(i), MEDDN(i)

Endfor

close, 1
openr, 1, 'list.txt'

G_MAX = uint(SUM_MAX/File_Len)
G_MIN = uint(SUM_MIN/File_Len)
G_AVG = uint(SUM_AVG/File_Len)
G_MED = uint(SUM_MED/File_Len)

print, G_MAX, G_MIN, G_AVG, G_MED
printf, 2, G_MAX, G_MIN, G_AVG, G_MED

For i=0,File_Len-1 Do Begin

  readf, 1, num
  print, name+num+'.tif'
  infile = name+num+'.tif'
  infile_re = name_re+num+'.tif'
  tmp = read_tiff(infile)
  data = reform(tmp,[XY])
;  shift_mean = float(G_AVG) - float(AVGDN(i)) ; AVG
  shift_mean = float(G_MED) - float(MEDDN(i)) ; MED
  data_new = shift_mean + data
  tmp_re = reform(data_new,[X,Y])

  For ki=0, X-1 Do Begin
    For kj=0, Y-1 Do Begin
      If (tmp_re(ki,kj) gt 255.) Then tmp_re(ki,kj) = 255.
      If (tmp_re(ki,kj) lt 0.) Then tmp_re(ki,kj) = 0.
    Endfor
  Endfor
Endfor

```

```

    data_re = reform(tmp_re,[XY])
; if min(data_new) lt 0 or max(data_new) gt 255 Then Begin
;   tv, tmp_re
;   print, num, i, MAXDN(i), MINDN(i), AVGDN(i)
;   print, G_MAX, G_MIN, G_AVG
;   print, min(data_new), max(data_new)
;   print, min(data_re), max(data_re)
;   read, xx
;   endif

    printf, 2, num, MINDN(i), MAXDN(i), AVGDN(i), MEDDN(i), min(data_re), max(data_re), mean(data_re), median(data_re)
    write_tiff, infile_re, tmp_re, 1

Endfor

close, 1
close, 2

END

```

Loop_tv.pro – this program allows users to observe a raw image and associated clustered image, cluster statistics and image histogram. When asked, insert (image number – 1) and last image. For example: 321 345 – the program shows images 320 through 344 with a 5 second interval between images. This program has been adapted from code created by Phillip Hwang at the Centre for Earth Observation Science.

```

; program for counting stats on isocluster image (6 clusters)
; X: 612, Y: 480

; Make Color Map for Classification
; White:1, Yellow:2, Blue:3, Red:4, Green:5, grey:6, orange:7, black:8)
R = [255, 255, 0, 255, 0, 100, 200, 0]
G = [255, 255, 0, 0, 255, 100, 100, 0]
B = [255, 0, 255, 0, 0, 100, 50, 0]

X = 612
Y = 480
XY = 293760
read, 'input number ', File_Str, File_Len
; File_Str = 1
; File_Len = 999

tmp = BytArr(612,480)
tmp_re = BytArr(612,480)
DN = BytArr(XY,File_Len)
HT = LonArr(256,File_Len)
TOTHT = LonARR(256)
CAT = BytArr(File_Len)
MAXDN = BytArr(File_Len)
MINDN = BytArr(File_Len)
MEANDN = BytArr(File_Len)
CUM_HIST = LonArr(256,100,6)
FN = StrArr(File_Len)

num = '000'
tmp_cat = '00'
openr, lun, 'list.txt', /Get_Lun

if File_Str ne 0 Then Begin
  For jj = 0, File_Str-1 Do Begin
    readf, lun, num
  Endfor

```

```

Endif

name = 'mn_t8_' ; Original
name_re = 'iso8_mn_t8_' ; Classification

Openw, lun1, 'log.txt', /Get_lun
Openw, lun2, 'tv_scrapes.txt', /Get_lun

for i=File_Str,File_Len-1 Do Begin
readf, lun, num

FN(i) = num

infile = name+num+'.tif'
infile_re = name_re+num+'.tif'

tmp = read_tiff(infile)
tmp_re = read_tiff(infile_re)

MAX01 = where(tmp_re eq 1, count) ; if class 1
MAX02 = where(tmp_re eq 2, count)
MAX03 = where(tmp_re eq 3, count)
MAX04 = where(tmp_re eq 4, count)
MAX05 = where(tmp_re eq 5, count)
MAX06 = where(tmp_re eq 6, count)
MAX07 = where(tmp_re eq 7, count)
MAX08 = where(tmp_re eq 8, count)

S_MAX01 = size(MAX01, /N_DIMENSIONS) ; allows check for null entry
S_MAX02 = size(MAX02, /N_DIMENSIONS)
S_MAX03 = size(MAX03, /N_DIMENSIONS)
S_MAX04 = size(MAX04, /N_DIMENSIONS)
S_MAX05 = size(MAX05, /N_DIMENSIONS)
S_MAX06 = size(MAX06, /N_DIMENSIONS)
S_MAX07 = size(MAX07, /N_DIMENSIONS)
S_MAX08 = size(MAX08, /N_DIMENSIONS)

; M is median of each class
; FR number of pixel for each class
; AV mean pixel value of each class

If S_MAX01 le 0 Then Begin ; if no data in max01 then give null value
M01 = -999
FR01 = -999
AV01 = -999
Endif else Begin
M01 = median(tmp(MAX01))
FR01 = Size(tmp(MAX01), /N_ELEMENTS)
AV01 = mean(tmp(MAX01))
Endelse

If S_MAX02 le 0 Then Begin ; if no data in max02 then give null value
M02 = -999
FR02 = -999
AV02 = -999
Endif else Begin
M02 = median(tmp(MAX02))
FR02 = Size(tmp(MAX02), /N_ELEMENTS)
AV02 = mean(tmp(MAX02))
Endelse

If S_MAX03 le 0 Then Begin ; if no data in max03 then give null value
M03 = -999
FR03 = -999
AV03 = -999
Endif else Begin
M03 = median(tmp(MAX03))

```

```

FR03 = Size(tmp(MAX03), /N_ELEMENTS)
AV03 = mean(tmp(MAX03))
Endelse

If S_MAX04 le 0 Then Begin ; if no data in max04 then give null value
M04 = -999
FR04 = -999
AV04 = -999
Endif else Begin
M04 = median(tmp(MAX04))
FR04 = Size(tmp(MAX04), /N_ELEMENTS)
AV04 = mean(tmp(MAX04))
Endelse

If S_MAX05 le 0 Then Begin ; if no data in max05 then give null value
M05 = -999
FR05 = -999
AV05 = -999
Endif else Begin
M05 = median(tmp(MAX05))
FR05 = Size(tmp(MAX05), /N_ELEMENTS)
AV05 = mean(tmp(MAX05))
Endelse

If S_MAX06 le 0 Then Begin ; if no data in max06 then give null value
M06 = -999
FR06 = -999
AV06 = -999
Endif else Begin
M06 = median(tmp(MAX06))
FR06 = Size(tmp(MAX06), /N_ELEMENTS)
AV06 = mean(tmp(MAX06))
Endelse

If S_MAX07 le 0 Then Begin ; if no data in max06 then give null value
M07 = -999
FR07 = -999
AV07 = -999
Endif else Begin
M07 = median(tmp(MAX07))
FR07 = Size(tmp(MAX07), /N_ELEMENTS)
AV07 = mean(tmp(MAX07))
Endelse

If S_MAX08 le 0 Then Begin ; if no data in max06 then give null value
M08 = -999
FR08 = -999
AV08 = -999
Endif else Begin
M08 = median(tmp(MAX08))
FR08 = Size(tmp(MAX08), /N_ELEMENTS)
AV08 = mean(tmp(MAX08))
Endelse

data = reform(tmp,[XY])
MAXDN(i) = max(data)
MINDN(i) = min(data)
MEANDN(i) = mean(data)

DN(*,i) = data
HT(*,i) = histogram(DN(*,i), Binsize=1)
TOTHT = TOTHT + HT(*,i)

Window, 0, XSize=X, YSize=Y, XPos=0, YPos=0
erase
tv, tmp

```

```

Window, 1, XSize=X, YSize=Y, XPos=X+1, YPos=0
erase
tv, tmp_re
Window, 2, XSize=X, YSize=Y, XPos=X+1, YPos=Y+1
erase

plot, HT(*,i)

loadct, 0
tvct, R(0), G(0), B(0), 1
tvct, R(1), G(1), B(1), 2
tvct, R(2), G(2), B(2), 3
tvct, R(3), G(3), B(3), 4
tvct, R(4), G(4), B(4), 5
tvct, R(5), G(5), B(5), 6
tvct, R(6), G(6), B(6), 7
tvct, R(7), G(7), B(7), 8

print, '#####'
print, name+num+'.tif'
print, i, FN(i), FR01, FR02, FR03, FR04, FR05, FR06, FR07
print, M01, M02, M03, M04, M05, M06, M07

printf, lun1, '#####'
printf, lun1, name+num+'.tif'
printf, lun1, i, FN(i), M01, M02, M03, M04, M05, M06, M07

wait, 1

printf, lun2, FN(i), MEANDN(i), MAXDN(i), M01, M02, M03, M04, M05, M06, M07, M08, AV01, AV02, AV03, AV04, AV05,
AV06, AV07, AV08, format = '(3A5,16F7.2)'

Endfor

Close, lun
Close, lun1
Close, lun2

end

```

Final_albedo.pro – program assigns physical and albedo attributes to clustered image. Image statistics are then calculated for individual images as well as entire flight and recorded in “final_flightID.txt”. User must associate appropriate cluster representative surface ID. FR00 is null value, FR01 is cluster value 1, ..., FR08 is cluster value 8. Loop variables must be added and set to zero at beginning of loop. Note program requires additional loops to be added for images with 3,4,5,6,7 and 8 clusters. This program has been adapted from code created by Phillip Hwang at the Centre for Earth Observation Science.

```

; set albedo surfaces for t8 July 4
; program for counting stats on isocluster image (8 clusters)
; X: 612, Y: 480

; Make Color Map for Classification
; White:1, Yellow:2, Blue:3, Red:4, Green:5, grey:6, orange:7, black:8
R = [255, 255, 0, 255, 0, 100, 200, 0]
G = [255, 255, 0, 0, 255, 100, 100, 0]
B = [255, 0, 255, 0, 0, 100, 50, 0]

X = 612

```

Y = 480
XY = 293760.00

File_Len = 474

tmp = BytArr(612,480)
tmp_re = BytArr(612,480)
tmp_5c = BytArr(612,480)
DN = BytArr(XY,File_Len)
HT = LonArr(256,File_Len)
TOTHT = LonARR(256)
CAT = BytArr(File_Len)
MAXDN = BytArr(File_Len)
MINDN = BytArr(File_Len)
CUM_HIST = LonArr(256,100,6)
FN = StrArr(File_Len)
FR00 = 0

; STUDY SCENE ALBEDOS

ST_BRD = 0.0
ST_INT = 0.0
ST_PAR = 0.0
ST_VIS = 0.0
ST_NIR = 0.0
ST_BLU = 0.0

TST_BRD = 0.0
TST_INT = 0.0
TST_PAR = 0.0
TST_VIS = 0.0
TST_NIR = 0.0
TST_BLU = 0.0

; STUDY POND DEPTH
; STUDY SNOW DEPTH

ST_PD = 0.0
TST_PD = 0.0
ST_SN = 0.0
TST_SN = 0.0

; SNOW POND FRACTIONS

SN_FR = 0
PD_FR = 0
TSN_FR = 0.0
TPD_FR = 0.0

; PROGRAM VARIABLES

num = '000'
tmp_cat = '00'
openr, lun, 'list.txt', /Get_lun

name = 'md_t8_' ; Original
name_re = 'md_t8_' ; Classification

Openw, lun1, 'log.txt', /Get_lun
Openw, lun2, 't8_final.txt', /Get_lun

for i=0,File_Len-1 Do Begin

;LOOP BEGINS

;RESET ALL LOOP Variables to ZERO – this is a very important step and must be added to program

```
readf, lun, num

FN(i) = num

infile = name+num+'.tif'
infile_re = name_re+num+'.tif'

tmp = read_tiff(infile)
tmp_re = read_tiff(infile_re)

MAX01 = where(tmp_re eq 1, count) ; if class 1
MAX02 = where(tmp_re eq 2, count)
MAX03 = where(tmp_re eq 3, count)
MAX04 = where(tmp_re eq 4, count)
MAX05 = where(tmp_re eq 5, count)
MAX06 = where(tmp_re eq 6, count)
MAX07 = where(tmp_re eq 7, count)
MAX08 = where(tmp_re eq 8, count)

S_MAX01 = size(MAX01, /N_DIMENSIONS) ; allows check for null entry
S_MAX02 = size(MAX02, /N_DIMENSIONS)
S_MAX03 = size(MAX03, /N_DIMENSIONS)
S_MAX04 = size(MAX04, /N_DIMENSIONS)
S_MAX05 = size(MAX05, /N_DIMENSIONS)
S_MAX06 = size(MAX06, /N_DIMENSIONS)
S_MAX07 = size(MAX07, /N_DIMENSIONS)
S_MAX08 = size(MAX08, /N_DIMENSIONS)

; M is median of each class
; FR number of pixel for each class
; AV mean pixel value of each class

If S_MAX01 le 0 Then Begin ; if no data in max01 then give null value
  M01 = -999
  FR01 = 0
Endif else Begin
  M01 = median(tmp(MAX01))
  FR01 = Size(tmp(MAX01), /N_ELEMENTS)
Endelse

If S_MAX02 le 0 Then Begin ; if no data in max02 then give null value
  M02 = -999
  FR02 = 0
Endif else Begin
  M02 = median(tmp(MAX02))
  FR02 = Size(tmp(MAX02), /N_ELEMENTS)
Endelse

If S_MAX03 le 0 Then Begin ; if no data in max03 then give null value
  M03 = -999
  FR03 = 0
Endif else Begin
  M03 = median(tmp(MAX03))
  FR03 = Size(tmp(MAX03), /N_ELEMENTS)
Endelse

If S_MAX04 le 0 Then Begin ; if no data in max04 then give null value
  M04 = -999
  FR04 = 0
```

```

Endif else Begin
    M04 = median(tmp(MAX04))
    FR04 = Size(tmp(MAX04), /N_ELEMENTS)
Endelse

If S_MAX05 le 0 Then Begin ; if no data in max05 then give null value
    M05 = -999
    FR05 = 0
Endif else Begin
    M05 = median(tmp(MAX05))
    FR05 = Size(tmp(MAX05), /N_ELEMENTS)
Endelse

If S_MAX06 le 0 Then Begin ; if no data in max06 then give null value
    M06 = -999
    FR06 = 0
Endif else Begin
    M06 = median(tmp(MAX06))
    FR06 = Size(tmp(MAX06), /N_ELEMENTS)
Endelse

If S_MAX07 le 0 Then Begin ; if no data in max06 then give null value
    M07 = -999
    FR07 = 0
Endif else Begin
    M07 = median(tmp(MAX07))
    FR07 = Size(tmp(MAX07), /N_ELEMENTS)
Endelse

If S_MAX08 le 0 Then Begin ; if no data in max06 then give null value
    M08 = -999
    FR08 = 0
Endif else Begin
    M08 = median(tmp(MAX08))
    FR08 = Size(tmp(MAX08), /N_ELEMENTS)
Endelse

print, 'variables reset'

If (M03 le 0 and M04 le 0 and M05 le 0 and M06 le 0 and M07 le 0 and M08 le 0) Then Begin ; 2 or less classes

    SH_BRD = FR00/XY * 0.07
    SH_INT = FR00/XY * 0.07
    SH_PAR = FR00/XY * 0.07
    SH_VIS = FR00/XY * 0.07
    SH_NIR = FR00/XY * 0.07
    SH_BLU = FR00/XY * 0.07
    SHD = FR00 * (-1000.00)

    DP_BRD = FR00/XY * 0.196136
    DP_INT = FR00/XY * 0.17594029
    DP_PAR = FR00/XY * 0.25267218
    DP_VIS = FR00/XY * 0.23668260
    DP_NIR = FR00/XY * 0.05322401
    DP_BLU = FR00/XY * 0.32194998
    DPD = FR00 * (-10.00)

    MP_BRD = FR00/XY * 0.2265018
    MP_INT = FR00/XY * 0.17243517
    MP_PAR = FR00/XY * 0.25244208
    MP_VIS = FR00/XY * 0.23567994
    MP_NIR = FR00/XY * 0.04677485
    MP_BLU = FR00/XY * 0.32634968
    MPD = FR00 * (-4.92)

    SP_BRD = FR00/XY * 0.223464

```

SP_INT = FR00/XY * 0.18368372
SP_PAR = FR00/XY * 0.25633188
SP_VIS = FR00/XY * 0.24145330
SP_NIR = FR00/XY * 0.06526365
SP_BLU = FR00/XY * 0.32331566
SPD = FR00 * (-1.79)

SL_BRD = FR00/XY * 0.221270
SL_INT = FR00/XY * 0.17257218
SL_PAR = FR00/XY * 0.24947842
SL_VIS = FR00/XY * 0.23416910
SL_NIR = FR00/XY * 0.4704208
SL_BLU = FR00/XY * 0.31063782
SLD = FR00 * (-1.91)

TR_BRD = FR00/XY * 0.401775
TR_INT = FR00/XY * 0.39252546
TR_PAR = FR00/XY * 0.46949164
TR_VIS = FR00/XY * 0.45615442
TR_NIR = FR00/XY * 0.27519874
TR_BLU = FR00/XY * 0.51675955
TRD = FR00 * 1.85

SS_BRD = FR00/XY * 0.61793102
SS_INT = FR00/XY * 0.56448876
SS_PAR = FR00/XY * 0.61941034
SS_VIS = FR00/XY * 0.60991505
SS_NIR = FR00/XY * 0.48054771
SS_BLU = FR00/XY * 0.65758394
SSD = FR00 * 3.80

DS_BRD = FR00/XY * 0.70684395
DS_PAR = FR00/XY * 0.706997
DS_INT = FR00/XY * 0.749196
DS_VIS = FR00/XY * 0.744967
DS_NIR = FR00/XY * 0.644906
DS_BLU = FR00/XY * 0.759215
DSD = FR00 * 7.83

DP_LB_BRD = FR00/XY * 0.266239
DP_LB_PAR = FR00/XY * 0.289618515
DP_LB_INT = FR00/XY * 0.393725181
DP_LB_VIS = FR00/XY * 0.374967898
DP_LB_NIR = FR00/XY * 0.119878123
DP_LB_BLU = FR00/XY * 0.478832541
DP_LBD = FR00 * (-8.40)

MP_MB_BRD = FR00/XY * 0.327627
MP_MB_INT = FR00/XY * 0.29189116
MP_MB_PAR = FR00/XY * 0.39225370
MP_MB_VIS = FR00/XY * 0.37509041
MP_MB_NIR = FR00/XY * 0.13251932
MP_MB_BLU = FR00/XY * 0.45882780
MP_MBD = FR00 * (-4.14)

SP_HB_BRD = FR00/XY * 0.338573
SP_HB_INT = FR00/XY * 0.35385105
SP_HB_PAR = FR00/XY * 0.45559145
SP_HB_VIS = FR00/XY * 0.43857778
SP_HB_NIR = FR00/XY * 0.19230365
SP_HB_BLU = FR00/XY * 0.52327676
SP_HBD = FR00 * (-1.50)

TR_B_BRD = FR00/XY * 0.311353
TR_B_INT = FR00/XY * 0.36992637
TR_B_PAR = FR00/XY * 0.43057166
TR_B_VIS = FR00/XY * 0.4193084

TR_B_NIR = FR00/XY * 0.27254193
TR_B_BLU = FR00/XY * 0.47636864
TR_BD = FR00 * 2.75

BI_BRD = FR00/XY * 0.244479
BI_INT = FR00/XY * 0.24662474
BI_PAR = FR00/XY * 0.31966904
BI_VIS = FR00/XY * 0.30490010
BI_NIR = FR00/XY * 0.13025514
BI_BLU = FR00/XY * 0.37877767
BID = FR00 * 0.25

NI_BRD = FR00/XY * 0.53781064
NI_INT = FR00/XY * 0.4895807
NI_PAR = FR00/XY * 0.5331284
NI_VIS = FR00/XY * 0.5261625
NI_NIR = FR00/XY * 0.4201339
NI_BLU = FR00/XY * 0.5627277
NID = FR00 * 1.50

NS_BRD = FR00/XY * 0.62003849
NS_INT = FR00/XY * 0.624118
NS_PAR = FR00/XY * 0.659828
NS_VIS = FR00/XY * 0.655236
NS_NIR = FR00/XY * 0.569298
NS_BLU = FR00/XY * 0.677277
NSD = FR00 * 3.29

OS_BRD = FR00/XY * 0.678867
OS_INT = FR00/XY * 0.70007623
OS_PAR = FR00/XY * 0.7340255
OS_VIS = FR00/XY * 0.73123216
OS_NIR = FR00/XY * 0.64758695
OS_BLU = FR00/XY * 0.74774099
OSD = FR00 * 7.42

; CALCULATE AVERAGE DEPTH SNOW AND POND
; AV_PD = SUM "-" D / SUM "-" FR
; AV_SN = SUM "+" D / SUM "+" FR

; CALCULATE FRACTIONS SNOW AND POND (SSN(SPD)_FR = SUM FR/XY

; calculate snow and pond albedo (/ SUM FR)

PD_BRD = (SH_BRD + DP_BRD + MP_BRD + SP_BRD + SL_BRD + DP_LB_BRD + MP_MB_BRD + SP_HB_BRD) * XY

PD_INT = (SH_INT + DP_INT + MP_INT + SP_INT + SL_INT + DP_LB_INT + MP_MB_INT + SP_HB_INT) * XY

PD_PAR = (SH_PAR + DP_PAR + MP_PAR + SP_PAR + SL_PAR + DP_LB_PAR + MP_MB_PAR + SP_HB_PAR) * XY

PD_VIS = (SH_VIS + DP_VIS + MP_VIS + SP_VIS + SL_VIS + DP_LB_VIS + MP_MB_VIS + SP_HB_VIS) * XY

PD_NIR = (SH_NIR + DP_NIR + MP_NIR + SP_NIR + SL_NIR + DP_LB_NIR + MP_MB_NIR + SP_HB_NIR) * XY

PD_BLU = (SH_BLU + DP_BLU + MP_BLU + SP_BLU + SL_BLU + DP_LB_BLU + MP_MB_BLU + SP_HB_BLU) * XY

SN_BRD = (TR_BRD + SS_BRD + DS_BRD + TR_B_BRD + BI_BRD + NI_BRD + NS_BRD + OS_BRD) * XY

SN_INT = (TR_INT + SS_INT + DS_INT + TR_B_INT + BI_INT + NI_INT + NS_INT + OS_INT) * XY

SN_PAR = (TR_PAR + SS_PAR + DS_PAR + TR_B_PAR + BI_PAR + NI_PAR + NS_PAR + OS_PAR) * XY

SN_VIS = (TR_VIS + SS_VIS + DS_VIS + TR_B_VIS + BI_VIS + NI_VIS + NS_VIS + OS_VIS) * XY

SN_NIR = (TR_NIR + SS_NIR + DS_NIR + TR_B_NIR + BI_NIR + NI_NIR + NS_NIR + OS_NIR) * XY

```

SN_BLU = (TR_BLU + SS_BLU + DS_BLU + TR_B_BLU + BI_BLU + NI_BLU + NS_BLU + OS_BLU) * XY
    Endif

; repeat above loop for image clusters 3,4,5,6,7 and 8.

;calculate scene albedo

SC_BRD = SH_BRD + DP_BRD + MP_BRD + SP_BRD + SL_BRD + TR_BRD + SS_BRD + DS_BRD + DP_LB_BRD +
MP_MB_BRD + SP_HB_BRD + TR_B_BRD + BI_BRD + NI_BRD + NS_BRD + OS_BRD

SC_INT = SH_INT + DP_INT + MP_INT + SP_INT + SL_INT + TR_INT + SS_INT + DS_INT + DP_LB_INT + MP_MB_INT
+ SP_HB_INT + TR_B_INT + BI_INT + NI_INT + NS_INT + OS_INT

SC_PAR = SH_PAR + DP_PAR + MP_PAR + SP_PAR + SL_PAR + TR_PAR + SS_PAR + DS_PAR + DP_LB_PAR +
MP_MB_PAR + SP_HB_PAR + TR_B_PAR + BI_PAR + NI_PAR + NS_PAR + OS_PAR

SC_VIS = SH_VIS + DP_VIS + MP_VIS + SP_VIS + SL_VIS + TR_VIS + SS_VIS + DS_VIS + DP_LB_VIS + MP_MB_VIS
+ SP_HB_VIS + TR_B_VIS + BI_VIS + NI_VIS + NS_VIS + OS_VIS

SC_NIR = SH_NIR + DP_NIR + MP_NIR + SP_NIR + SL_NIR + TR_NIR + SS_NIR + DS_NIR + DP_LB_NIR +
MP_MB_NIR + SP_HB_NIR + TR_B_NIR + BI_NIR + NI_NIR + NS_NIR + OS_NIR

SC_BLU = SH_BLU + DP_BLU + MP_BLU + SP_BLU + SL_BLU + TR_BLU + SS_BLU + DS_BLU + DP_LB_BLU +
MP_MB_BLU + SP_HB_BLU + TR_B_BLU + BI_BLU + NI_BLU + NS_BLU + OS_BLU

data = reform(tmp,[XY])
MAXDN(i) = max(data)
MINDN(i) = min(data)

DN(*,i) = data
HT(*,i) = histogram(DN(*,i), Binsize=1)
TOTHT = TOTHT + HT(*,i)

plot, HT(*,i)

print, '#####'
print, name+num+'.tif'
print, i, FN(i), FR01, FR02, FR03, FR04, FR05, FR06, FR07
print, M01, M02, M03, M04, M05, M06, M07
print, SC_BRD, SC_INT, SC_PAR, SC_VIS, SC_NIR, SC_BLU, SN_BRD, SN_INT, SN_PAR, SN_VIS, SN_NIR, SN_BLU,
PD_BRD, PD_INT, PD_PAR, PD_VIS, PD_NIR, PD_BLU

printf, lun1, '#####'
printf, lun1, name+num+'.tif'
printf, lun1, i, FN(i), M01, M02, M03, M04, M05, M06, M07

; STUDY TOTALS

ST_BRD = ST_BRD + SC_BRD
ST_INT = ST_INT + SC_INT
ST_PAR = ST_PAR + SC_PAR
ST_VIS = ST_VIS + SC_VIS
ST_NIR = ST_NIR + SC_NIR
ST_BLU = ST_BLU + SC_BLU

; DEPTH TOTALS

ST_PD = ST_PD + AV_PD
ST_SN = ST_SN + AV_SN

; FRACTION TOTALS

SN_FR = SN_FR + SSN_FR
PD_FR = PD_FR + SPD_FR

```

```

; wait, 1

printf, lun2, FN(i), M01, M02, M03, M04, M05, M06, M07, M08, FR01, FR02, FR03, FR04, FR05, FR06, FR07, FR08,
SC_BRD, SC_INT, SC_PAR, SC_VIS, SC_NIR, SC_BLU, SN_BRD, SN_INT, SN_PAR, SN_VIS, SN_NIR, SN_BLU,
PD_BRD, PD_INT, PD_PAR, PD_VIS, PD_NIR, PD_BLU, SSN_FR, SPD_FR, format = '(A10,8F10.2,8I10,20F10.6)'

Endfor

TST_BRD = ST_BRD / File_Len
TST_INT = ST_INT / File_Len
TST_PAR = ST_PAR / File_Len
TST_VIS = ST_VIS / File_Len
TST_NIR = ST_NIR / File_Len
TST_BLU = ST_BLU / File_Len

TST_PD = ST_PD / File_Len
TST_SN = ST_SN / File_Len

TSN_FR = SN_FR / File_Len
TPD_FR = PD_FR / File_Len

printf, lun2, *****
printf, lun2, *****
printf, lun2, TST_BRD, TST_INT, TST_PAR, TST_VIS, TST_NIR, TST_BLU, TST_PD, TST_SN, TSN_FR, TPD_FR, format
= '(6f10.6, 4F10.2)'

free_lun, lun
free_lun, lun1
free_lun, lun2

End

```

APPENDIX D. RADARSAT-1 DATA SET

Table D.1. RADARSAT-1 data set collected and processed at the Alaska SAR Facility. Images are stored in the 8-bit CEOS format.

Granule	YD	Beam	Start Date	Center Point
R1 33357 ST1 260	84	1	26 Mar 2002, 13:56:11	75.10 Lat, -96.93 Lon;
R1 33414 ST3 260	89	3	30 Mar 2002, 13:39:26	75.48 Lat, -98.48 Lon;
R1 33434 ST2 190	90	2	31 Mar 2002, 23:06:46	75.26 Lat, -96.80 Lon;
R1 33434 ST2 191	90	2	31 Mar 2002, 23:06:53	75.63 Lat, -97.42 Lon;
R1 33457 ST2 259	92	2	02 Apr 2002, 13:51:53	75.64 Lat, -97.46 Lon;
R1 33457 ST2 260	92	2	02 Apr 2002, 13:51:59	75.27 Lat, -98.07 Lon;
R1 33477 ST3 189	93	3	03 Apr 2002, 23:19:12	75.10 Lat, -95.87 Lon;
R1 33477 ST3 190	93	3	03 Apr 2002, 23:19:19	75.48 Lat, -96.38 Lon;
R1 33500 ST1 259	95	1	05 Apr 2002, 14:04:26	75.46 Lat, -98.40 Lon;
R1 33506 ST7 188	96	7	06 Apr 2002, 00:01:01	75.09 Lat, -97.32 Lon;
R1 33506 ST7 189	96	7	06 Apr 2002, 00:01:08	75.49 Lat, -97.60 Lon;
R1 33514 ST3 261	96	3	06 Apr 2002, 13:35:18	75.11 Lat, -97.91 Lon;
R1 33557 ST2 260	99	2	09 Apr 2002, 13:47:45	75.27 Lat, -97.02 Lon;
R1 33600 ST1 259	102	1	12 Apr 2002, 14:00:15	75.46 Lat, -97.36 Lon;
R1 33600 ST1 260	102	1	12 Apr 2002, 14:00:21	75.10 Lat, -98.01 Lon;
R1 33606 ST7 188	102	7	12 Apr 2002, 23:56:50	75.09 Lat, -96.29 Lon;
R1 33606 ST7 189	102	7	12 Apr 2002, 23:56:57	75.49 Lat, -96.58 Lon;
R1 33614 ST3 260	103	3	13 Apr 2002, 13:31:01	75.48 Lat, -96.38 Lon;
R1 33614 ST3 261	103	3	13 Apr 2002, 13:31:08	75.11 Lat, -96.87 Lon;
R1 33657 ST2 260	106	2	16 Apr 2002, 13:43:36	75.27 Lat, -95.98 Lon;
R1 33657 ST2 261	106	2	16 Apr 2002, 13:43:42	74.90 Lat, -96.57 Lon;
R1 33677 ST2 189	107	2	17 Apr 2002, 23:10:51	74.89 Lat, -97.26 Lon;
R1 33677 ST2 190	107	2	17 Apr 2002, 23:10:58	75.26 Lat, -97.85 Lon;
R1 33700 ST1 259	109	1	19 Apr 2002, 13:56:04	75.46 Lat, -96.28 Lon;
R1 33700 ST1 260	109	1	19 Apr 2002, 13:56:11	75.10 Lat, -96.94 Lon;
R1 33734 ST1 191	111	1	21 Apr 2002, 22:54:18	75.45 Lat, -96.48 Lon;
R1 33820 ST3 189	117	3	27 Apr 2002, 23:19:10	75.10 Lat, -95.86 Lon;
R1 33820 ST3 190	117	3	27 Apr 2002, 23:19:17	75.48 Lat, -96.37 Lon;
R1 33843 ST1 259	119	1	29 Apr 2002, 14:04:24	75.46 Lat, -98.41 Lon;
R1 33849 ST7 188	120	7	30 Apr 2002, 00:00:59	75.09 Lat, -97.30 Lon;
R1 33849 ST7 189	120	7	30 Apr 2002, 00:01:06	75.49 Lat, -97.59 Lon;
R1 33877 ST2 190	121	2	01 May 2002, 23:02:31	75.26 Lat, -95.74 Lon;
R1 33877 ST2 191	121	2	01 May 2002, 23:02:38	75.63 Lat, -96.36 Lon;
R1 33943 ST1 259	126	1	06 May 2002, 14:00:14	75.46 Lat, -97.36 Lon;
R1 33943 ST1 260	126	1	06 May 2002, 14:00:21	75.10 Lat, -98.02 Lon;
R1 33949 ST7 188	126	7	06 May 2002, 23:56:50	75.09 Lat, -96.29 Lon;
R1 33949 ST7 189	126	7	06 May 2002, 23:56:56	75.49 Lat, -96.57 Lon;
R1 33957 ST3 260	127	3	07 May 2002, 13:31:00	75.48 Lat, -96.38 Lon;
R1 33957 ST3 261	127	3	07 May 2002, 13:31:07	75.11 Lat, -96.88 Lon;
R1 34000 ST2 260	130	2	10 May 2002, 13:43:34	75.27 Lat, -95.99 Lon;

Granule	YD	Beam	Start Date	Center Point
R1 34000 ST2 261	130	2	10 May 2002, 13:43:41	74.90 Lat, -96.58 Lon;
R1 34020 ST2 189	131	2	11 May 2002, 23:10:50	74.89 Lat, -97.25 Lon;
R1 34020 ST2 190	131	2	11 May 2002, 23:10:56	75.26 Lat, -97.84 Lon;
R1 34092 ST7 188	136	7	17 May 2002, 00:05:12	75.09 Lat, -98.36 Lon;
R1 34100 ST3 261	137	3	17 May 2002, 13:39:29	75.11 Lat, -98.97 Lon;

APPENDIX E. PROGRAMS USED WITH SAR DATA

ASF_tools. A collection of SAR tools are available from the Alaska SAR Facility website. The following are three tools used for calibration and geocoding of raw SAR data where incorporated into an UNIX shell program for batch processing. Information on tool usage can be found using the man pages provided with each program.

(<http://www.asf.alaska.edu/apd/software/index.html>)

Projprm. ASF projection program required for geocode and used in calibrate shell. Projection file = polar.proj, projection key = ps1.

```
Prompt input = "projprm plstereo ps1 polar.proj -s 6378273 -q 0.006693883 -l -97 -p 75"
```

Where `-s` is the major axis, `-e` is the eccentricity squared, `-l` is the centre longitude and `-p` is the standard parallel.

Calibrate.sh. Unix csh used to batch process SAR data for radiometric calibration, geocoding and clipping images to 200 x 200 pixels.

```
#csh
#shell to batch calibrate and clip SAR data
#shell used for thesis data and requires projection key from projprm

set inputdata = `ls -d R*.D` #read in all SAR files R.D
foreach loop ( $inputdata ) #read each file in
echo $loop
set dataname = (`echo $loop | cut -c1-16`) #keep char 1-16
set name = ( `echo $loop | cut -c2-16`) #keep char 2-16
set gname = g{$name} #gamma calibration
set gpname = gp{$name} #gamma polar coordinates
set spname = sp{$name} #sigma polar coordinates
set sname = s{$name} #sigma calibration
set gcname = gc{$name} #gamma polar and clip image
set scname = sc{$name} #sigma polar and clip image
echo $dataname
echo $name
echo $gname
echo $gpname
calibrate $dataname $gname -g #calibrate gamma
calibrate $dataname $sname #calibrate sigma

geocode -h 0 -p 100 $gname $gname polar.proj ps1 $gpname #geocode gamma to ps
geocode -h 0 -p 100 $sname $sname polar.proj ps1 $spname #geocode sigma to ps
geocode -h 0 -p 100 -i 75.23 -97.32 200 200 $gname $gname pl.proj truro $gcname
```

```

#geocode gamma and cut image to 200 x 200 centred at 75.27N, 97.17W (just east of study
area)

geocode -h 0 -p 100 -i 75.23 -97.32 200 200 $sname $sname pl.proj truro $sname
#geocode sigma and cut image to 200 x 200 centred at 75.27N, 97.17W

end #end loop

```

BIN_ASCII_200.pro

```

;IDL program to import binary images in ASF LAS format and export ASCII
grids
; requires a list of images to be processed "img_list.txt"

Data = BytArr(200,200)
Fn = '123'
NumOfFile = 350; required field and depends on number of images to be processed

  openr, 1, 'img_list.txt' ; image list

for i=0,NumOfFile-1 Do Begin

  readf, 1, fn
  print, fn+'.img'

  openr, 10, fn+'.img'
  readu, 10, Data
  close, 10

  openw, 20, fn+'.txt'
  printf, 20, Data, format='(200I)'
  close, 20

endfor

  close, 1

end

```

Val_extract.pro. Select value extraction for time series development.

```

; IDL program to extract selected values from 200 x 200 binary images.
Floating box averages can be applied to imagery first by adding one
bytarr (200,200), and the function "smooth" before values are
extracted. This was preformed using 3x3 and 5x5 windows. Sigma naught
values are exported to text file.

```

```

data = BytArr(200,200)
filter = BytArr(200,200)
name = strarr(30,122)
time = BytArr(10,122)
MN = 122

; Input X, Y - coordinates fall within the melt pond study area.

x0 = 70
y0 = 70

```

```

x1 = 70
y1 = 99
x2 = 99
y2 = 99
x3 = 99
y3 = 70
x4 = 77
y4 = 77
x5 = 77
y5 = 93
x6 = 93
y6 = 93
x7 = 93
y7 = 77
x8 = 85
y8 = 85
x9 = 0
y9 = 0
fname = string(30)

openr, lun, 'list.lst' , /Get_lun
For i=0, MN-1 Do Begin
    readf, lun ,fname
    name(i)= fname
Endfor
Close, lun

; Get data

For i=0, MN-1 Do Begin
    tmp = read_binary(name(i)+'.img')
    data = reform(tmp, [200,200])
    time(0,i) = data(x0,y0)
    time(1,i) = data(x1,y1)
    time(2,i) = data(x2,y2)
    time(3,i) = data(x3,y3)
    time(4,i) = data(x4,y4)
    time(5,i) = data(x5,y5)
    time(6,i) = data(x6,y6)
    time(7,i) = data(x7,y7)
    time(8,i) = data(x8,y8)
    time(9,i) = data(x9,y9)

Endfor

openw, lun1, 'Study_sigma_std.txt' , /Get_lun ; export file

For i=0, MN-1 Do Begin
    printf, lun1, name(i), time(0,i), time(1,i), time(2,i), time(3,i), time(4,i),
time(5,i), time(6,i), time(7,i), time(8,i), time(9,i), format = '(a20,10i10)'

Endfor

Close, lun1

End

```